SEARCH FOR ANOMALOUS LONG RANGE INTERACTIONS AT HIGHLY RELATIVISTIC VELOCITIES

by

Philip John Reiner

Submitted in Partial Fulfillment

of the

Requirements for the Degree

DOCTOR OF PHILOSOPHY

Supervised by Professor A. C. Melissinos

Department of Physics and Astronomy

The University of Rochester

Rochester, New York

1985

Abstract

A high energy particle accelerator can be used to test the energy dependence of gravitational interactions between massive particles at highly relativistic velocities. General Relativity predicts that such interactions must be proportional to $(2\gamma^2\beta^2+1)/\gamma$ where γ is the Lorentz factor and $\beta=v/c$ is the relative velocity of the interacting bodies. A test of this dependence could provide a direct measure of the spin of the graviton. In addition, the accelerator experiment also provides a means for setting limits on other "anomalous" interactions at relativistic velocities. Such a test was made at the Fermi National Accelerator Tevatron.

The Tevatron is a circular ring which accelerates 10^{13} protons to a peak energy of 800 GeV. The protons circulate in bunches spaced at the frequency of the accelerating RF field. The resulting structure of the beam provides a unique periodic source of gravity with strong components at several harmonics of the beam revolution frequency.

A superconducting microwave cavity transducer was used as a detector for mechanical strains induced by the gravitational or other possible long range interactions. The transducer consists of a set of coupled TE_{011} mode cavities operating at 10 GHz. The cavity system has two resonant modes with the useful property that mechanical perturbations at their difference frequency induce energy transitions between the modes. The detector was sensitive to harmonic displacements of 10^{-17} cm.

The detector was placed at a distance of 20 cm from the beam and was used to take 7 data sets during the January-April 1985 running of the Tevatron. At this time we set limits on the size of the induced metric strain of 1.5×10^{-16}. Given the mechanical properties of the detector this implies a limit on the coupling G_A of an anomalous longe range interaction $G_A < 2\times10^{19}\ G_N$ where G_N is Newton's constant. This shows that such interactions have an upper limit which is 17 orders of magnitude below the strength of electromagnetic interactions. Finally, we made a test of Special Relativity and showed that if we express the energy-momentum relation as

$$\left(\frac{E}{mc^2}\right)^2 = \frac{1}{\left(1-\frac{v^2}{c^2}\right)^{1+\varepsilon/2}}$$

the anomalous correction ε must be $\varepsilon < 0.017$.

Table of Contents

List of Tables

List of Figures

Appendix D

Chapter 1

1.1 Motivation

The bulk of our current understanding of nature assumes the existence of four basic forces which can occur between physical bodies, namely, the electromagnetic, strong, weak and gravitational force. Until the turn of the century, gravitation was experimentally understood only in terms of celestial mechanics and of a very limited number of experiments such as the Cavendish experiment and free falling mass experiments.[1] Einstein's Theory of General Relativity predicts new phenomena such as the curvature of space due to the presence of matter or energy and the radiation of gravitational energy by accelerated objects.[2] This theory has met with remarkable success in a number of extremely precise experiments. The curvature of space induced by massive objects has been verified by the gravitational light bending phenomenon and the time delay of radar signals reflected off the planet Mars.[3] The perihelion shift of Mercury in its orbit around the sun is also remarkably close to the shift predicted by General Relativity.[4] The equivalence between the gravitational and inertial mass which forms the foundation of General Relativity has been verified to one part in 10^{12} by the extremely precise Eötvös experiments.[5]

More recently, searches have been made for the presence of gravitational radiation from distant star systems and supernovae using sophisticated Weber-type bar antennas and interferometers. These experiments however have not yet produced conclusive results.[6,7] In general, most of these experiments involve celestial bodies but as yet, no purely laboratory tests have been possible.

The possibility of using a high energy particle storage beam to test the energy dependence of the gravitational interactions between massive particles has been discussed in the recent literature.[8,9,10,11] Such a test could provide a direct measure of the spin of the graviton which is believed to be the exchange quantum mediating the gravitational interaction. At present however, the detection of these interactions at relativistic velocities appears to be beyond the capability of the available technology.

The experiment described here was designed to test such a gravitational detector by taking advantage of the highly stable relativistic particle beams at the Fermi National Accelerator Laboratory Tevatron. This test also sought to establish the level at which background electromagnetic effects for such an experiment become manifest. These goals were achieved and are discussed in the thesis.

The relative strengths of the four known interactions are depicted in figure 1.1. The large gap between the weak force and gravitation prompts the question: Are there other forces of intermediate strength which have not yet been detected? Such forces must of course have classical limits and ranges which have prevented

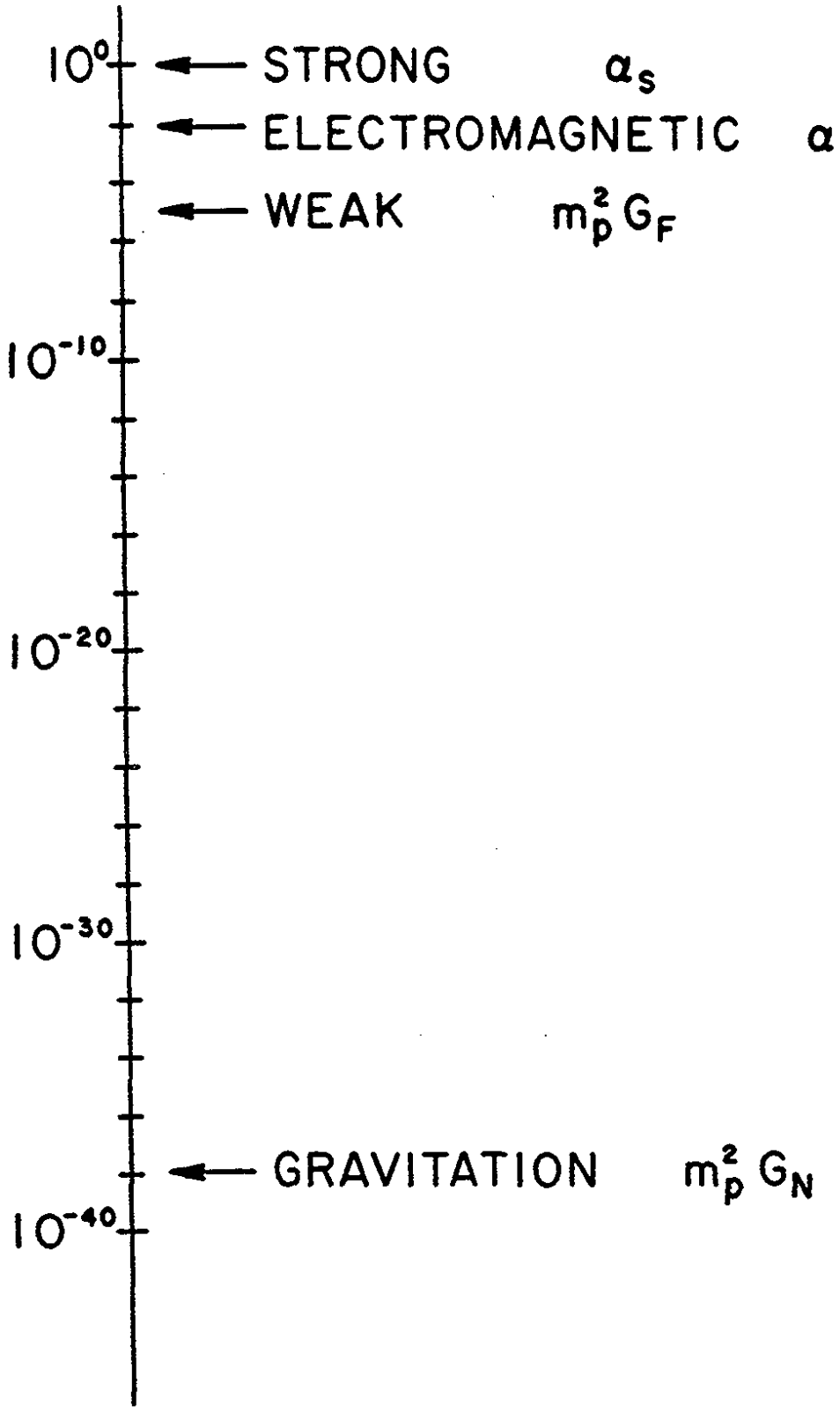

FIGURE 1.1 RELATIVE STRENGTH OF KNOWN FORCES

their detection by all of the experiments previously mentioned. Perkins[12] has shown for instance that the Eötvös experiments of Dicke and Braginsky predict that a long range force which couples to baryon number must have a coupling strength less than $10^{-9} G_N$ where G_N is the familiar Newton Constant. These experiments involve non-relativistic sources of gravity.

Alternatively, suppose that the "new" force has a high γ dependence ($\gamma=[1-v^2/c^2]^{-\frac{1}{2}}$) so that it fails to appear at Newtonian velocities. Such a case however must arise only for forces with ranges shorter than the impact parameter of the light bending experiments since they already place stringent limits on the allowable velocity dependence of the gravitational interactions between a massive object and photons.[13] The sensitivity of the detector used in this experiment is adequate to test for such unknown forces mediated by exchange particles of mass $\sim 10^{-6}$ eV which corresponds to a range of ~20 cm.

From the data, the limit set for the coupling of any new long range force between massive bodies with the same general characteristics as gravitation (that is for tensor fields with 1/r potential) is $G_A < 10^{19} G_N$. The corresponding limit set on the size of the electromagnetic background is

$$\frac{G_A m_p^2}{\hbar c} < 5 \times 10^{-18} \alpha_e$$

where α_e is the fine structure constant, $\alpha_e=1/137$. Finally, the

frequency stability of the ramp cycle of the Tevatron beam allowed an interesting test of Special Relativity. This is discussed in detail in Appendix A.

1.2 Effects at the FNAL Tevatron

A high energy particle accelertator provides a highly stable periodic source of gravitation and can be used to explore the nature of the relativistic gravitational interactions between massive objects. This discussion includes the expected effects at the FNAL Tevatron.

Consider a single bunch of N protons circulating in the Tevatron near a massive detector with a revolution frequency ω_0 as shown in figure 1.2. Since the mass of both the detector and the protons in the beam is small, the gravitational potentials can be derived by assuming that they are periodic perturbations on the locally flat Minkowski metric denoted by $\eta^{\mu\nu}$.[14]

$$h^{\mu\nu} = g^{\mu\nu} - \eta^{\mu\nu} \tag{1.1}$$

With this assumption, the non-zero components of the potentials at the position of the observer in figure 1.2b are

$$h^{00} = h^{ii} = \frac{2GNm_p(2\gamma^2\beta^2+1)}{c^2(y^2+\gamma^2\beta^2c^2t^2)^{\frac{1}{2}}} \tag{1.2a}$$

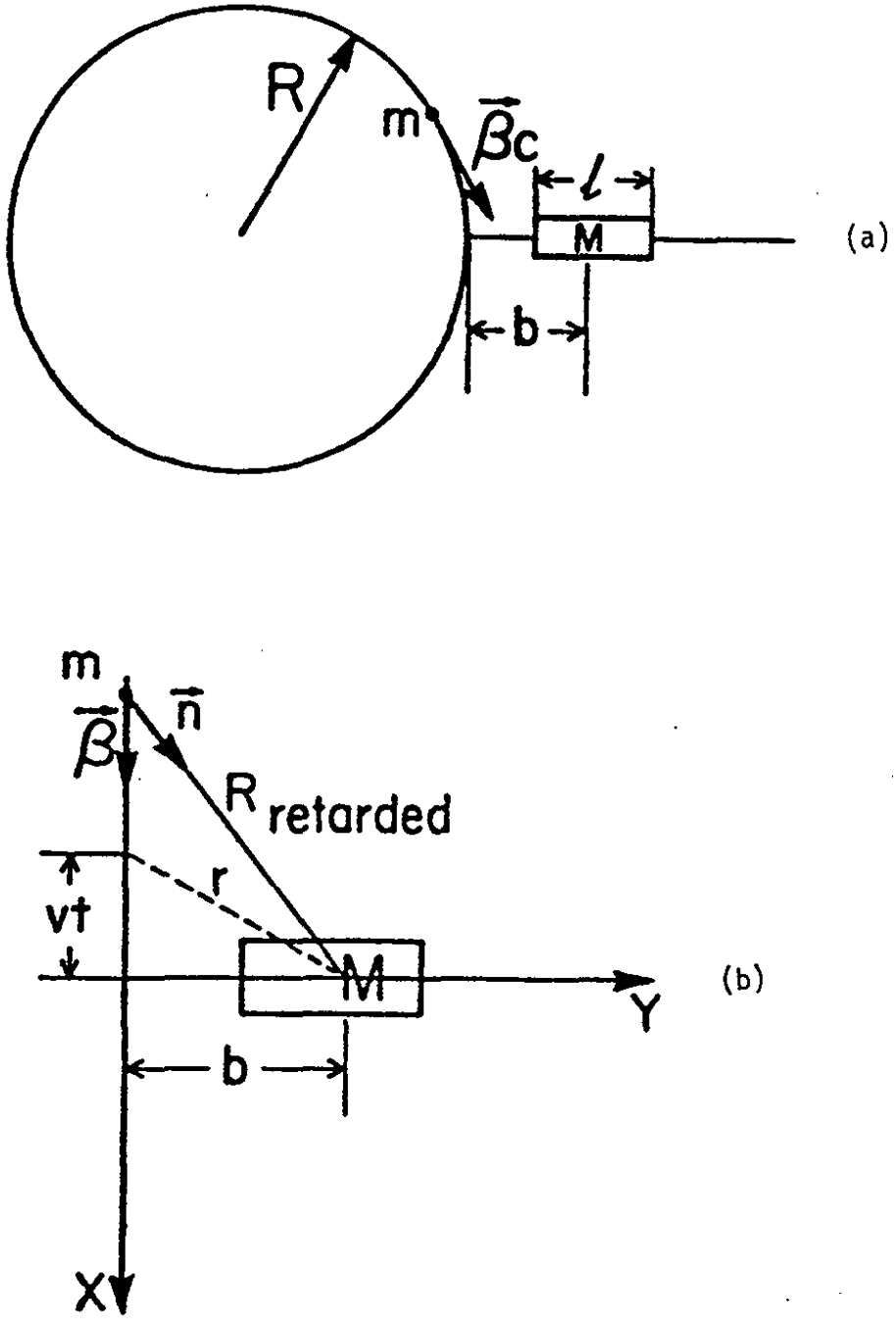

FIGURE 1.2 MASSIVE DETECTOR NEAR HIGH ENERGY STORAGE RING

$$h^{0i} = h^{i0} = \frac{2GNm_p(2\gamma^2\beta)}{c^2(y^2+\gamma^2\beta^2c^2t^2)^{\frac{1}{2}}} \qquad (1.2b)$$

Here γ is the Lorentz contraction factor and β the velocity of the protons relative to the speed of light. These potentials essentially measure the strain of the metric due to the passage of the beam near the detector. An observer at position M will receive an average impulsive acceleration in the transverse direction given by[8,9]

$$\left\langle \frac{F}{m} \right\rangle = \frac{2GNm_p}{\gamma\beta bc}(1+2\gamma^2\beta^2) \qquad (1.3)$$

The detector used in this investigation will respond to two distinct effects. The first is the direct coupling of the metric strain to the cavity fields. For our case, the detector had two well defined orthogonal electromagnetic modes where U_1 and U_2 are the stored energy in the first and second mode. If initially $U_1=0$ the coupling to the gravitational strain results in[15]

$$U_1 = \alpha h^2 U_2 \qquad (1.4)$$

Here h is the metric strain and the coefficient α is dependent on the detection scheme and will be characterized in detail in chapter 3. Thus, passage of the beam causes a local strain in the metric which is harmonic and can couple to electromagnetic fields.

The second effect is the detection of the gravitational force or the imposed acceleration of the detector given by equation 1.3. In this case, the assumption is made that the gravitational force causes a mechanical oscillator of mass m to be driven into oscillation at the precise revolution frequency of the proton bunch. If the oscillator has a resonant frequency ω_0 with mechanical $Q=Q_m$ then these oscillations will build up to a maximum displacement of the oscillator of

$$\Delta l_{max} = 2 \left\langle \frac{F}{m} \right\rangle \frac{Q_m}{\omega_0^2} \qquad (1.5)$$

Now, if the oscillator has length l then the effective strain induced is just $\Delta l/l$. This will result in the conversion of power from mode 2 to mode 1 according to equation 1.4 if we replace h by $\Delta l/l$. Thus, the effect of the mechanical Q_m is to coherently store energy from the gravitational coupling between the detector and the beam and allow the enhancement of the total strain developed across the detector.

1.3 Scope of E-723

The purpose of this investigation was to place the best limits possible on the measured size of the gravitational strains and

accelerations produced by the proton beam and observe any anomalous long range interactions between the relativistic particle beam and a massive detector. The detector was placed in the accelerator tunnel at the C0 straight section and the detection electronics was housed in the C0 Spectrometer room located on the main ring as shown in figure 1.3.

The detector used was a two cavity parametric transducer developed at the University of Rochester capable of measuring effective strains of $\sim 10^{-18}$ or harmonic displacements of $\sim 10^{-17}$ cm. The bulk of the work of this investigation has been the operation of this detector in the high radiation environment of the particle accelerator at FNAL. This posed several technically difficult problems including the remote control operation of the detector as well as compliance with the safety codes for operation in a limited access environment.

A first test of the detector was made in the spectrometer room at a distance of ~7.6 meters from the beam. Fine tuning of the detector as well as development of reliable remote control systems were made and tested during the May-July 1984 running period. The detector was installed into the tunnel at a distance of 20 cm from the Tevatron beam during the September-November 1984 shutdown of the ring. Finally, the data for this investigation was obtained during the January-April 1985 running period.

The limit on the gravitational strain measured at this time was 3.96×10^{-16} with a corresponding effective acceleration of 6.8×10^{-5} cm/s^2.

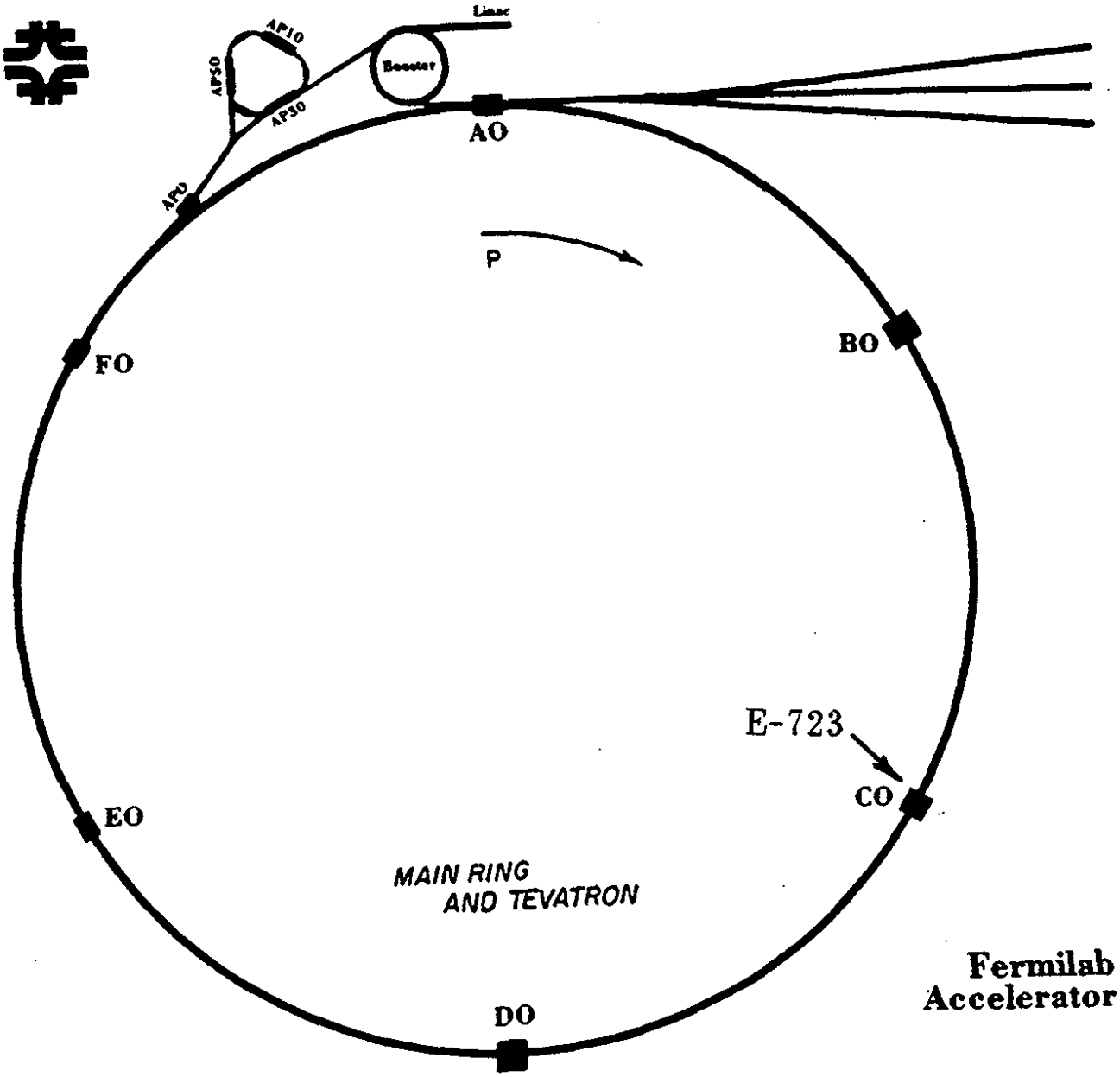

FIGURE 1.3 GEOGRAPHIC LOCATION OF E-723

Three different detection schemes were used to obtain the data reported during this running period. The first two configurations yielded 5 data sets taken at a temperature of 4.2 K and represent a total of 1,190 beam cycles.

During these runs, several erroneous noise signals appeared with the proper frequencies and propagated through the detection system. The origins of each of these signals were investigated and in each case with the proper use of shielding and grounding techniques they were systematically eliminated. The net result shown in the 5 data runs yielded no unusual signals.

The last detection scheme utilized the phase and amplitude information for the detected signals and allowed for enhanced signal to noise ratios. A sixth data set was obtained using the improved signal processing technique but still without a conclusive signal in the background noise. Finally, improvements in the electrical properties of the detector were made for the seventh data run. These results yielded our first real beam induced signal which can not be immediately attributed to the pick-up and cross-talk problems encountered previously. The exact origin of this signal is unknown but appears to be beam related and represents our first hard limitation on the achieveable sensitivity of the detector in the particle accelerator environment.

Chapter 2 deals with the characteristics of the Tevatron particle beam and gives a detailed analysis of the time and frequency spectra of the beam. The basic operation of the detector and the sensitivity to mechanical strain is reported in chapter 3.

The elaborate apparatus used in this investigation is cited in chapter 4 including the computer based data acquisition system. Chapter 5 details the results of this research obtained during the January-April running period of the Tevatron and includes the measured limits on the effective strains and accelerations of the detector system. These measurements are compared to the expected gravitational strain and accelerations in chapter 6 where we also discuss the limits placed on anomalous long range interactions. A limit on deviations from the predictions of the theory of special relativity is given in appendix A. Details of the Fourier analysis of the beam distribution are given in appendix B and appendix C presents a simulation of the signal processing using test data obtained with the data acquisition system. Finally, appendix D gives an analysis of the expected electromagnetic backgrounds at the detector in the Tevatron environment.

References

1. C.W. Misner, K.S. Thorne, and J.A. Wheeler,Gravitation (W.H. Freeman and Company, 1973),1121-1126.

2. A. Einstein, Preuss. Akad. Wiss. Berlin, Sitzber., 688-696 (1916).

3. C. Will, in Theory and Experiment in Gravitational Physics, (Cambridge University Press 1981), 166-183.

4. I. Shapiro et al., Phys. Rev. Lett. 28, 1594-7 (1972).

5. V. Braginsky and V. Panov., Sov. Phys. JETP. 34, 463-6 (1972).

6. N. Deruelle and T. Piran (editors). Gravitational Radiation, (North Holland Publishing Company, 1983).

7. R.W.P. Drever, Workshop on Gravitational Radiation, Ecole d'Ete de Physique Theorique, (North Holland Publishing Co., Amsterdam, 1983).

8. A.C. Melissinos, Il Nouvo Cimento, 62B, 190 (1981).

9. V.B. Braginsky, C.M. Caves and K.S. Thorne, Phys. Rev., D15, 2047 (1977).

10. C.M. Caves, Phys. Letts., 80B,323 (1979).

11. C.E. Reece, P.J. Reiner and A.C. Melissinos, Phys. Letts., 104A, 341-4 (1984).

12. D.H. Perkins, Introduction to High Energy Physics, (Addison Wesley Publishing Company, 1972),ch. 6.

13. D. Koltun, Report No. UR-782, Department of Physics and Astronomy, University of Rochester, Rochester, N.Y. (1981) (unpublished).

14. L.D. Landau and E.M. Lifshitz, The Classical Theory of Fields, 4th Edition, Volume 2 (Pergamon Press, NY 1975) Chapter 12.

15. C.E. Reece, P.J. Reiner, A.C. Melissinos, Report No. UR-832, Department of Physics and Astronomy, University of Rochester, Rochester, NY. (1982) (unpublished).

Chapter 2

Tevatron Beams

2.1 Introduction

This chapter discusses the nature and characteristics of the accelerated beam at the FNAL Tevatron. Since our detection scheme relies upon the ability to measure beam induced effects of known frequency and phase, it is necessary to understand and measure the harmonic content of the proton beam.

Section 2.2 describes the basic operation of the Tevatron during normal high energy physics (HEP) running periods. The next section describes the basic periodic time structure of the beam during acceleration and section 2.4 details the Fourier analysis of the beam. Finally, in section 2.5 the concept of the "effective" gravitational mass of the proton beam is introduced.

2.2 HEP Tevatron Beam Operation

In simple terms, the Tevatron consists of a series of cryogenic bending and focusing magnets used to guide the proton beam and a set

of radio frequency cavities used to accelerate the protons in bunches to 800 GeV/proton. Beam is injected at 8 GeV from a booster ring in a series of 13 booster batches which will be described in section 2.2. The injected protons are accelerated to 150 GeV/proton in the main ring which consists of normal temperature magnets and then injected into the Tevatron. The Tevatron then accelerates the bunched beam to its final energy in about 20 seconds. Figure 2.1 shows one complete beam cycle of the magnet ramp and the intensity of the beam in the Tevatron. The bending magnet current is ramped so that the increase in energy of the beam is approximately linear with time. A more detailed discussion of the energy ramp is given in Appendix A. During this time, the RF frequency of the beam has increased from 53.112 MHz to 53.120 MHz to remain synchronous with the basic beam revolution frequency of the protons which increased from 47.712 kHz by 900 mHz. Once the magnets are fully ramped, "flattop" operation begins where the particles are kept at constant energy (800 GeV) and are extracted to various experimental areas. During the next 20 seconds, the field in the magnets is returned to the level needed for the next injection cycle to begin. Figure 2.1 also shows the particle intensity as a function of time during the ramp cycle. Most of our data was obtained during the flattop portion of this cycle.

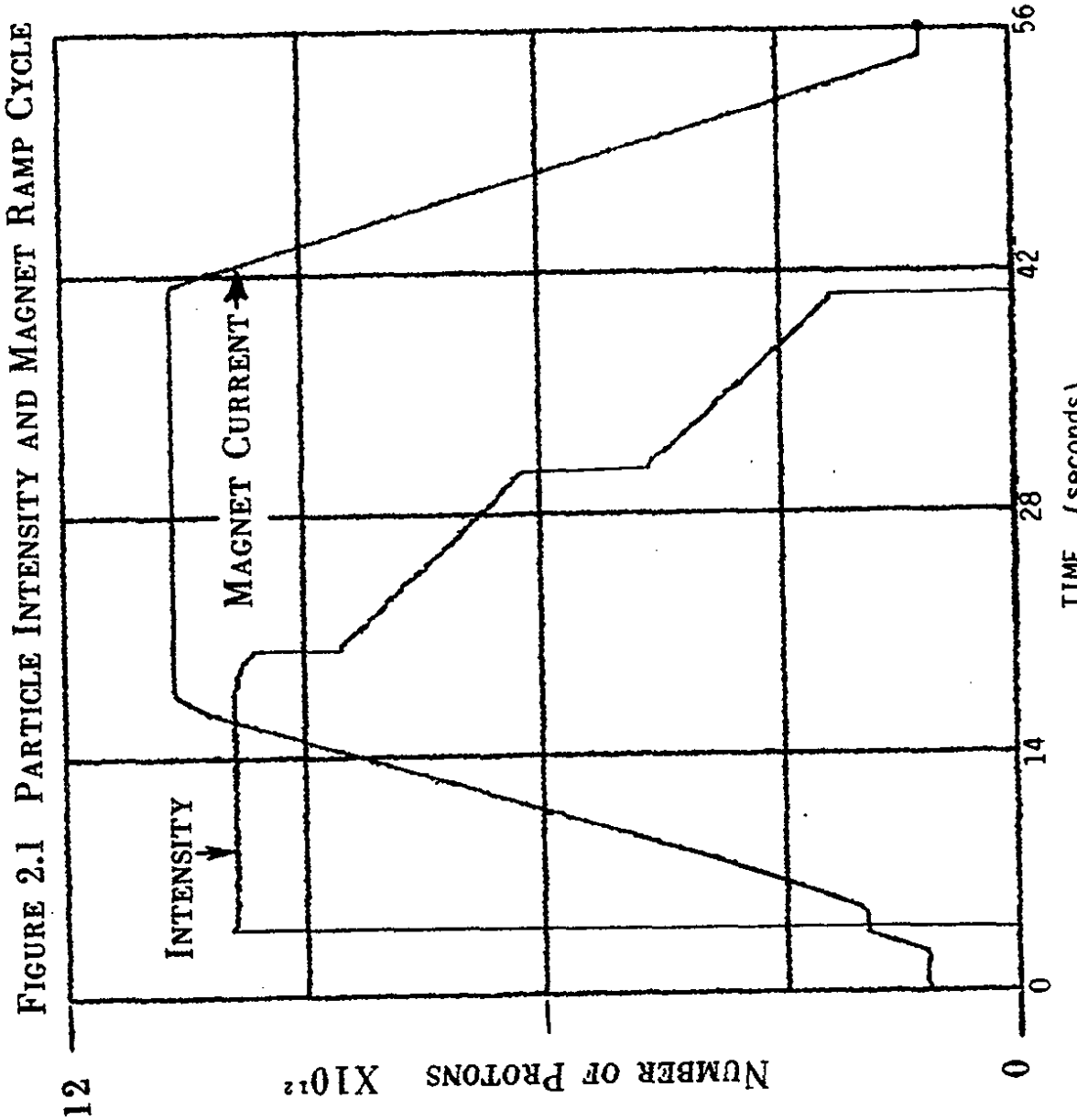

FIGURE 2.1 PARTICLE INTENSITY AND MAGNET RAMP CYCLE

2.3 Beam Structure

Protons are injected form the booster ring into the main ring in a series of 13 batches, one after the other. Each batch consists of 85 "buckets" or stable RF regions into which the protons can coalesce. During normal HEP operations, only 12 of the 13 batches are filled and injected into the main ring and then into the Tevatron so that the resulting structure is as shown in figure 2.2a. The Tevatron RF system is designed to have 1113 equally spaced buckets around the ring or approximately 13 booster batches. One such booster batch is shown in figure 2.2b. In this particular case, only 79 of the available 85 buckets have been filled giving rise to the narrow gap structure shown in figure 2.2a. During the main running period for which the data was obtained the structure consisted of 4 missing buckets with 81 buckets filled. This gap is of extreme importance as will be shown in section 2.4 since it gives rise to a strong 26^{th} harmonic signal. The actual structure of several individual buckets is shown in figure 2.2c and of course follows the basic RF frequency of 53.1196 MHz. A description of the beam pick-ups used to obtain the traces in figure 2.2 is given in section 4.6.

Each bucket is approximately a 1 nanosecond wide (rms) gaussian pulse (which corresponds to an rms length of 30 cm.) Individual buckets are separated by ~20 nanoseconds or 6 meters. As can be seen from figures 2.2a and 2.2b the individual buckets vary somewhat in size, but the overall structure remains essentially the same

FIGURE 2.2 PROTON DISTRIBUTION IN TEVATRON AT 800 GEV

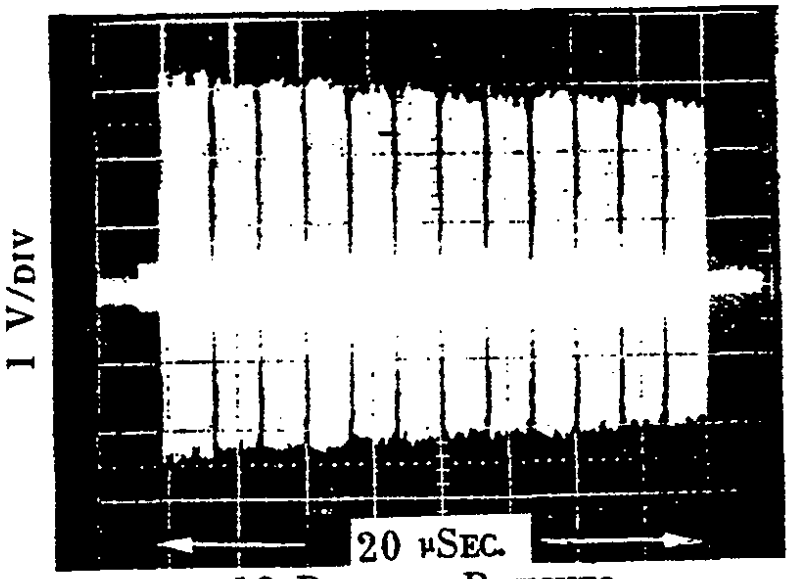

2.2A

12 BOOSTER BATCHES

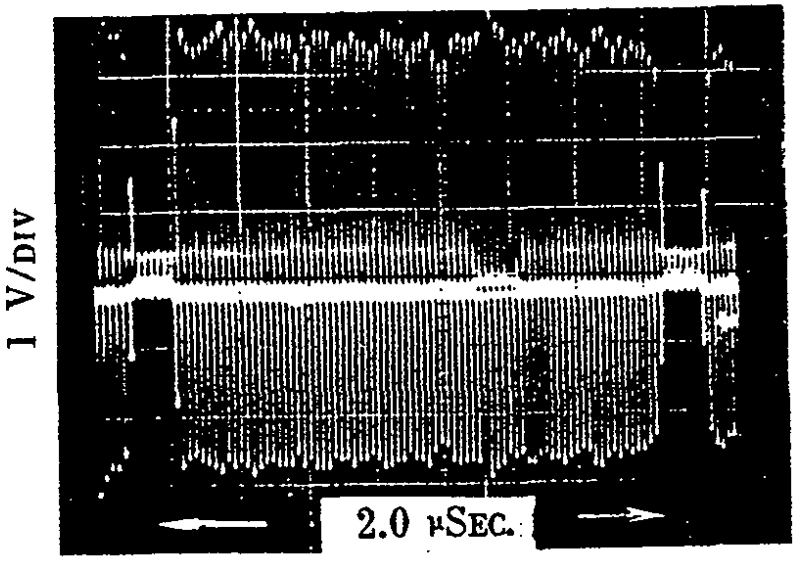

2.2B

1 BOOSTER BATCH

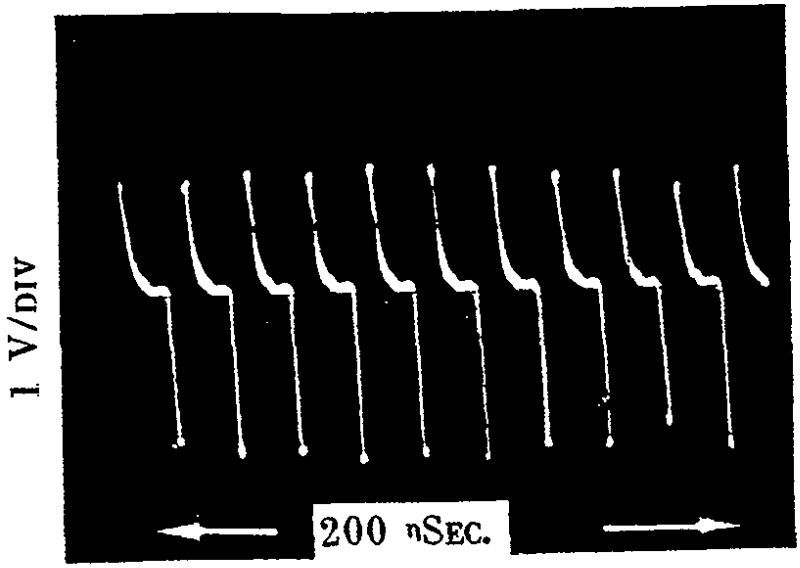

2.2C

INDIVIDUAL BUCKETS

during a given running period. In addition, the particle intensity (total number of protons in the ring) may vary from cycle to cycle: This is also true for the spill structure during the flattop operation. The best results obtained and discussed here were for beam intensities of approximately 9.0×10^{12} protons or $\sim9.3\times10^{9}$ protons per bucket.

2.4 Fourier Analysis of the Beam Distribution

The periodic nature of the particle orbits gives rise to well defined harmonics of the fundamental beam revolution frequency at 47,713.00±.01 Hz. Our detector had an available tuning range as described in section 3.2 from 1.19 to 1.34 MHz so that it could be made sensitive to periodic perturbations at the 25^{th}, 26^{th}, 27^{th}, or 28^{th} harmonic of the 47 kHz. We chose in particular to work at the 26^{th} harmonic at 1.24054093 MHz ±25 mHz for the reasons given below.

A computer model for the particle number density was developed to assist in the analysis of the harmonic content of the beam as detailed in Appendix B. We assume that the individual buckets are gaussian shaped pulses equally spaced around the ring so that the time dependence of the beam can be written as follows.

$$F_{total}(t) = \sum_{m=0}^{1112} A_m f_o(t-t_m) \qquad (2.1)$$

where A_m is the number of protons in bucket m and $f_0(t-t_m)$ is given by ;

$$f_0(t) = \frac{1}{\sqrt{2\pi}\sigma} e^{\frac{1}{2}(t/\sigma)^2} \tag{2.2}$$

We can decompose $F_{total}(t)$ into its Fourier components so that the n^{th} harmonic of the fundamental revolution frequency ω_0 given by $F(\omega)$ is

$$F^n(\omega) = C_n \cos(n\omega_0 t+\phi) \tag{2.3}$$

where ϕ = arc tan (B/A)

and

$$C_n = 2\sqrt{A_n^2+B_n^2}$$

where

$$A_n = \sum_{m=1}^{1112} A_m f_{0n}(\omega)\cos\left(\frac{2\pi\omega m}{1113}\right)$$

(2.3a)

$$B_n = \sum_{m=1}^{1113} A_m f_{0n}(\omega) \sin\left(\frac{2\pi\omega m}{1113}\right)$$

The normalization was then chosen by dividing $F(\omega)$ by the strength of the n^{th} harmonic in the case where all of the protons are in a single bunch.

The harmonic content of the beam was measured by mixing the signal from the beam position monitor with a local oscillator signal as shown in figure 2.3. The local oscillator signal was provided by a Model HP3325A Synthesizer and the mixer was a Model MD-140 double balanced mixer manufactured by Anzac Inc. The frequency of the synthesizer was adjusted so that the desired output of the mixer was at 10 kHz. This signal was then measured with a Model 8561A HP Fast Fourier Transform Analyzer.

The solid line in figure 2.4 shows the first 30 harmonics of the 47 kHz that were measured at flattop (along with the 1113^{th} harmonic at 53.119693 MHz ±5 Hz) during normal HEP operation with 12 booster batches in the ring. The dashed curve is the computer model assuming 12 booster batches with each booster batch having 81 equally filled buckets with 4 empty buckets between batches. This same structure was measured directly from the beam position monitor on an oscilloscope. From this analysis we see that the 26^{th} harmonic was particularly strong relative to the 25^{th}, 27^{th}, and the 28^{th} harmonics so that the choice was made to tune the cavities to the 26^{th}.

Figure 2.5 shows several computer models with different gap

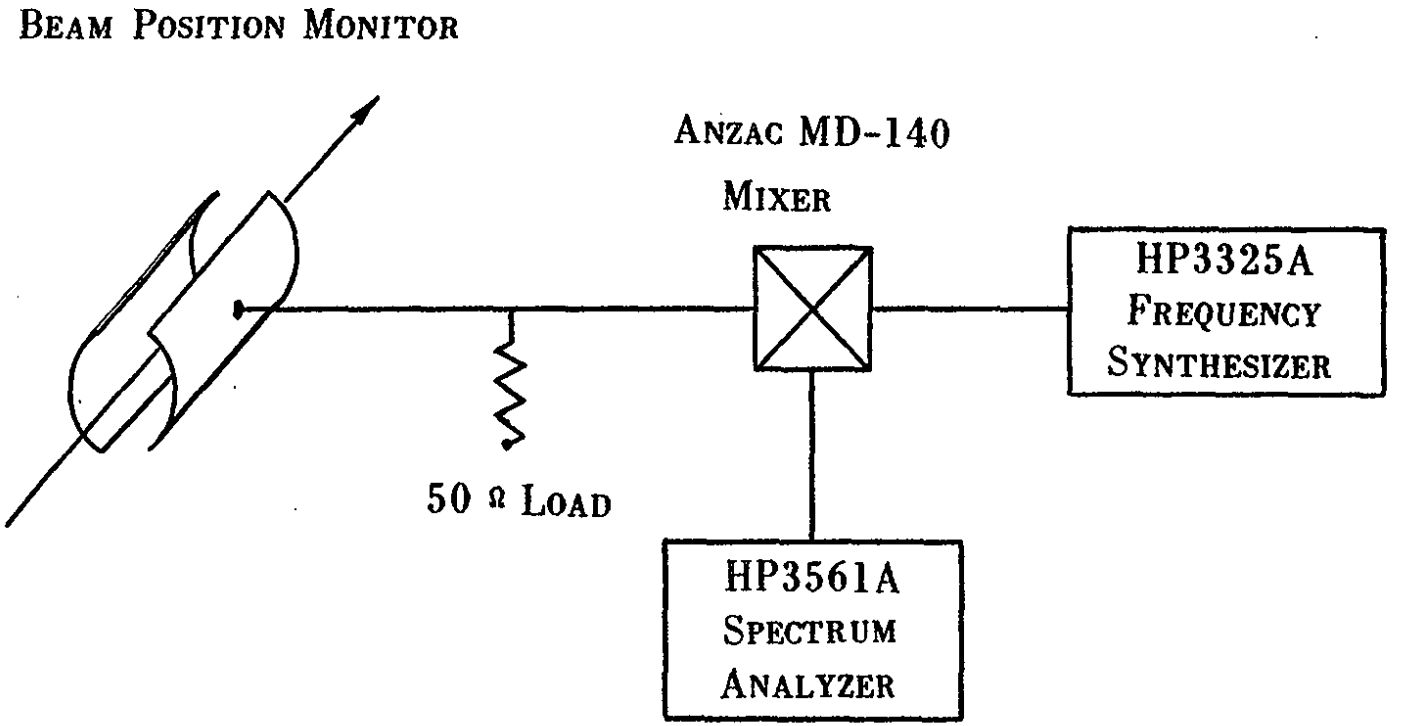

Figure 2.3 Apparatus for Measuring Harmonic Content of Beam

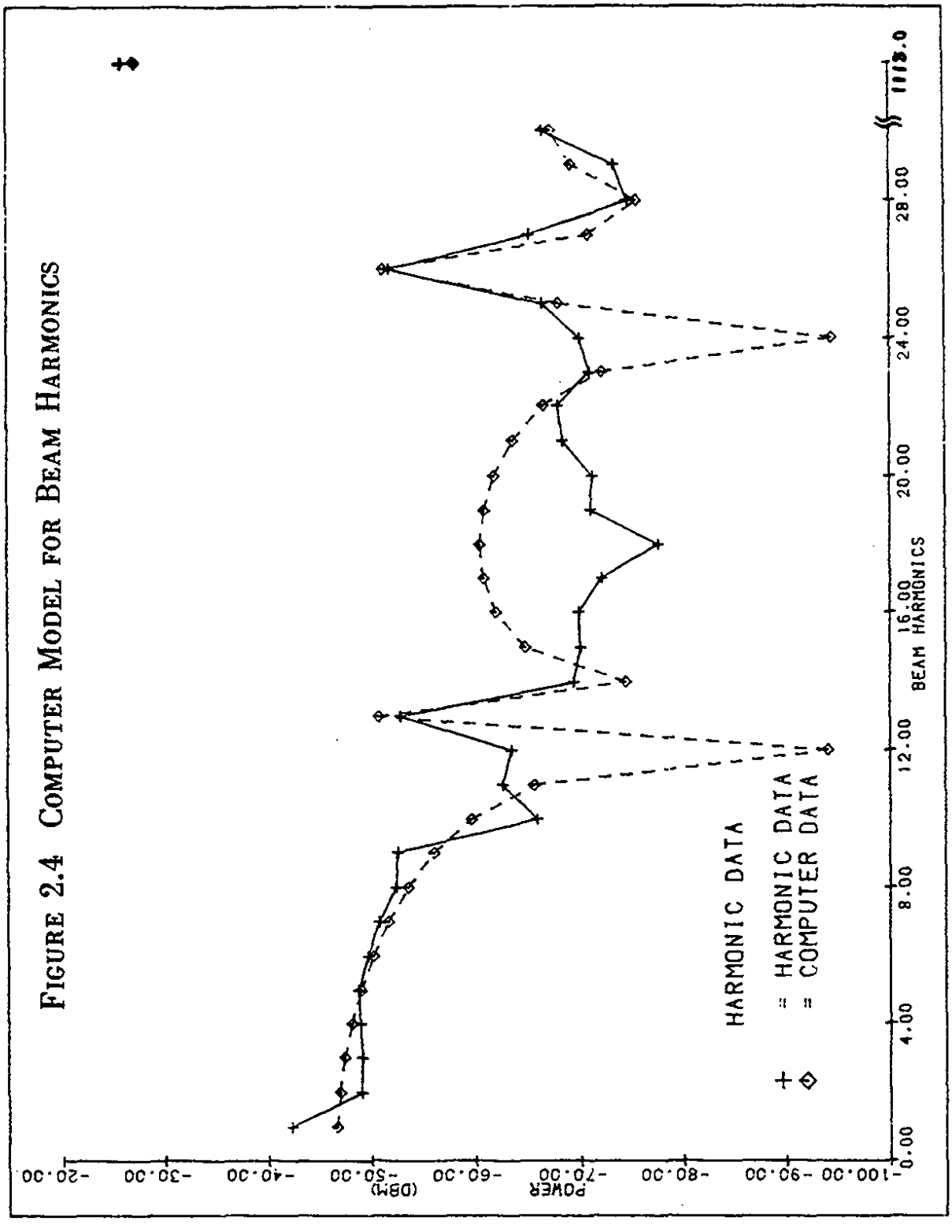

FIGURE 2.4 COMPUTER MODEL FOR BEAM HARMONICS

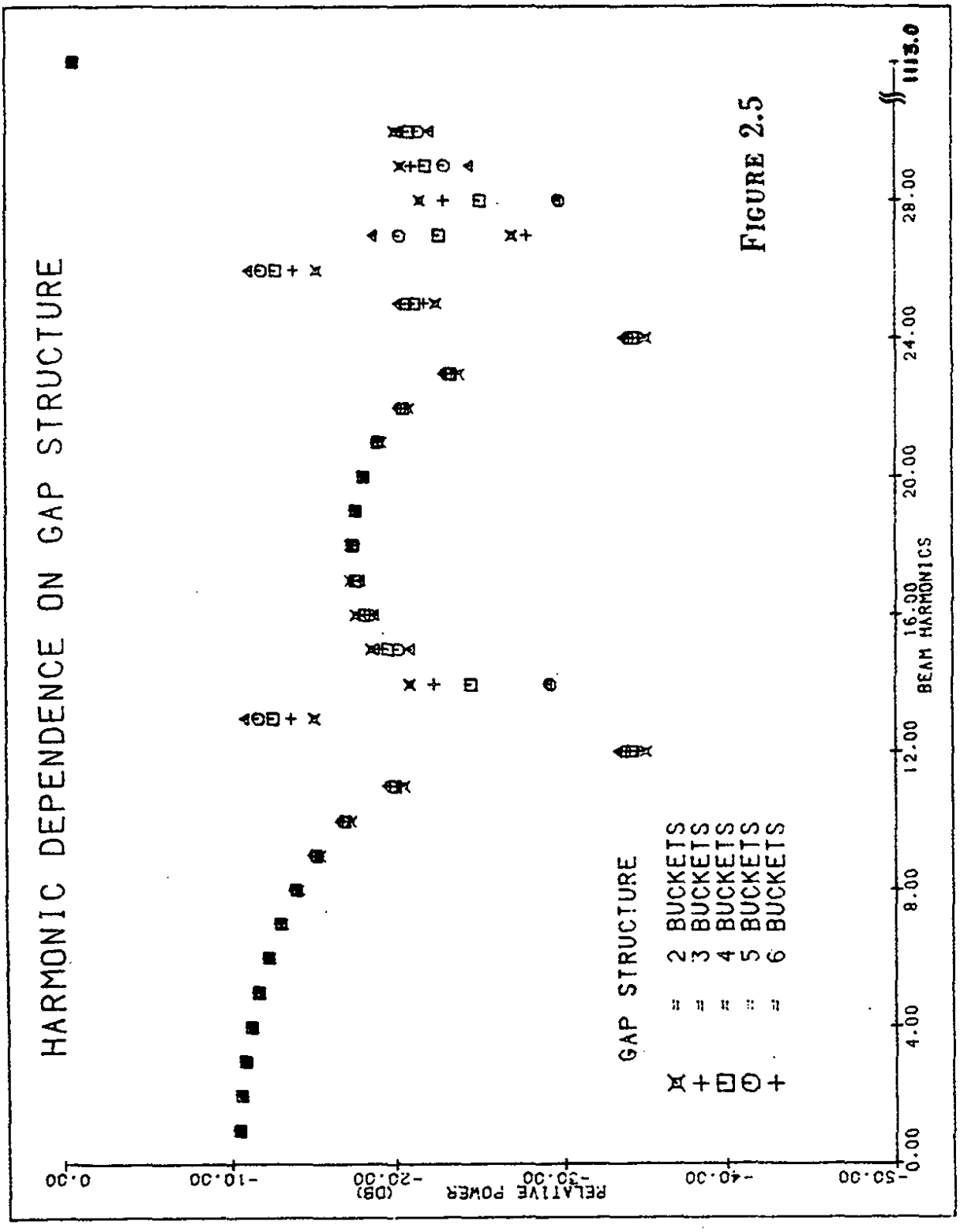
HARMONIC DEPENDENCE ON GAP STRUCTURE
GAP STRUCTURE
2 BUCKETS
3 BUCKETS
4 BUCKETS
5 BUCKETS
6 BUCKETS
RELATIVE POWER (DB)
0.00
-10.00
-20.00
-30.00
-40.00
-50.00
4.00
8.00
12.00
16.00
20.00
24.00
28.00
1113.0
BEAM HARMONICS

FIGURE 2.5

structure between the batches. This analysis shows that the relative strength of the peaks at the 13^{th} and 26^{th} are directly related to the number of buckets missing between the booster batches. In each case however we note that the actual size of the 26^{th} harmonic does vary slightly, but the 1^{st} and the 1113^{th} remain essentially the same.

Several different measurements of the 26^{th} harmonic were also made with varying numbers of filled booster batches in the ring and at varying intensity as depicted in figure 2.6. This figure shows the wide variety in signal levels of the 26^{th} which is a result both of the total intensity and of the distribution of protons in the buckets around the ring. This figure also shows that the largest 26^{th} harmonic is obtained for 12 booster batches and that the power generally increases with increasing intensity for a given number of batches.

A quantitative study of the dependence of the size of the 26^{th} harmonic on the total intensity was made using the 12 booster batch data taken during the 7 data runs described in chapter 5. The result is shown in figure 2.7 and demonstrates that the power increases with the square of the particle intensity as expected. The solid line represents a linear fit to the data which exhibits a slope of $2.3 \pm .4$.

In addition to measuring the various harmonics at flattop, measurements of the frequency shift during the ramp portion of the cycle for the 1113^{th} harmonic were also made. Figure 2.8 shows one such measurement with the 3561A FFT placed in a measure and update

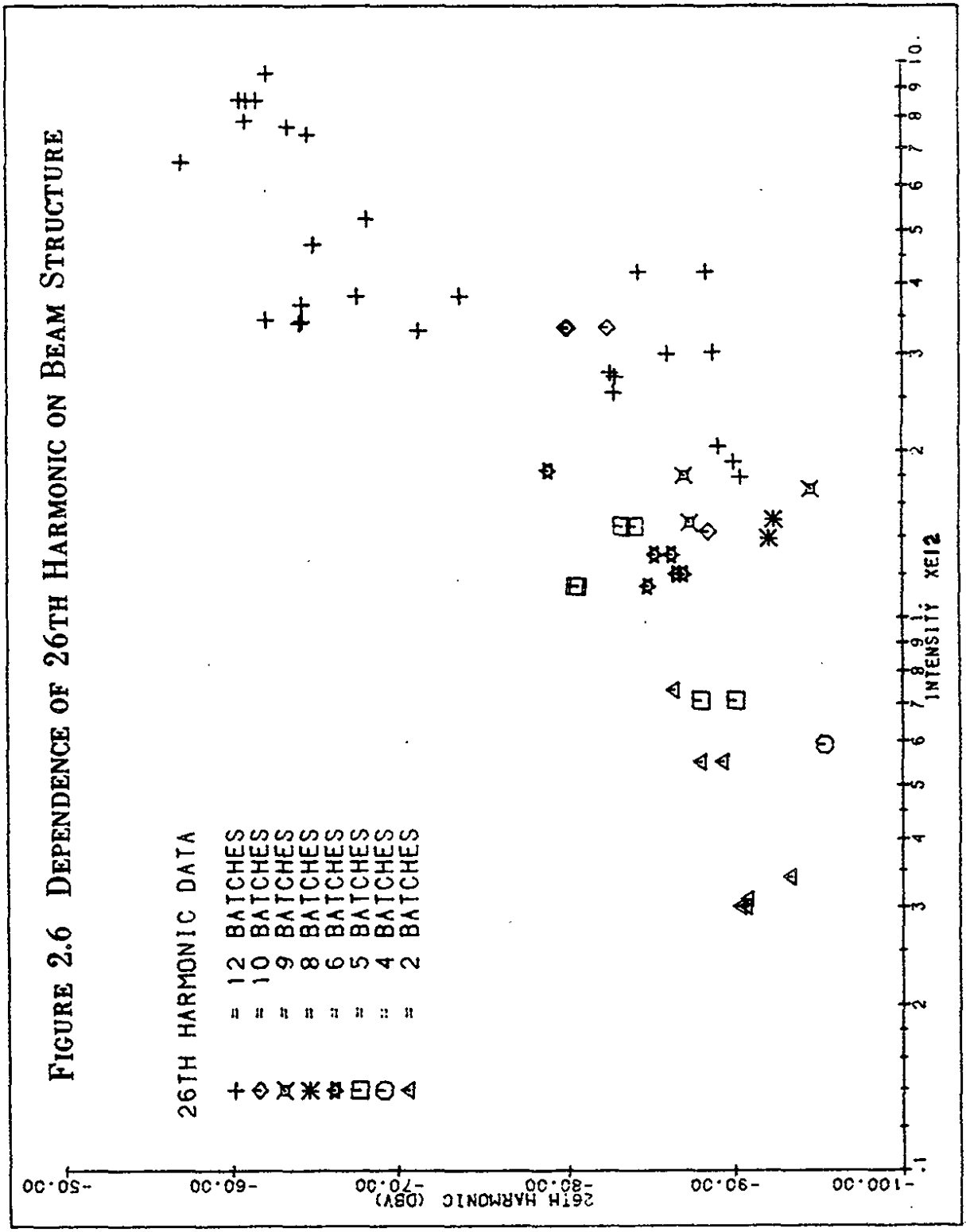

FIGURE 2.6 DEPENDENCE OF 26TH HARMONIC ON BEAM STRUCTURE

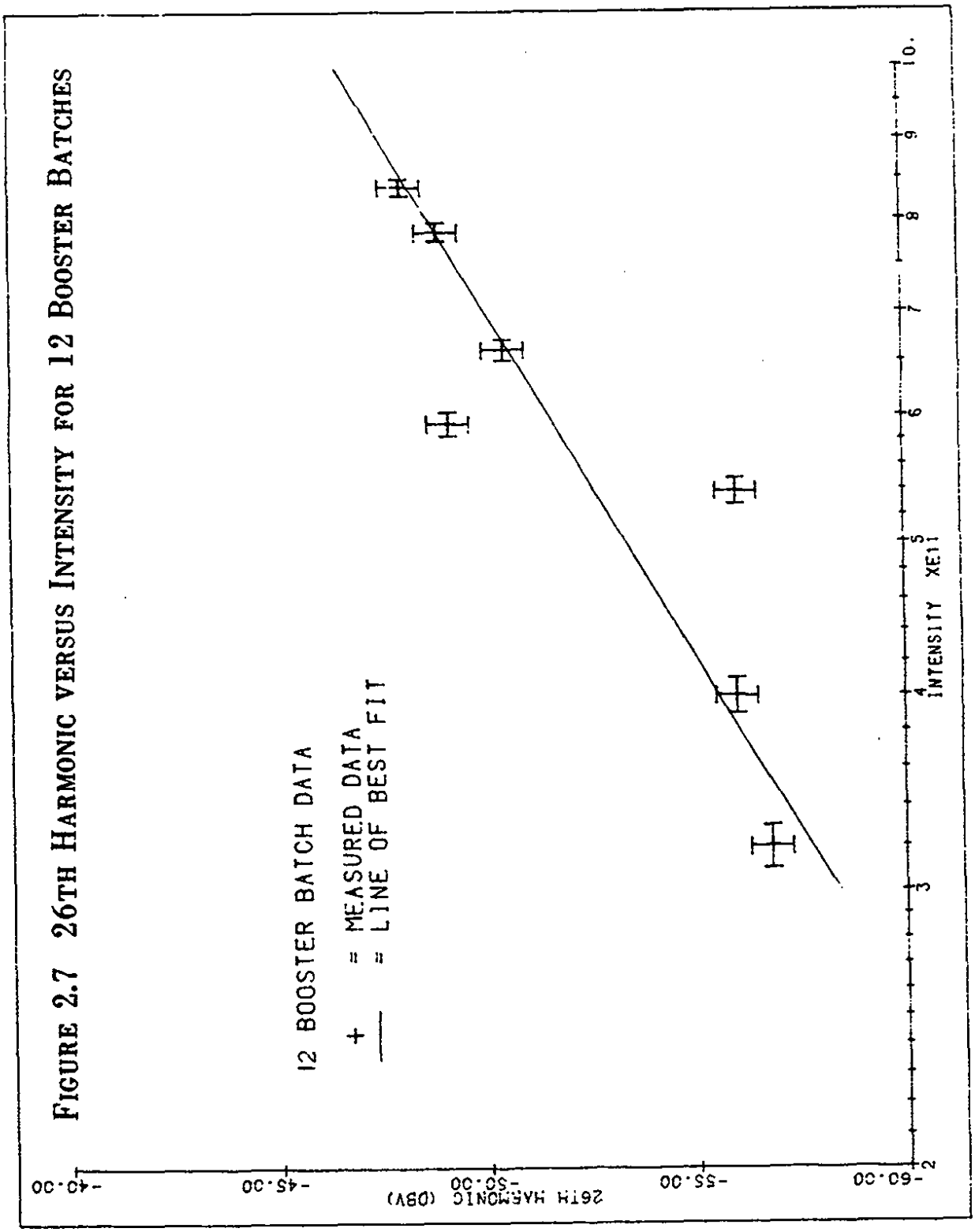

FIGURE 2.7 26TH HARMONIC VERSUS INTENSITY FOR 12 BOOSTER BATCHES

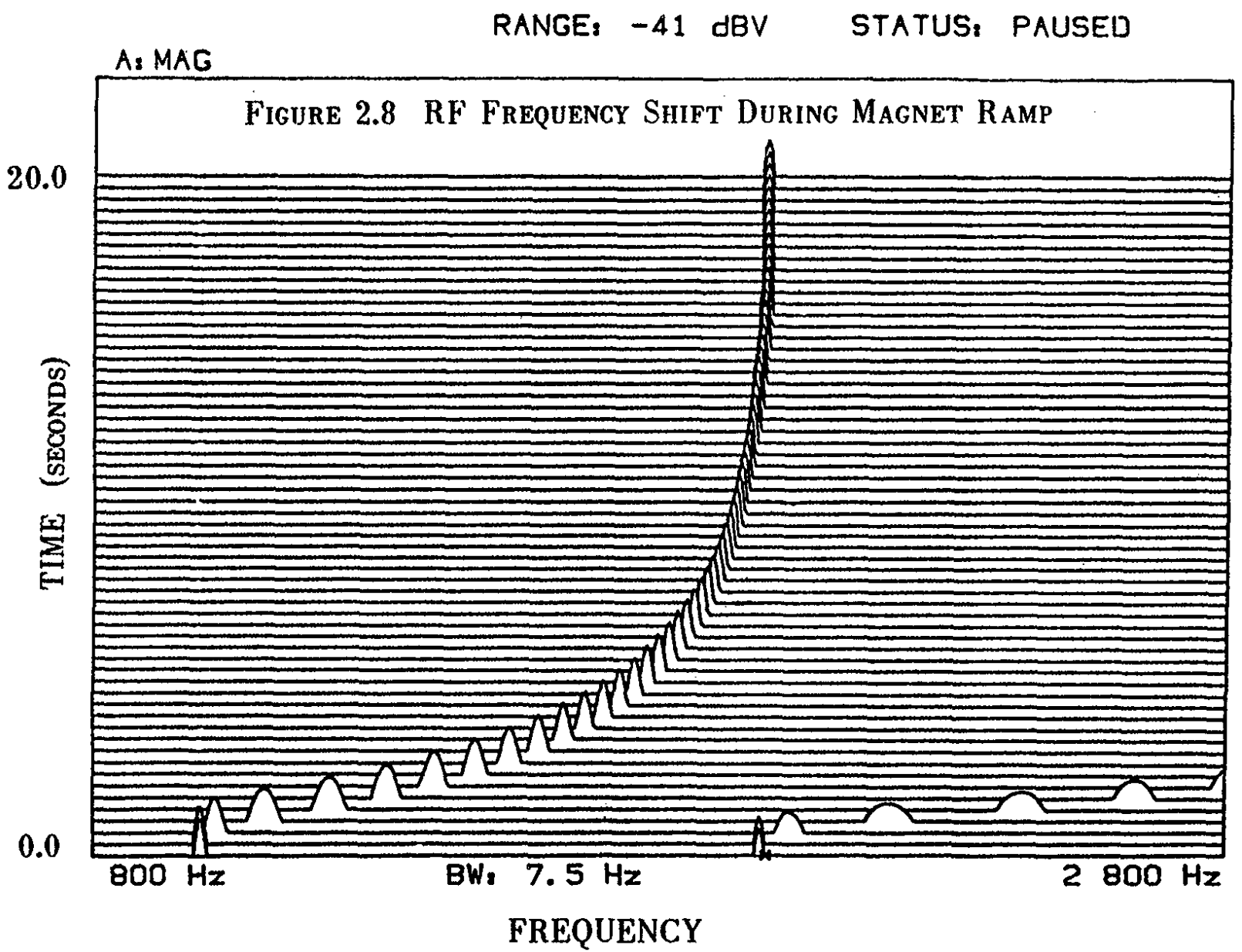

FIGURE 2.8 RF FREQUENCY SHIFT DURING MAGNET RAMP

mode so that it measured the 1113^{th} harmonic at successive time intervals. From this plot we can see that the fundamental RF frequency changes by 1001±1 Hz from the start of the magnet ramp at 150 GeV to the start of flattop at 800 GeV. A detailed analysis of this data is given in Appendix A and is used as a high precision confirmation of special relativity.

2.5 Effective Gravitational Mass

The gravitational potential at the position of a massive detector for a single particle of mass m as previously given is

$$h^{00} = \frac{2GNm_p(2\gamma^2\beta^2+1)}{c^2(y^2+\gamma^2\beta^2c^2t^2)^{\frac{1}{2}}} \tag{2.4}$$

The actual particle density is gaussian so that for a single bunch,

$$\rho(t) = \frac{m}{\sqrt{2\pi}\sigma} e^{\frac{1}{2}t^2/\sigma^2} \tag{2.5}$$

The Fourier amplitude of h_{00} at frequency ω_0 is then

$$h_{00} = \frac{4Gm_p\gamma N}{\pi Rc^2} \log\left(\frac{2\pi\gamma R}{b}\right) \tag{2.6}$$

To obtain the actual Fourier amplitude at the 26^{th} harmonic from the measured value h_{26} of the 26^{th} harmonic from the beam position monitor, we need only multiply h_{00} by the ratio of the 26^{th} harmonic to the 1113^{th}.

$$(h_{00})_{26} = h_{00}\left(\frac{h_{26}}{h_{1113}}\right) \tag{2.7}$$

This is equivalent to calculating the "effective" gravitational mass m_{eff} from the number of protons (N) in the beam.

$$m_{eff} = m_p N \left(\frac{h_{26}}{h_{1113}}\right) \tag{2.8}$$

Chapter 3

Operation of a Parametric Transducer

3.1 Introduction

The extremely small size of the gravitational effects between particle beams and a massive detector necessitates a highly sensitive transducer and careful use of a variety of signal processing techniques. As the primary stage of our detection scheme we have chosen to use a superconducting , coupled cavity parametric converter transducer.

The transducer is a resonant two-mode microwave cavity system with a precisely defined difference frequency between the two modes. This system has the useful property that any harmonic time perturbation in the inductance or capacitance of the system at the difference frequency can couple energy from one mode to the other. In this application, we try to measure the transfer of energy resulting from perturbations in the dimensions of the transducer due to the passage of the bunched proton beam near the detector. The detector itself has a sensitivity to small harmonic displacements of 1.3×10^{-17} cm.

The basic theory of operation of a parametric converter is given in section 3.2 and a discussion of the sensitivity of the transducer

to a given force is given in section 3.3. Section 3.4 describes the noise limitations of the particular detection system used here and outlines the techniques used to detect small signals in the presence of noise.

3.2 Transducer

The cavity transducer consists of a set of TE_{011} superconducting Niobium cavities coupled together by an iris in a common endwall. The resultant cavity system as shown in figure 3.1 has two orthogonal modes which we label f_1 and f_2. The frequency splitting Δf_N of the two modes is governed primarily by the coupling (K) between the cavities and the unperturbed frequencies of the two individual (uncoupled) cavities f_{01} and f_{02}. The coupling K depends upon the geometry of the coupling hole between the cavities. The dependence on f_{01} and f_{02} allows the precise adjustment of the frequency splitting by changing the length (longitudinal dimension) of one of the cavity halves with a worm gear assembly (section 4.1).

The expression for Δf_N is given below.

$$\Delta f_N = \sqrt{(f_{01}-f_{02})^2+K^2 f_{01} f_{02}} \qquad (3.1)$$

From this expression we see that Δf can be minimized by making f_{01} and f_{02} identical so that $\Delta f_{min}=Kf_0$. For this investigation, Δf_N

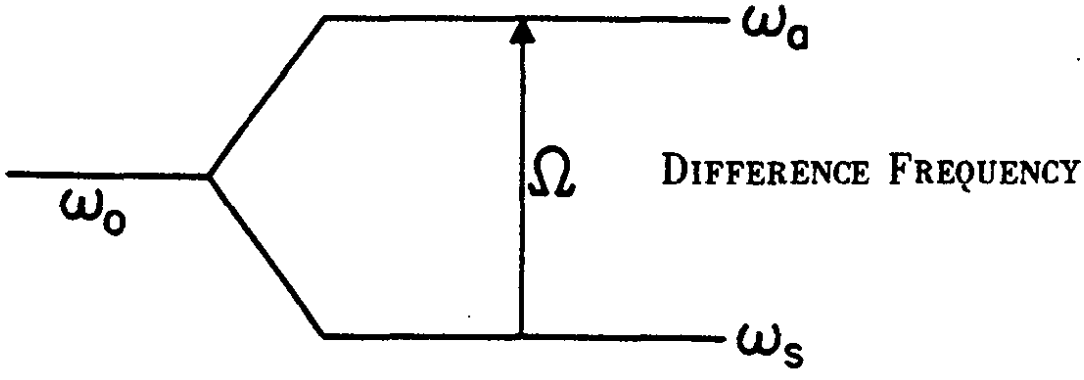

RESONANT MODES

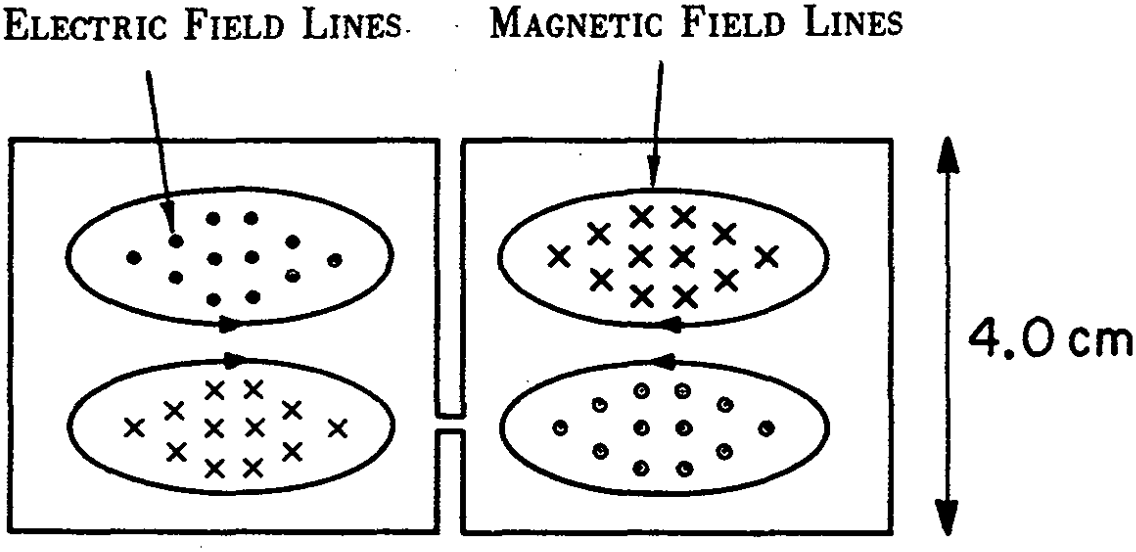

ANTISYMMETRIC TE_{011} MODE

FIGURE 3.1 ELECTROMAGNETIC RESONANCES FOR COUPLED CAVITY SYSTEM

was measured to be 1.18 MHz and the total tuning range obtainable for Δf was 1.18 to 1.40 MHz.

In a two-mode parametric converter, one mode is tuned to the pump frequency: For our case, this was f_2. Then, any perturbation at Δf in the common reactance of the cavity will pump energy from one mode into the other. Reece[1] has shown that the resultant energy U_2 stored in mode 2 by parametric conversion from mode 1 due to a cavity endwall displacement of amplitude Δl at the frequency f_p is governed by the following relationship:

$$U_2 = \frac{U_1 Q_2^2}{4} \left[\frac{\Delta l}{27.3\text{cm}} \frac{\Delta f_{min}}{\Delta f_N} \right]^2 \left[\frac{1}{1+4Q_2^2 \Delta^2} \right] \qquad (3.2)$$

Δ is a detuning parameter defined as $\Delta=(\Delta f_N - f_p)/f_2$.

In this expression we see that the energy of the upconverted signal is proportional to the square of the loaded electrical Q of the cavity system. Hence, one would like as high an electrical Q as possible. Also, we would like to keep Δf_N as close as possible to Δf_{min}, and Δ as small as possible.

Since we are detecting the signal U_2, we must introduce the coupling parameters β_1 and β_2 which describe the amount of available power which can be pumped into and out of the cavity system. Then the expression for the effective sensitivity of the transducer to a harmonic displacement of a cavity endwall is given below.

$$\Delta l = 27.3 \left(\frac{\Delta f_N}{\Delta f_{min}} \right) \left[\frac{P_2}{P_1} \frac{1}{Q_1 Q_2} \frac{(\beta_1+1)(\beta_2+1)}{\beta_1 \beta_2} \left\{ \frac{f_2}{f_1} \right\} (1+4Q_2^2 \Delta^2) \right]^{\frac{1}{2}} \quad (3.3)$$

P_1 is the total incident power going into the cavities and P_2 is the signal power which we must detect. To maximize the output power for a given displacement, we set $\beta_1=\beta_2=1.0$. The functional dependence of this expression has been experimentally verified.

3.3 Force Measurement

Now suppose that the cavity endwall can be modeled as a harmonic oscillator subject to a displacement Δl. The familiar Langevin function for the displacement x for a damped oscillator with mechanical $Q=Q_m$ and frequency ω_0 is given by:[2]

$$m\ddot{x} - \left(\frac{m\omega_0}{Q_m} \right) \dot{x} + m\omega_0^2 x = F_g(t) \quad (3.4)$$

For our case, the driving term $F_g(t)$ is the gravitational tidal impulse imparted to the detector by the beam. We can solve for the Fourier transform of x(t) to get

$$\left| x(\omega) \right| = \frac{\left| \frac{F_g(\omega)}{m} \right|}{\left| (\omega_0^2 - \omega^2) + \frac{i\omega_0 \omega}{Q_m} \right|} \tag{3.5}$$

Substituting 3.5 into 3.3 and solving for the average acceleration and setting $\omega=\omega_p$ we get the following expression:

$$\left| \frac{F_g(\omega)}{m} \right| = \Delta l \left[(\omega_0^2 - \omega_p^2)^2 + \left\{ \frac{\omega_p \omega_0}{Q_m} \right\}^2 \right]^{\frac{1}{2}} \tag{3.6}$$

This equation illustrates that the sensitivity of the detector to acceleration increases with mechanical Q and for $\omega=\omega_{0_m}$. That is, for maximum sensitivity, the frequency of the gravitational force must be precisely tuned to the mechanical resonance. Furthermore, this frequency must coincide with the difference frequency of the transducer. In practice, this was very difficult to do since it would require tuning the mechanical resonance of the cavity system to precisely the revolution frequency of the proton beam. Fortunately, the mechanical response consists of a dense set of resonances so that effective coupling with $Q_m \approx 10^3$ was always possible. In addition, care must be taken in using equation 3.6 since it is not clear that the gravitational impulse couples to a single well defined mechanical resonance of the cavity transducer.

Equation 3.6 also assumes that the harmonic oscillator has reached an equilibrium state. For long measurement times, or equivalently, for small mechanical Q_m ($\tau > Q_m/\omega \sim 10^{-4}$ sec) this is not a problem.

3.4 Minimum Detectable Signals

The smallest detectable signals which can be measured with our detector depend not only on the parameters described in section 3.2 but also on the techniques one chooses to observe a given signal. Since the signal of interest is most likely smaller than the noise which is present, we must resort to statistical methods of analysis.[3] We will assume that the noise is random both in amplitude and in phase and that it is independent of frequency (white). This last assumption is valid if the amplifiers, mixers and cavities are broadband compared to the overall bandwidth of the detection system.

The noise figure F for a system is defined as the ratio of the signal to noise at the input to the signal to noise at the output.[4]

$$F = \frac{\left(\frac{S_1}{N_1}\right)}{\left(\frac{S_0}{N_0}\right)} \tag{3.7}$$

The input noise N_i is just the available thermal energy at

temperature T_g multiplied by the effective bandwidth (B) of the system. Solving for the smallest detectable signal from a narrow band detection system we get the following expression:

$$S_{min} = kT_gB\left(\frac{S_o}{N_o}\right)F_{tot} \tag{3.8}$$

This expression shows that the smallest detectable signal is directly proportional to the total noise figure of the system as well as the detection bandwidth. The total noise figure is given by

$$F_{tot} = F_1 + \frac{F_2-1}{G_1} + \cdots + \frac{F_N-1}{G_1G_2\cdots G_N} \tag{3.9}$$

where F_i and G_i are the noise figure and gain of the i^{th} amplifier.

At first glance, it appears that the smallest detectable signal can be achieved by simply integrating the output power of the detector over the longest available time period, and hence achieving the smallest bandwidth possible. However, this is not the case since the signal of interest has some small but finite bandwidth. If the detection bandwidth is smaller than the signal bandwidth, then no improvement in the signal to noise ratio can be achieved since the total available signal power will be distributed over a band of frequencies and hence, the signal power at a given frequency

will decrease at the same rate as the noise. Thus the limitation on the effective bandwidth is governed by the bandwidth of the signal of interest.

The output signal to noise ratio is usually assumed to be greater than or equal to one for a "reasonable" experiment and in particular for a single measurement. However, this need not be the case, if several equivalent measurements can be made and an ensemble average performed.

For our detector two different statistical averaging techniques can be used to establish the best possible output signal to noise ratio.[5] For both techniques, we assume that the output signal is a voltage V(t) which consists of a gaussian random noise signal N(t) and the deterministic signal S(t) that we are interested in. The noise signal is assumed to have zero mean and a variance σ. Thus the detected voltage is

$$V(t) = S(t) + N(t) \tag{3.10}$$

Both S and N are assumed to be periodic at the frequency of interest and we are interested in analyzing the narrow band output spectrum of the detector.

The first averaging technique is based on the power average of k records as defined below.

$$\langle \text{Power} \rangle = \frac{C}{k} \sum_{j=1}^{k} V_j(t)$$

$$\left\langle \text{Power} \right\rangle = \frac{C}{k} \sum_{i=1}^{k} \left\{ S_i^2(t) + N_i^2(t) + S_i(t)N_i(t) \right\} \qquad (3.11)$$

The last term vanishes for large k since S(t) and N(t) are uncorrelated, so that

$$\langle V^2 \rangle = \langle S^2 \rangle + \langle N^2 \rangle$$

where

$$\frac{1}{k} \sum_{i=1}^{k} S^2(t) = \langle S^2 \rangle$$

Now, we define the average noise power to be the variance σ^2 of the noise voltage since the average noise voltage is zero. Since each measurement is equivalent (assuming all parameters remain fixed for each measurement) the actual magnitude of the random noise power given by σ^2 is constant so that the signal to noise ratio is also constant. Thus, there is no improvement in the signal to noise ratio when power averaging is performed. However, we could estimate the maximum size of a signal in the presence of noise if we could subtract σ^2 from the average power in the bin of interest.

$$\langle S_0^2 \rangle = \langle V^2 \rangle - \sigma^2 \qquad (3.12)$$

Now, we do not know σ^2 exactly since we only observe a finite number of spectra, but we can estimate σ^2 with the following estimator ($\hat{S}^2$):

$$\hat{S}^2 = \frac{k\Sigma V_i^2 - (\Sigma V_i)^2}{k(k-1)} \qquad (3.13)$$

This statistic can be shown to have a Chi-squared distribution[6] so that we can define a confidence interval for $\langle \hat{S}^2 \rangle$ as follows: For a $(1-\alpha)100\%$ confidence estimate of σ^2 from a random sample of size k, $(k>30)$

$$\langle V^2 \rangle - \frac{(k-1)\hat{S}^2}{\chi^2_{1-\alpha/2}} < S_0^2 < \langle V^2 \rangle - \frac{(k-1)\hat{S}^2}{\chi^2_{\alpha/2}} \qquad (3.14)$$

The other available analysis option utilizes a voltage average of the output signal from the cavity transducer. Since the signal voltage is periodic in time we must have a method of averaging the voltages in such a way that the signals of interest S(t) all add in phase. This can be accomplished by using a second noiseless signal at the same frequency which has a constant phase relationship with the desired signal of interest, or in other words, we must have a signal which is correlated in time with the signal of interest.[7] For

this investigation, the beam intensity signal is correlated in time with the expected upconverted signal and thus provides the noiseless signal with which to correlate the detected signals. We could for such a case add successive time records together such that we start at the same point in the period of the waveform for each record. In this case we have,

$$\left\langle V(\omega)\right\rangle = \frac{1}{k}\sum \left\{S_0(\omega) + N_0(\omega)\right\} \tag{3.15}$$

and

$$\frac{1}{k}\sum S_0(\omega) = S_0(\omega)$$

Again however, the average noise voltage is zero but the noise power is defined as the variance in the noise. From the theory of maximum likelihood[8], we can show that for k records averaged together,

$$\sigma_k^2 = \frac{\sigma^2}{k} \tag{3.16}$$

where σ^2 is the variance in the voltage for one record. Thus

$$\langle N \rangle = \frac{\sigma}{\sqrt{K}} \tag{3.17}$$

Here, the signal to noise power ratio improves and is given as follows:

$$\frac{S}{N} = \frac{kS_0^2}{N_0^2} \tag{3.18}$$

Thus the minimum detectable signal is given below.

$$S_{min} = kTB\left(\frac{kS_0^2}{N_0^2}\right)F \tag{3.19}$$

Alternatively, we can calculate the coherence function ξ between the output of the detector and the beam intensity signal.[9] This procedure is outlined below. We assume that the output of the detector is given by $A(\omega)$ and consists of the desired deterministic signal $X(\omega)$ and a noise term $N(\omega)$.

$$A(\omega) = X(\omega)+N(\omega) \tag{3.20}$$

The corresponding output of the beam pick-up is denoted by $B(\omega)$ and has the form

$$B(\omega) = k(\omega)X(\omega) \tag{3.21}$$

swhere $k(\omega)$ is a well defined function. The coherence coefficient ξ is defined at each frequency as[10]

$$\xi^2 = \frac{\langle B^*A \rangle \langle A^*B \rangle}{\langle A^*A \rangle \langle B^*B \rangle} \tag{3.22}$$

The brackets indicate an ensemble average for each of the quantities. The average power in signal A is

$$\langle A^*A \rangle = \langle X^*X \rangle + \langle N^*N \rangle + \langle AN^* \rangle + \langle A^*N \rangle \tag{3.23}$$

The last two terms in this expression vanish for sufficiently large averages since the noise is not correlated with the expected signal. The average cross term for A and B is

$$\langle AB^* \rangle = k\langle X^*X \rangle + k\langle NX^* \rangle \tag{3.23a}$$

so that the coherence function squared for large averages is

$$\xi^2 = \frac{\langle X^* X \rangle}{\langle X^* X \rangle + \langle N^* N \rangle} \tag{3.24}$$

From this expression the average noise power is

$$N(\omega) = \left(1-\xi^2\right)\langle A^*(\omega)A(\omega)\rangle \tag{3.25}$$

and the desired signal is

$$S(\omega) = \xi^2 \langle A^* A \rangle \tag{3.26}$$

The power signal to noise ratio of this analysis is then given by:

$$\frac{S}{N} = \frac{\xi^2}{(1-\xi^2)} \tag{3.27}$$

In order to take advantage of this scheme a detection system is needed capable of measuring both signals $A(\omega)$ and $B(\omega)$ simultaneously. Such a scheme was developed and is discussed in section 4.7.

The minimum detectable acceleration can be derived by assuming the driving term in the Langevin equation to be given by the energy in the thermal bath surrounding the detector.[10] For such a case, the average available noise power is just

$$\left\langle N^2(\omega_0)\right\rangle = \frac{4kT}{\tau} \tag{3.28}$$

where m is the mass of the mechanical oscillator of frequency f_0 and τ is the relaxation time of the oscillator given by

$$\tau = \frac{Q_m}{\omega_0} \tag{3.29}$$

Substituting this result into equation 3.6 yields

$$\hat{\Delta I}(\omega) = \frac{\left|N^2(\omega_0)\right|^{\frac{1}{2}}}{\left[(\omega_0^2-\omega^2)^2+\left\{\frac{\omega\omega_0}{Q_m}\right\}^2\right]^{\frac{1}{2}}}\sqrt{\frac{1}{m}} \tag{3.30}$$

On resonance, $\omega=\omega_0$ so that the average thermally induced fluctuation in $\hat{\Delta I}$ per $Hz^{\frac{1}{2}}$ for our detector is given by :

$$\hat{\Delta\tilde{I}}(\omega) = \frac{2Q}{m\omega_0^2}\sqrt{\frac{kTm\omega_0}{Q}} = \sqrt{\frac{Q}{\omega_0}}\sqrt{\frac{4kT}{m\omega_0^2}} \qquad (3.31)$$

References

1. C.E. Reece, Report No. UR-867, Department of Physics and Astronomy, University of Rochester, Rochester, N.Y. (1983) (PhD. Thesis, unpublished).

2. S. Chandrasekhar, Rev. Mod. Phys., 15,No. 1, Jan 1943.

3. J.S. Bendat, Principles and Applications of Random Noise Theory, (John Wiley & Sons, Inc., 1958)

4. W.B. Davenport Jr., and W.L. Root, Random Signals and Noise (McGraw-Hill Book Company Inc., 1958) pp207-212.

5. Hewlett Packard Co. Application Notes, AN 245-1, "Signal Averaging with the HP-3582A Spectrum Analyzer", and AN 245-2, "Measuring the Coherence Function with the HP-3582A Spectrum Analyzer".

6. R.E. Walpole, R.H. Meyers, Probability and Statistics for Engineers and Scientists, 2nd Edition (Macmillan Publishing Co., Inc., NY, 1978) 172-4.

7. J.S. Bendat, Op cit., 93-96.

8. A.C. Melissinos, Experiments in Modern Physics, (Academic Press, N.Y., 1966) 459-471.

9. P. Roth, Sound and Vibration, "How to Use the Spectrum and Coherence Function," Jan. 1971.

10. Hewlett Packard Application Note AN 245-2, Op cit.

11. J. Beck, Statistical Mechanics, Fluctuations and Noise, (Halsted Press, N.Y., 1976) 167-169.

Chapter 4

Experimental Apparatus

4.1 Introduction

The operation of the superconducting parametric cavity transducer in a high energy accelerator environment posed many challenging problems. High radiation levels from the particle spray of the beam prevented access to the cryostat during HEP (high energy physics) running periods. This necessitated the development of reliable remote control systems for tuning of the cavity system and control of the microwave electronics.

Figure 4.1 shows a top view of the position of the detector in relationship to the tunnel housing the Tevatron and the CO Spectrometer Room. In order to provide limited access to the microwave controls and to the cryogenic control system during HEP operation of the beam, the microwave electronics, storage dewars, and vacuum pumps were placed behind a 15 foot thick concrete shield inside the CO Spectrometer Room. This also prevented possible radiation damage to the solid state circuitry that was part of the detection system. The computer and data acquisition system as well as the bulk of the detection electronics were housed in a Porta-Kamp located near the spectrometer room roof.

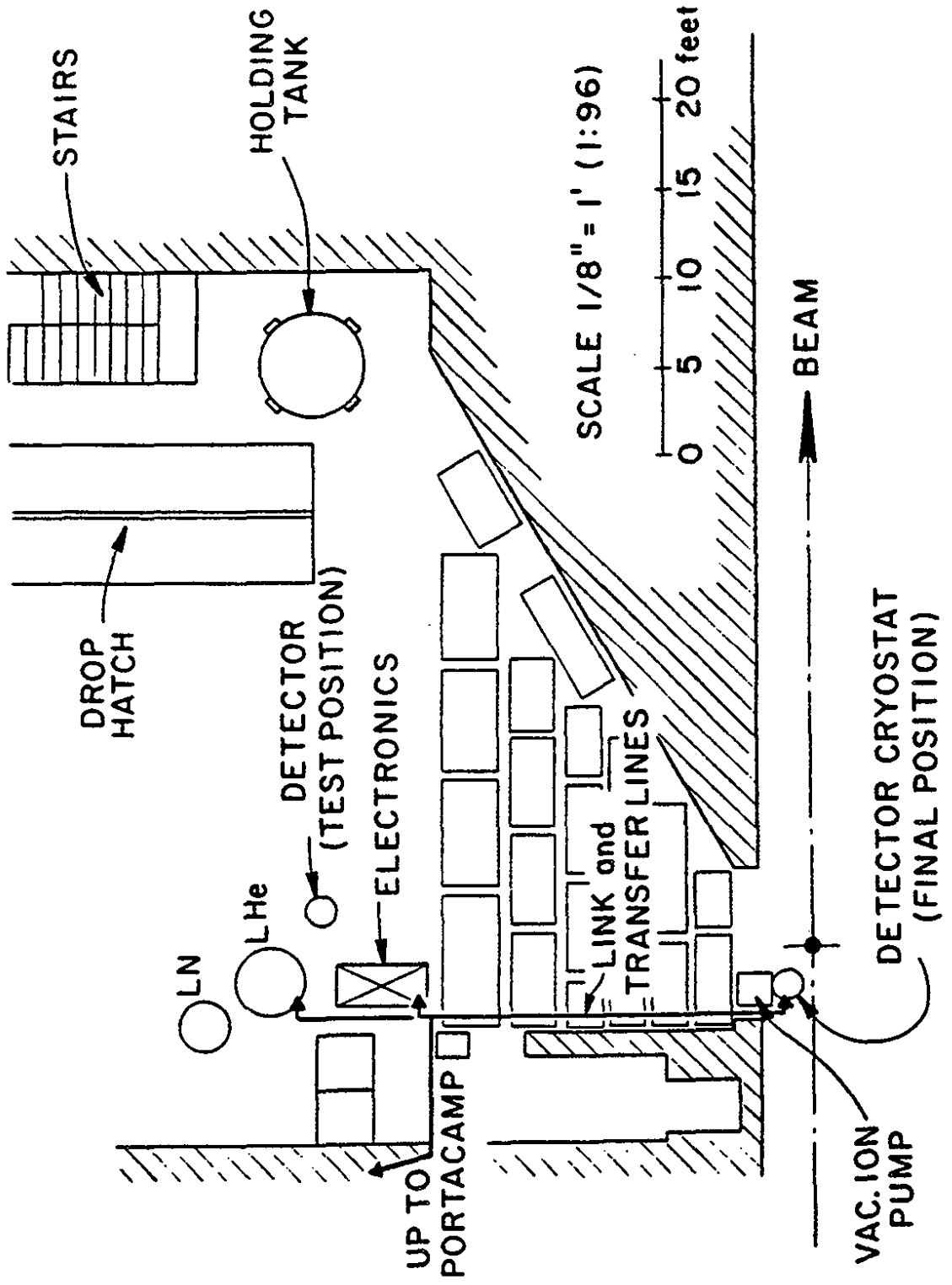

FIGURE 4.1 TOP VIEW OF DETECTOR LOCATION

The first section (4.2) describes the microwave cavity system ,the microwave transmission lines which couple energy into and out of the detector and the remote control system. Section 4.3 describes the microwave control electronics and in particular, the waveguide hybrid tee used to discriminate the pump frequency from the upconverted signal. The next section details the cryogenic apparatus needed to transport the cryogens from the spectrometer room to the cryostat safely and efficiently.

Calibration of the response of the detector to various mechanical excitations was achieved with the use of strain gauges and a piezoelectric crystal mounted on the cavities. These devices are described in section 4.5. Section 4.6 discusses the beam position monitor which provides direct information as to the "effective" gravitational mass of the beam as well as the phase information needed for the correlation of beam induced signals with the passage of the beam near our detector.

The three basic detection schemes used in this investigation are described in section 4.7. The total gains and noise figures for each scheme are tabulated.

Finally, the computer based data acquisition system is outlined in section 4.8. A basic description of the off-line data analysis for each of the three detection schemes is also given.

4.2 Microwave Cavities and Transmission Lines

The microwave cavities consist of two right circular cylinders placed end to end and coupled through an iris in their common endwall as shown in figure 4.2. Coupling to the cavities is accomplished through two coupling tubes with flanges welded in place. The cavities are each 1.55 inches in length and have an inner diameter of 1.55 inches so that they have a resonant frequency of 9.94 GHz in the TE_{011} mode. One of the cavity halves has an endwall which is slightly flexible to allow for the precise tuning of the cavity difference frequency. A worm gear assembly was mounted on this endwall which was designed to displace the endwall in order to change the length dimension of the cavity in either direction. The rotating shaft of the worm gear assembly extended through a vacuum tight Cajon Connector on the top of the cryostat from where it could easily be adjusted.

The opposite cavity half had an endwall which was .279 cm thick and designed to resonate mechanically at about 600 kHz when driven longitudinally by a piezoelectric transducer mounted on the outside end. All of the cavity pieces were machined from "reactor grade" Niobium stock and were electron beam welded under high vacuum. The cavity surfaces were cleaned and polished using several techniques[1] to achieve unloaded electrical Q_e as high as 1.0×10^9.

The two modes of the cavity system were measured to be 9.94438 GHz and 9.94562 GHz with electrical Q_0 of $\sim6\times10^7$ at 1.89°K and $\sim2\times10^7$ at 4.2°K.

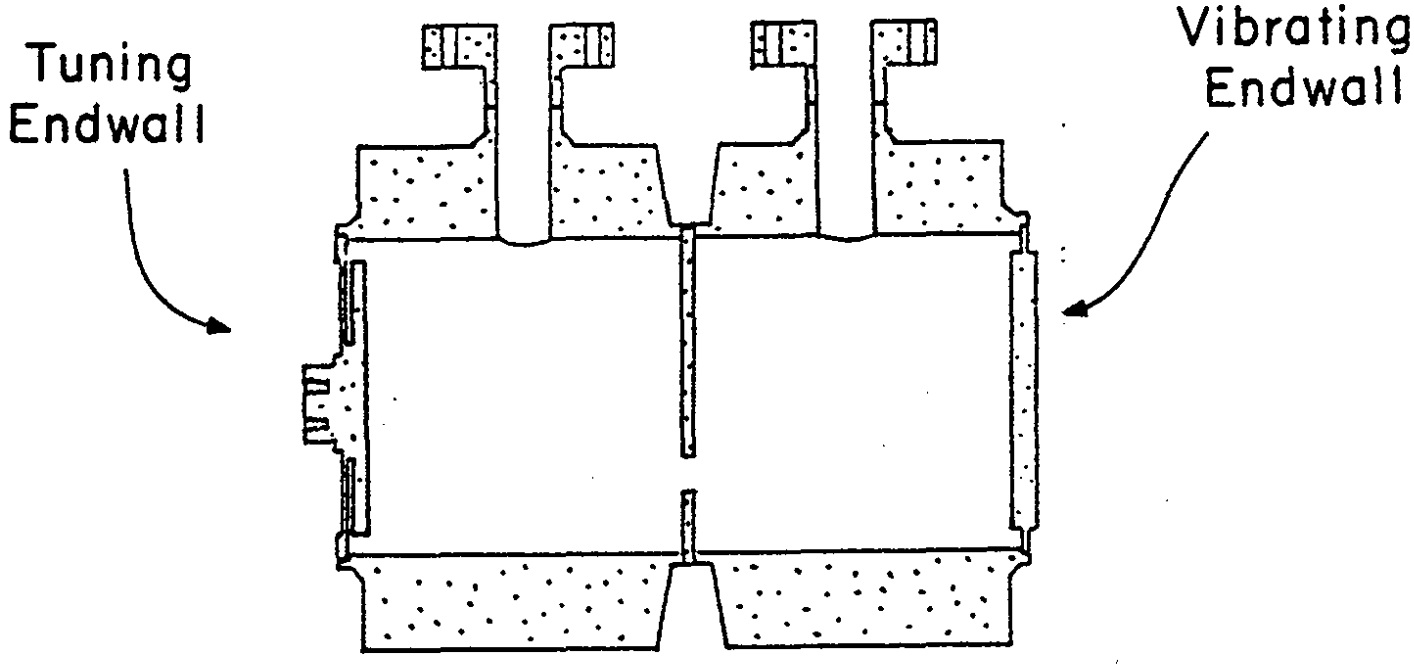

FIGURE 4.2 MICROWAVE CAVITY TRANSDUCER

The transmission lines to the cavities were mounted on flexible bellows at the top of the cryostat with high-vacuum SMA feedthrough connectors as shown in figure 4.3. Remote control positioning of the lines was accomplished by mounting D.C. stepping motors with a worm gear assembly attached to the end of a threaded screw adjustment. The motors were driven by a Camac Module 044 driver which optionally could be controlled via computer. This module was used to control a stepping motor driving circuit designed specifically for D.C. stepping motors. With this system, it was possible to precisely control the probe positions to within $(1.0\pm.1)\times10^{-5}$ cm per motor pulse with an average change in position of $(7.4\pm1.0)\times10^{-6}$ cm per pulse. Limit switches were fastened to the probe adjustment assemblies to restrict the total travel of the probes and prevent damage to the bellows.

Remote control of the Δf tuning was accomplished by mounting a similar motor with another worm gear assembly on the tuning shaft (of the worm gear assembly used to position the moveable endwall outside of the cryostat. During operation, this provided for ~50 Hz per pulse tuning of the difference frequency with a total tuning range of Δf of ±20 kHz. The assembly was carefully adjusted so that the difference frequency was approximately 1.2405 MHz at the center of its available tuning range.

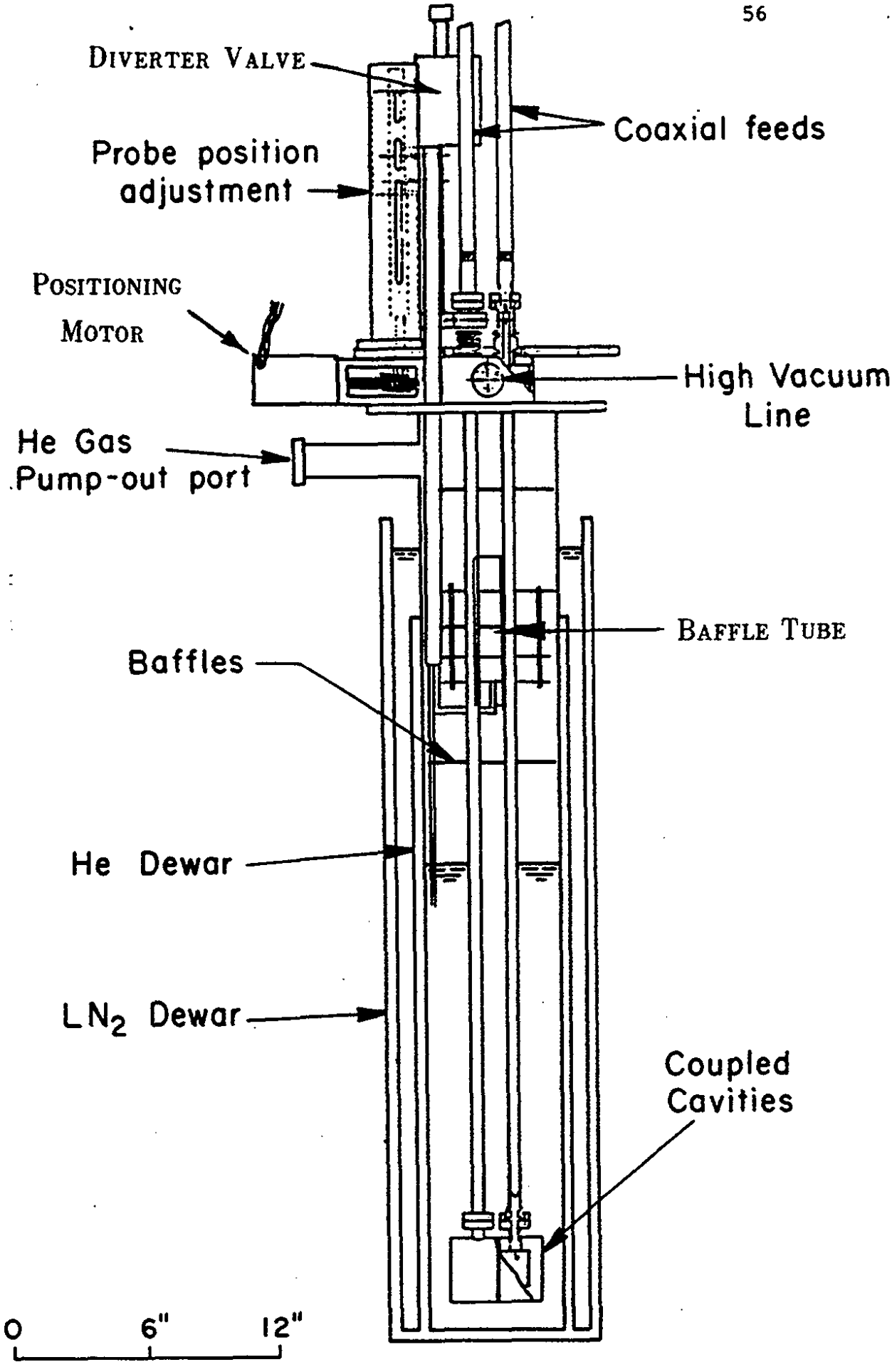

Figure 4.3 Cryostat Assembly

4.3 Microwave Stabalized Oscillator Control System

The microwave control system is shown in figure 4.4. The generator for the microwave power consisted of a varactor-tuned Gunn effect oscillator model VSX-9011-NF manufactured by Varian Corporation. This generator was phase locked to the cavity mode resonant at 9.945620 GHz. The oscillator provided 200 mW output power and was mechanically tuneable over a 500 MHz range and had an electronic tuning range of 30 MHz centered near 10 GHz.

The oscillator output is protected from large reflected signals by a ferrite isolator. A Model 8430-124D high speed PIN switch made by Microwave Associates was remotely controlled and could be opened or closed electronically with a switching time of less than 30 nsec. As shown in the diagram, part of the power is then split off with a 6 dB directional coupler and fed into a 3 dB hybrid splitter. This provided the necessary +7 dBm local oscilator power for both the phase locking microwave mixer and the signal detection mixer. The small signal at the delta port of the splitter was used to drive a HP5342A Frequency Counter.

The primary signal from the output port of the 6 dB directional coupler was fed into a directional coupler followed by the symmetric port of the hybrid tee.

The hybrid tee split the incoming signal into two equal amplitude and equal phase signals which in turn fed 24' sections of RG90 waveguide. Each section of waveguide had a microwave phase shifter on the end which was located in the shielded CO Spectrometer

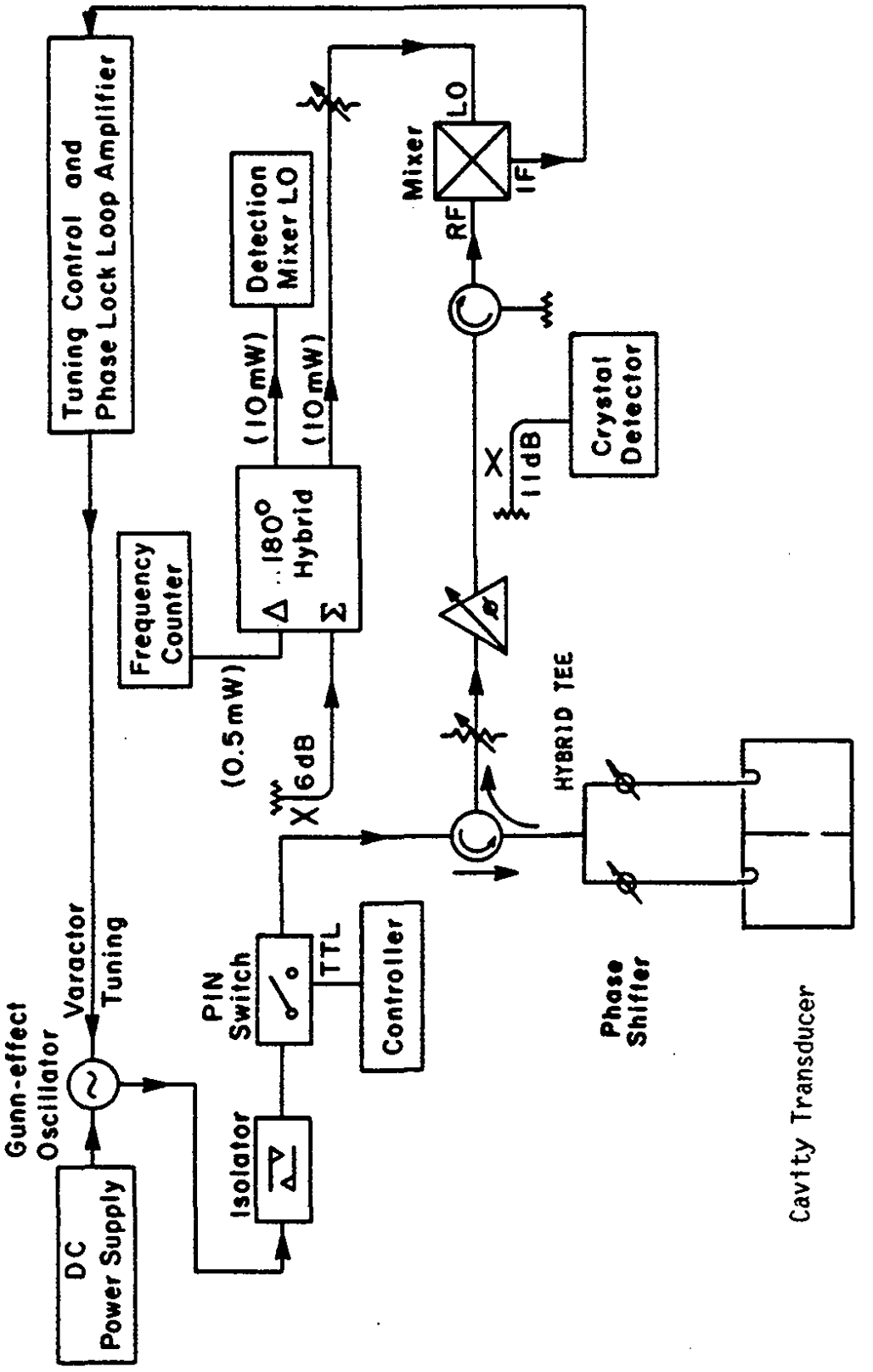

FIGURE 4.4 MICROWAVE EXCITATION AND CONTROL ELECTRONICS

room area. The waveguide carried the microwave signals into the CO tunnel area and to the transmission lines of the cavities. Coaxial stub tuners were used to prevent excessive reflection of the microwaves due to the impedance mismatches in the lines. The overall attenuation between the output ports of the hybrid tee and the input ports of the transmission lines was measured to be 4.84 dB for one of the lines and 4.94 dB for the other.

Reflected power at 9.94562 GHz from the cavities travelled back out the symmetric port of the hybrid tee and was split off with the 10 dB directional coupler. This signal was then fed into an attenuator followed by a phase shifter and finally a microwave mixer. The output of the mixer carried the necessary phase information for the reference locking system and was fed into a phase lock loop amplifier (PLLA).[2]

The PLLA had a low frequency gain of 0 to 80 db selectable in 20 dB steps and variable high frequency gain. The output of the PLLA could be remotely controlled because the module was located in the CO spectrometer room near the microwave control equipment. The output of the PLLA provided the electronic tuning for the Gunn oscillator. The frequency drift of the oscillator was observed to be ~10 Hz/30 min with 80 dB low frequency gain and ~10 Hz/min with 0 dB gain. The corresponding long term drift was ~50 Hz/hr.

The microwave hybrid tee used to feed the microwave lines to the cavities served another important purpose. The signal produced in the upconversion process is 180° out of phase with the incoming signal into the cavities. The hybrid tee is designed to allow the

signal applied to the symmetric port to be split into equal amplitude equal phase signals as already described. The upconverted signals travel from the two ports back out the waveguide lines and recombine at the delta port of the hybrid tee. By carefully balancing the phase and amplitude of the output arms of the hybrid tee using the phase shifters and stub tuners, it was possible to achieve ~75 dB isolation between the Σ and Δ ports of the tee at the input frequency to the cavities. The ability to discriminate against the input frequency at the delta port of the tee was essential to prevent saturation of the low noise amplifier used to detect the upconverted signal.

4.4 Cryogenic System

The microwave cavities were mounted and cooled inside a 6 inch diameter Model CSM-60 dewar manufactured by Cryofab Inc.. The dewar was located inside the tunnel and near the proton beam line as shown in figure 4.1. Mu metal was placed around the dewar in order to attenuate magnetic fields and avoid flux trapping during cooldown of the detector.

The microwave cavities were mounted on a flatplate located at the end of two ½" stainless steel tubes. The tubes housed the microwave transmission lines and provided the high vacuum pumpout ports for the cavities. The cavities were then evacuated to $\sim 6\times10^{-8}$ Torr with a Varian 30 l/s Vac-Ion Pump. Indium wire O-rings

provided the necessary vacuum seal between the cavity flanges and the flatplate and allowed the system to be thermally cycled from 4° to room temperature repeatedly without any noticeable vacuum leaks.

The liquid Helium was transported by a 20 foot transfer line which extended from the storage dewar in the CO spectrometer room into the cryostat in the tunnel. Warm gas from the cryostat was vented through a 2" diameter copper line connected to the CSM-60 dewar. This line also provided the pumpout port for the Helium space in the cryostat during low temperature operations. Temperatures of 1.89° K were achieved by pumping on this line with a 85.5 cfm Roots Blower Pump located in the spectrometer room. During a typical cold run, the pump could evacuate the entire system and reach temperatures below the lambda point of Helium in less than two hours.

A very inexpensive and reasonably efficient liquid Nitrogen transfer line was constructed from $\frac{3}{8}$" copper tubing surrounded by two layers of aluminized mylar followed by common household pipe insulation. The entire assembly was housed inside a 2" copper pipe which extended into the tunnel.

The level of liquid Nitrogen was automatically controlled using a capacitance probe and a LN_2 level controller. The level of liquid Helium inside the dewar was monitored by a KE-101e Helium level meter and the bath temperature was monitored using a Germanium resistance thermometer manufactured and calibrated by Lake Shore Cryogenics Corp.

A diverter valve was constructed to make possible the refilling of the dewar without excessive boil-off of the remaining liquid Helium. The boiloff is due to the flow of the warm gas from the Helium transfer produced as the line is cooled down during the first stages of transfer. Figure 4.5 shows the construction of the diverter valve. The valve consisted of an intake port which connected to the LHe transfer line and two exhaust ports which could be remotely controlled using two solenoids. One exhaust port directed the liquid cryogen to the bottom of the dewar while the other ended in a stainless steel U-tube connected to a baffle tube at the top of the dewar as shown in figure 4.3. Thermal isolation of the LHe bath was provided by two stages of baffles consisting of alternating layers of G-10 and Aluminum.

The baffle tube consisted of a G-10 tube 5 inches long and ~1.25 inches wide with interleaving baffle plates inside. These were spaced so as to allow the separation of two-stage Helium during the transfer process. The liquid Helium could be directed to the bottom of the dewar during initial cooldowns or diverted to the top of the dewar without disturbing the Helium bath below it. During a typical "cold" transfer, only 1 or 2 liters of the Helium bath would be lost during the 30 minute cooldown of the transfer line. The consumption rate of liquid Helium was typically 1 liter per hour during the running periods and approximately .5 liters per hour with the microwaves turned off.

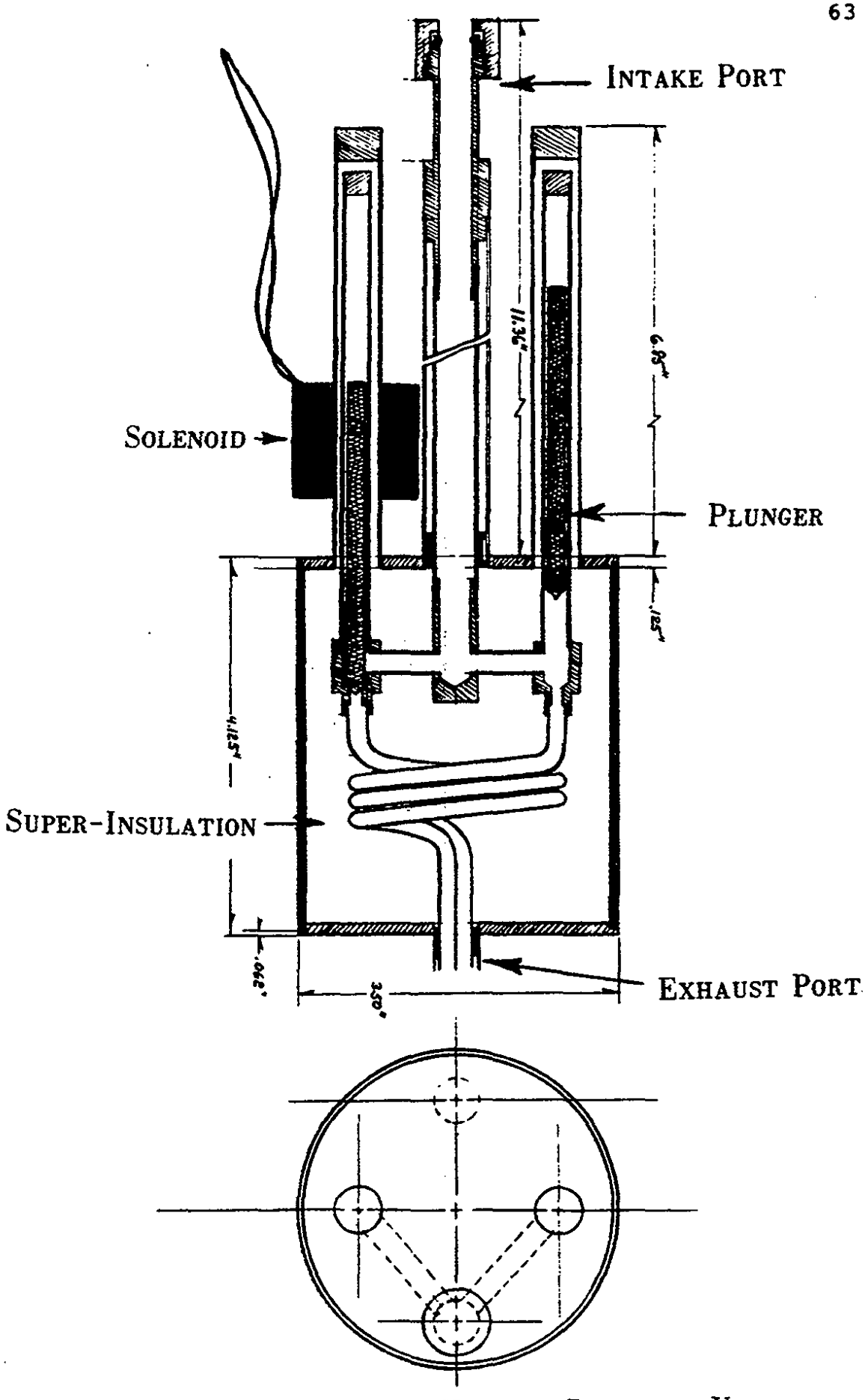

FIGURE 4.5 SECTIONAL VIEW OF DIVERTER VALVE

4.5 Piezoelectric Crystal and Strain Gauges

In order to perform a calibration of the sensitivity of the detector to effective mechanical strains on the cavity walls, a piezoelectric ceramic disk (PZT) was mounted on the moving endwall of the cavity as shown in figure 4.6. In addition, three strain gauges were mounted in the positions shown on the outside of the cavity surface. The PZT was a flat disk 3.81 cm in diameter and .1" thick constructed of a ceramic material commonly called PZT-5A (lead zirconate-titanate) manufactured by Valpey Fischer Corp. The PZT mounting scheme is detailed in reference 3.

The strain gauges were made from the same material and were glued to the cavity using GE Electrical Varnish. Each strain gauge was connected to individually shielded, twisted lead pairs of wires. During a calibration run, the signal from the beam position monitor was amplified and filtered at the 26^{th} harmonic and connected to each one of the strain gauges or the PZT. The resulting upconverted signal was measured and recorded on tape.

4.6 Beam Intensity Monitor

The beam intensity monitor consists of two 18 cm long copper electrodes mounted inside a 10.2 cm diameter stainless steel beam pipe as shown in figure 4.7. Each electrode is bent in a 3.5 cm radius curve and subtends 110° centered around the axis of the beam pipe as shown in the diagram.

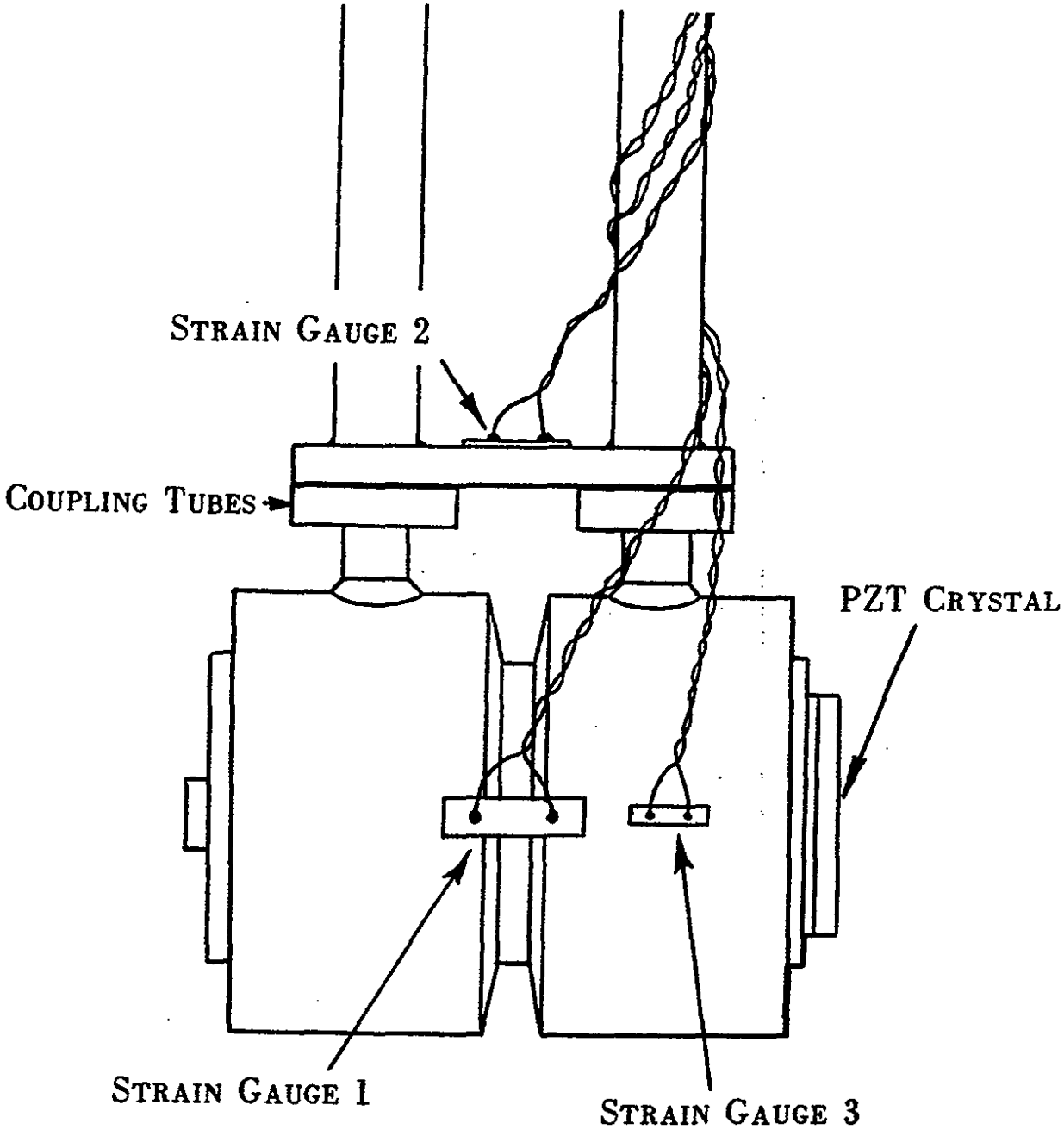

FIGURE 4.6 LOCATION OF STRAIN GAUGES AND PZT

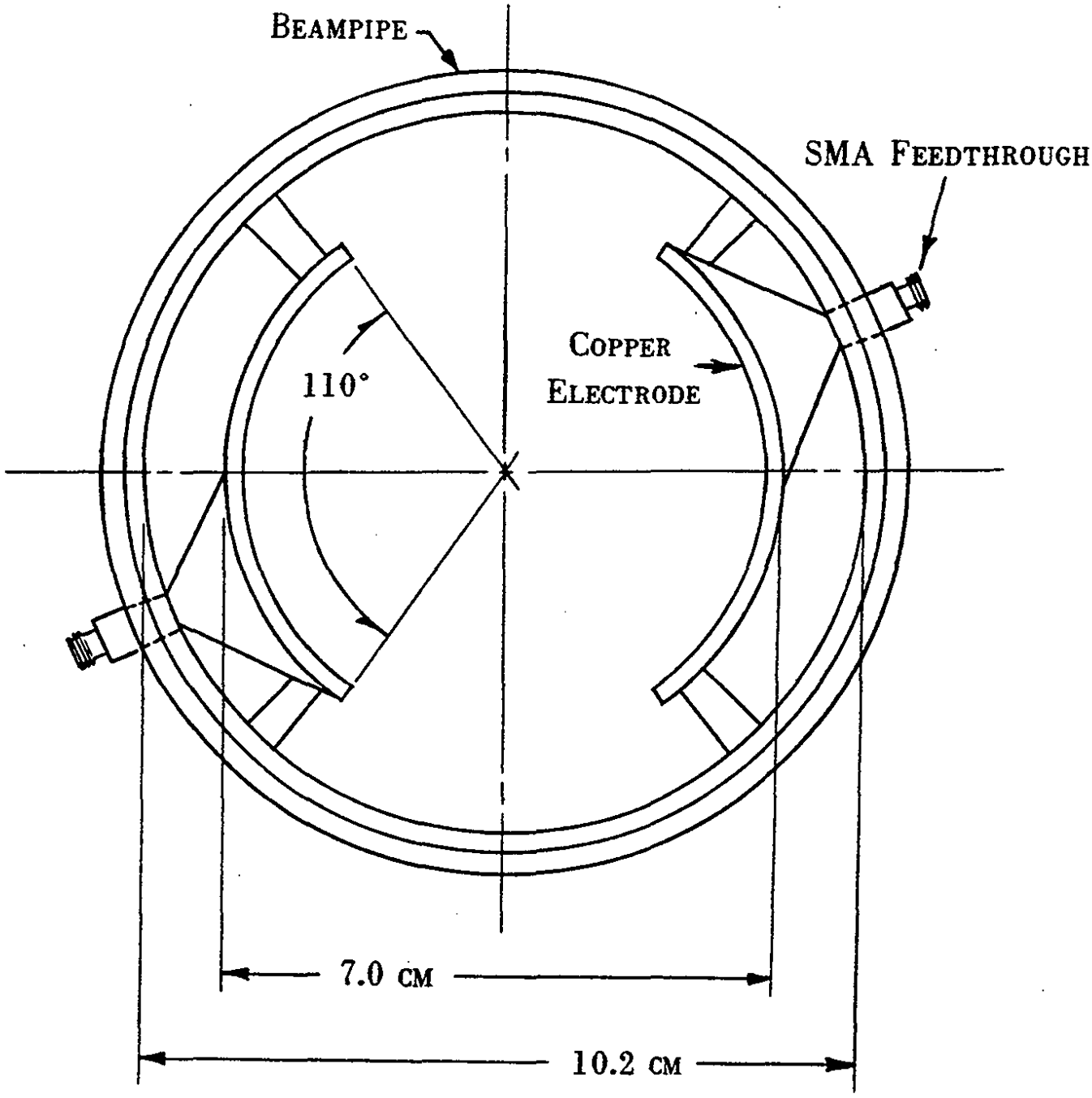

FIGURE 4.7 BEAM POSITION MONITOR

When a bucket travels between the pick-ups along the beam pipe axis, an electromagnetic signal is induced on the electrodes which is proportional to the intensity of the beam.[4] Typically, the output of the position monitor was 5±.5 Volts peak to peak for an intensity of $(8.5\pm.5)\times10^{12}$ protons in the Tevatron beam.

The output of the pick-ups are connected to two RG-8 foam cables which are phase balanced to ~1° at 53.11 MHz. The output of the pick-ups provided the necessary information concerning the harmonic content of the beam as well as the necessary phase information for the 26^{th} harmonic.

4.7 Detection Electronics

As previously described, the 180° phase difference between the two modes of the coupled cavities allowed us to detect the desired signal at the Δ-port of the hybrid tee. The first three stages of all of the detection schemes are the same as shown in figure 4.8.

The output of the Δ-port was monitored by a HP8555A Spectrum Analyzer to ensure proper balancing of the hybrid tee prior to amplification by the low noise amplifier. The signal was then amplified with a WJ-5310-532 GaAs FET Amplifier manufactured by Watkins Johnson Company. The amplifier had a gain of 42.1±.3 dB with a measured noise figure of 4.9 dB and an available output power of 20 mW.[5]

Once the signal was amplified, it was fed into a circulator

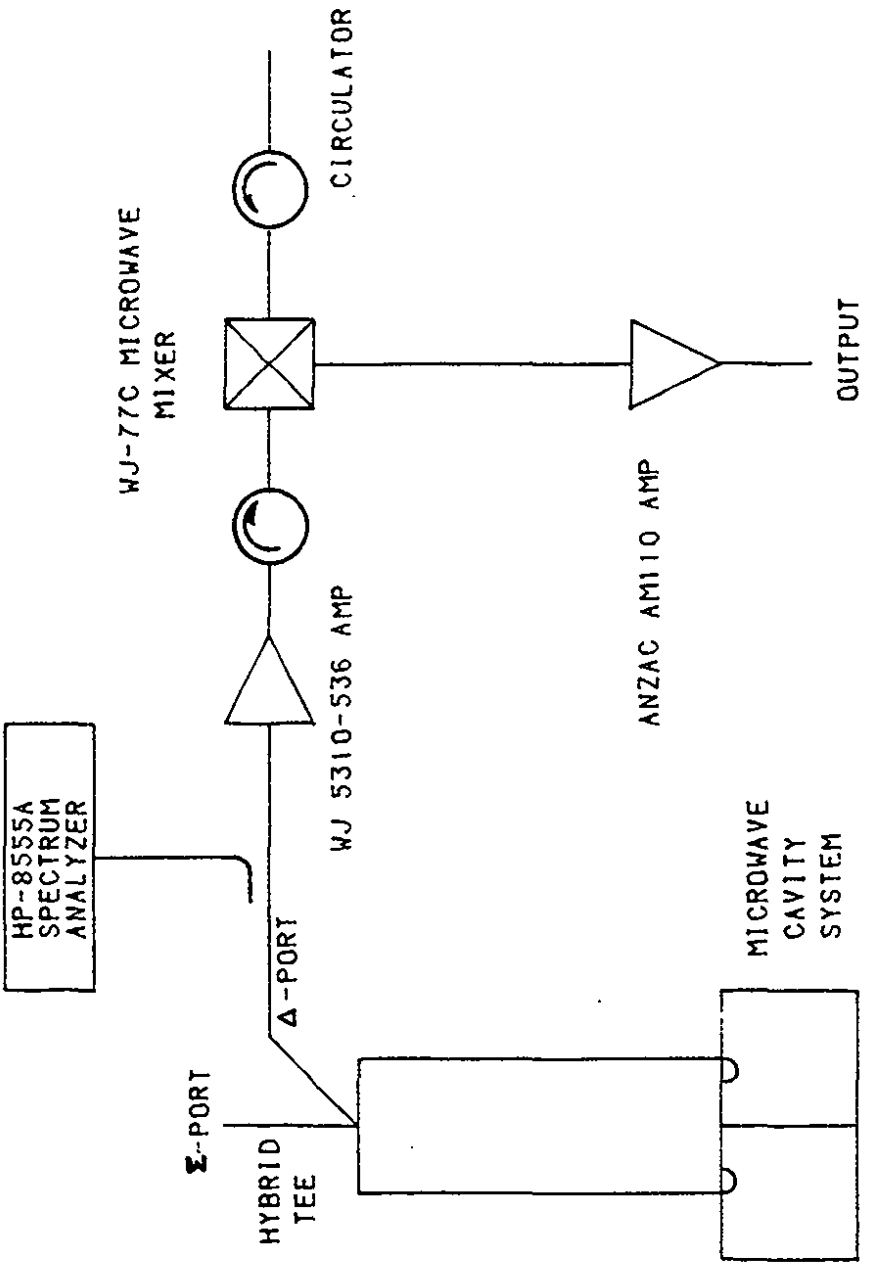

FIGURE 4.8 PRIMARY STAGES OF DETECTION SYSTEM

followed by a WJ-44C microwave mixer. The local oscillator port of the mixer was fed with +7 dBm at the input frequency to the cavities so that the IF port of the mixer was precisely at the intermodal difference frequency of the cavities. This signal was again amplified in a Model AM-110 low noise amplifier manufactured by Anzac Inc. It had a gain of 32 dB with a noise figure of ~6 dB in the frequency range of .5 to 500 MHz. For this experiment, the output was at the 26^{th} harmonic of the beam frequency namely, 1.240540 MHz ±30 Hz. Table 4.1 shows the gains and losses of the components used in this system.

The detection of the IF signal was accomplished by one of three different schemes using a one channel or a two channel Fast Fourier Transform Analyzer (FFT). In the first scheme, as shown in figure 4.9, the output of the Anzac amplifier was mixed with a 1.230 MHz signal from a HP3325A signal generator in a Model MD-140 Anzac IF Mixer. The IF output from this mixer was then precisely at a frequency of 10 kHz. The output signal was then mixed and amplified by 76.6 dB in a Model 5206 Lock-In Amplifier manufactured by Princeton Applied Research Corp.

The reference for the lock-in amplifier was provided by a second HP3325A Synthesizer which was phase locked to the first synthesizer and set to 10007.000±.001 Hz. The resulting output at 7.000 Hz was measured by a HP3561A FFT Spectrum Analyzer.

Table 4.2 shows the gains and losses of the IF detection elements used in this system. The overall noise figure for this system was 4.9±.1 dB resulting primarily from the WJ-5310-536

Table 4.1

Gain of Detection Electronics

Device	Gain dB	Output Signal Frequency	Noise Figure
Coaxial Transmission Lines	-2.0	9.94438 GHz	********
Microwave Waveguide Lines	-4.6	9.94438 GHz	********
WJ5310 GaAs FET Amplifier	+42.1	9.94438 GHz	4.9 dB
WJ77C Microwave Mixer	-5.5	1.24054093 MHz	5.5 dB
AM-110 Anzac IF Amplifier	+32.1	1.24054093 MHz	6.0 dB
Total Gain	62.1±.5 dB		
Total Noise Figure	4.9±.1 dB		

Table 4.2

Gain of Single and Two Mixer Detection Schemes

Device	Gain dB	Output Signal Frequency
Gain of Initial Stages	62.0	1.24054093 MHz
MD-140 Anzac IF Mixer	-4.7	10.0000 kHz*
PAR5206 Lock-In Amplifier	+76.6	7.000 Hz
HP3561A FFT	*****	7.000 Hz
Total Gain	133.9±.5 dB	
Total Noise Figure	4.9±.5 dB	

* For the two mixer beam reference scheme this frequency was 75 kHz.

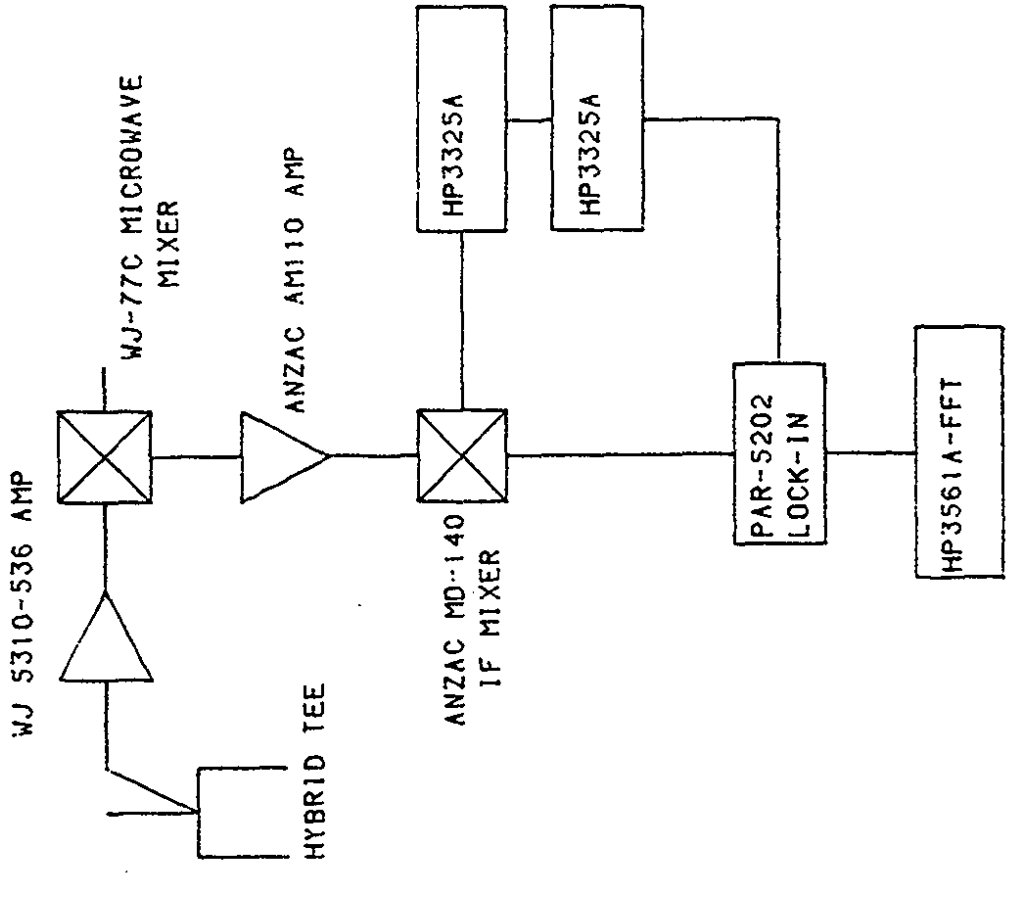

FIGURE 4.9 SINGLE MIXER MODE DETECTION SYSTEM

Amplifier. The overall gain for the system was 133.9±.5 dB.

In the 2-mixer version of this detection scheme shown in figure 4.10, the reference for the lock-in amplifier was provided by making use of a beam synchronous reference signal. The beam in the Tevatron is phased locked to one part in 10^8 to this signal at the fundamental beam RF frequency of 53.109 MHz. It therefore provided an extremely precise reference signal with which to compare any upconverted signal present in our cavities.

The beam sync signal was multiplied in frequency to the 26^{th} harmonic at 1.240 MHz in a phase lock loop amplifier. The output of the phase lock loop was then mixed with a reference signal from the second HP3325A. In this case, the 1^{st} and 2^{nd} synthesizers were set at 1.165541 MHz and 1.165548 MHz (±.001 Hz) respectively. The output of this second mixer was thus at 75 kHz and was filtered in a simple LRC filter network and then applied to the reference port of the lock-in amplifier. The noise figure and overall gain for this system was the same as the one mixer mode. This system had a measured frequency stability between the beam synchronous reference signal and the beam position monitor better than 50 mHz.

The final detection scheme is shown in figure 4.11. In this case, the second stage mixers labelled A and B were driven by the same HP3325A synthesizer at a frequenncy of 1.239522 MHz (±.001 Hz). The output containing the signal of interest at 1019.00±.03 Hz was then amplified with a Model TM503 Tektronics amplifier and finally fed into channel A of a HP3582A Dual Channel FFT Analyzer. The reference channel for the analyzer was provided by the output of

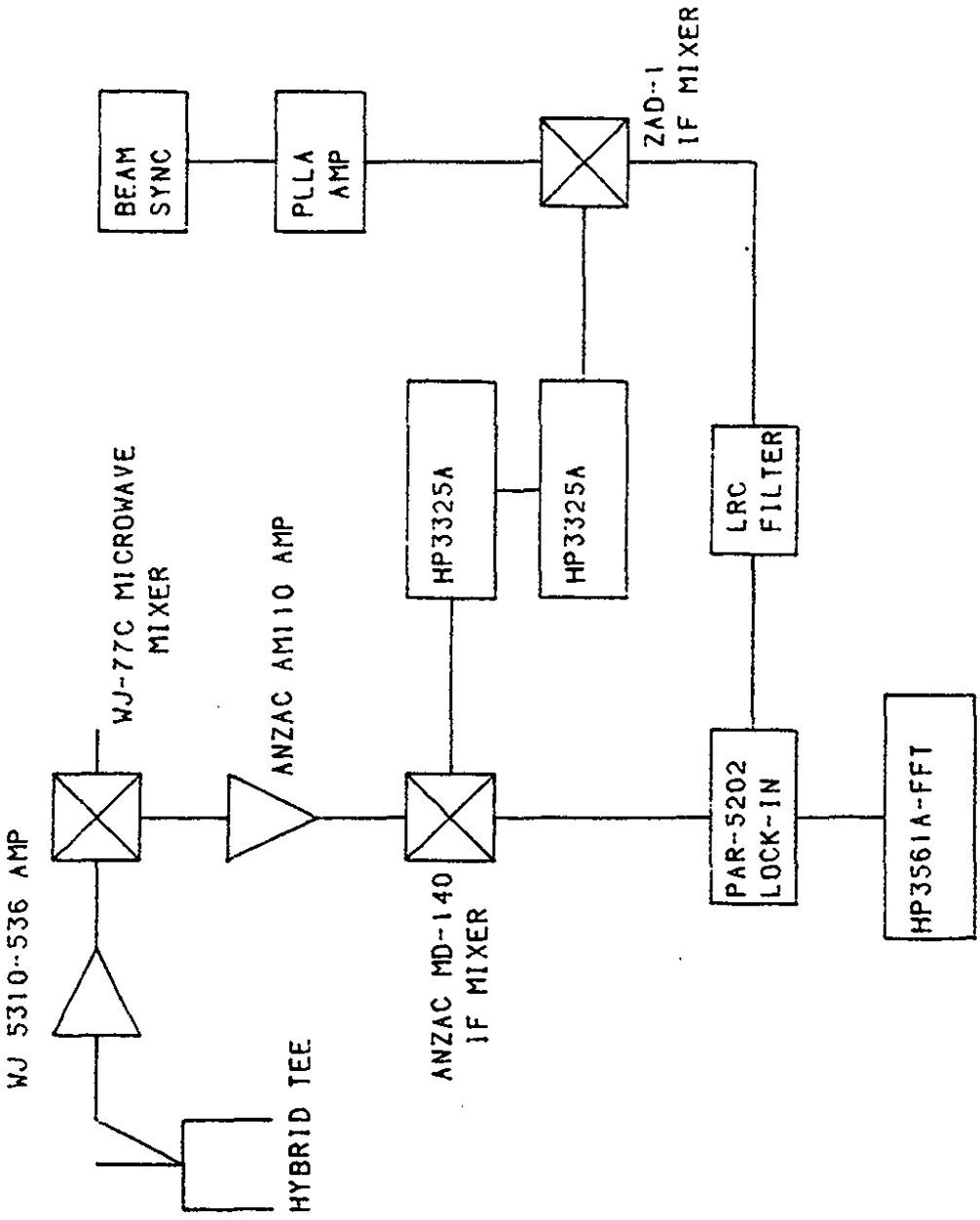

FIGURE 4.10 TWO MIXER MODE DETECTION SYSTEM

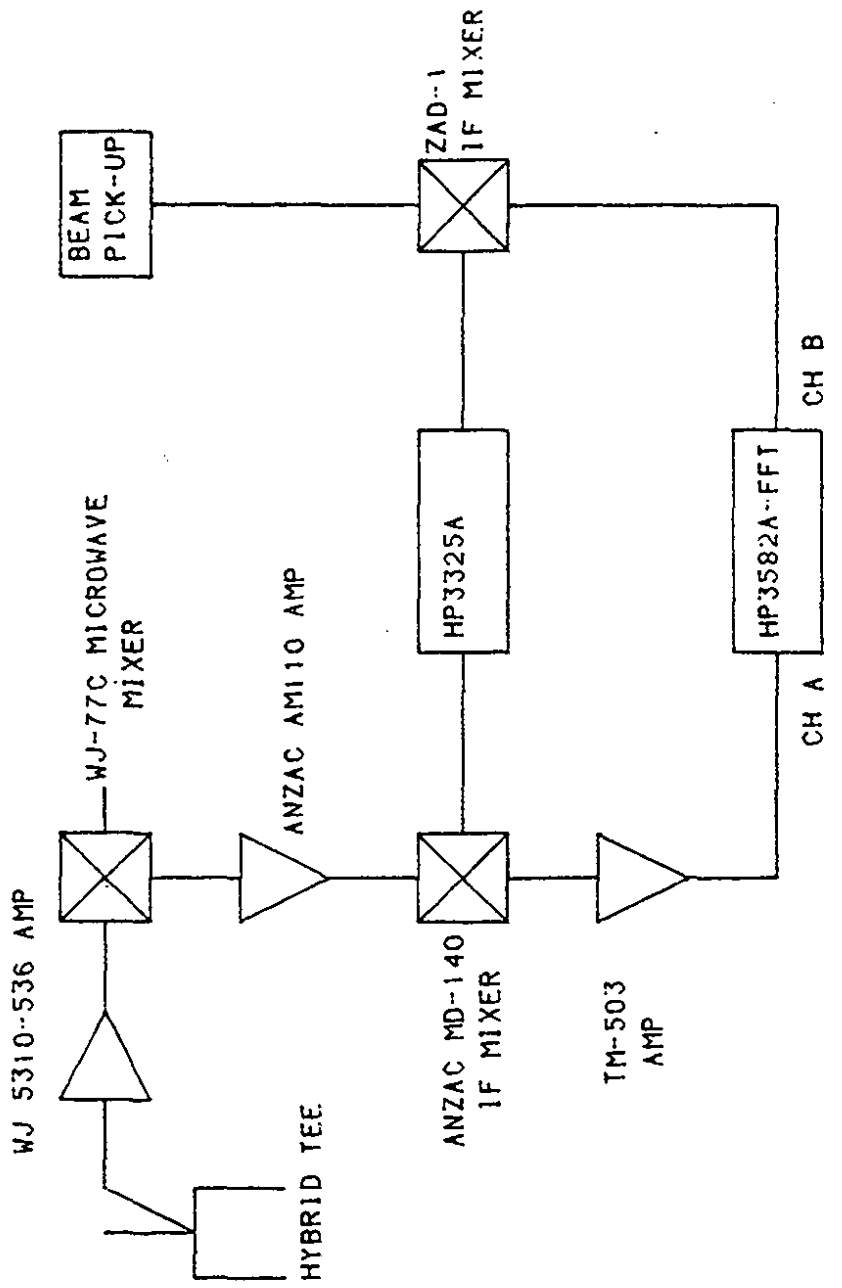

FIGURE 4.11 DUAL CHANNEL FFT DETECTION SYSTEM

Table 4.3

Gain of Dual Channel FFT Detection Scheme

Device	Gain dB	Output Signal Frequency
Gain of Initial Stages	62.0	1.24054093 MHz
MD-140 Anzac IF Mixer	-4.7	1019.0 Hz
TM503 TEK Amplifier	+23.1[1]	1019.0 Hz
HP3582A FFT	*****	1019.0 Hz
Total Gain	80.4 dB[1] (±.5 dB)	Total Noise Figure 4.9 dB (±.1 dB)

[1] These values reported for the 4.2° K data run. For the 1.89°K data run the gain of the TEK amplifier changed to +17.1 dB for an overall gain of 74.4 dB.

mixer B as shown. In this way, the exact phase relationship between the upconverted signals and the beam pick-ups could be measured for each given beam cycle and hence the techniques described in section 3.3 could be utilized.

Table 4.3 shows the gains and losses for this detection system. The overall noise figure remained essentially the same, but the gain was 80.4±.5 dB for data taken at 4.2° and 74.4±.5 dB for the data taken at 1.89° K.

4.8 Data Acquisition

The data acquisition system was based on a Digital PDP-11/34 Computer manufactured by Digital Equipment Corporation with a DEC Magtape TU16 9 channel tape drive, a Model IV Bison Control Interupt Box, and two RL01K disk drive units. Other peripherals included a DEC-10 Decwriter teletype, a LSI Model ADM-3A Video Display Terminal and a Versetec Matrix Printer. A block diagram of the system is shown in figure 4.12.

The interface between the computer and our detection system was based on the Camac System. A Model 70A type A1 Crate Controller was conected to a Jorway Model 411 PDP11/Camac Interface. The Jorway Crate Controller was used to address a Kinetic Systems Model 3388 GPIB Interface which in turn addressed the FFT.

The system software was the RT-11 system monitor for PDP

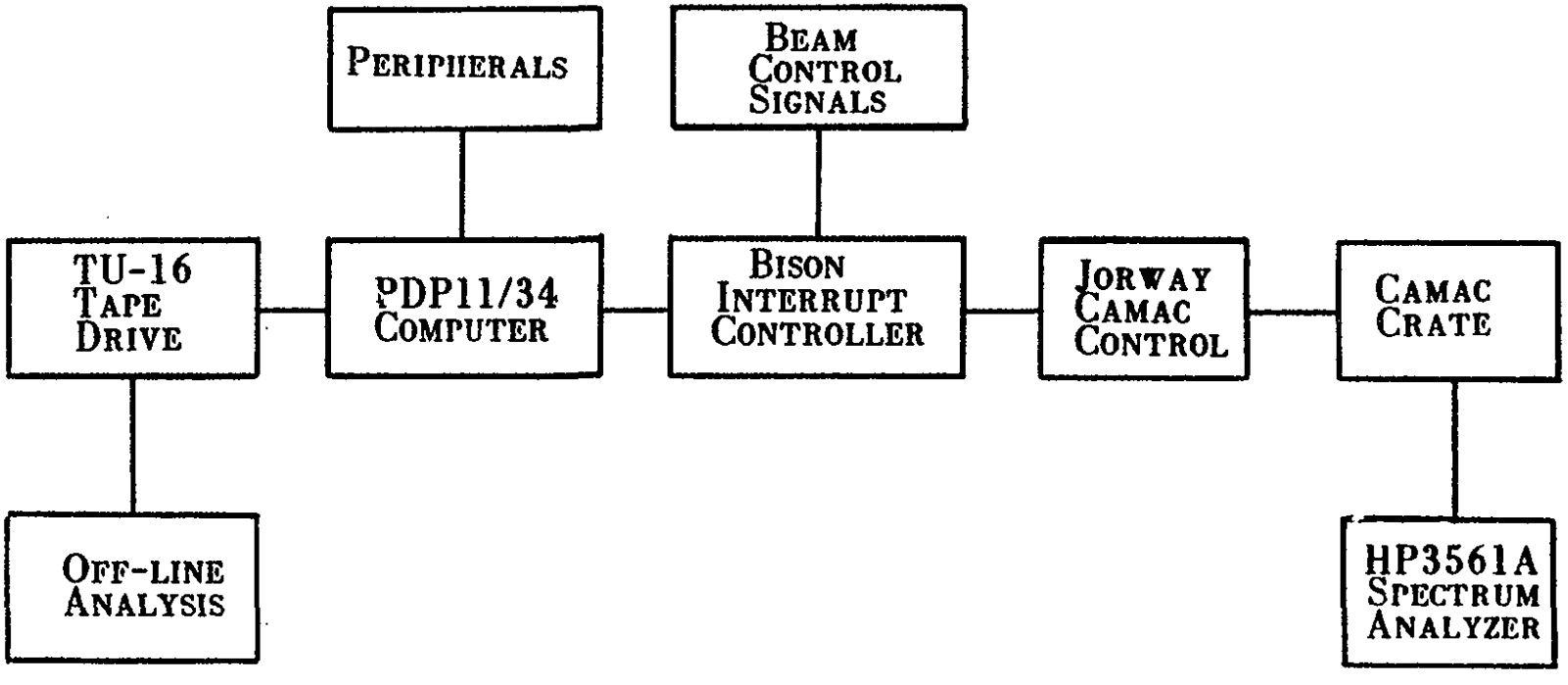

FIGURE 4.12 BLOCK DIAGRAM OF DATA ACQUISITION SYSTEM

computer systems and the actual data logging software was a version of the MULTI Data Acquisition System with slight modifications to allow for computer control of the HP Models 3561A and 3582A Fast Fourier Transform Analyzers.

We were primarily interested in logging data during normal HEP operation of the Tevatron. This was accomplished by making use of the various trigger signals provided by the main control room via a Camac Controls Model 178 Card located in a second Camac Crate near our detection system. These trigger signals were used to initiate the acquisition and storage of the data on S-type 9 track high density magtape.

During a typical beam cycle, the computer would initialize the FFT to its proper settings and wait for the first trigger signal to arrive. Upon receiving this signal through the Bison Interupt Controller, it would then trigger the FFT to begin taking data. A second interrupt signal would then allow the computer to read the data from the FFT and write it on the magtape in 16-bit words and the cycle would be repeated.

Off-line analysis of the data tapes was performed on the Fermilab NOS-2 Cyber Computing Facility. We used a modified version of the MULANA software program developed at Fermilab to analyze data logged with the RT-11 MULTI Data Acquisition System.[6] Further processing of the data was then performed using the facilities of the Cyber Network. Appendix C describes the algorithm used to analyze the data tapes.

References

1. P.J. Reiner, Report No. UR-807, Department of Physics and Astronomy, University of Rochester, Rochester, N.Y. (1983) (unpublished).

2. C.E. Reece, Report No. UR-867, Department of Physics and Astronomy, University of Rochester, Rochester, N.Y. (1983) (PhD. Thesis, unpublished).

3. C.E. Reece, Ibid. p62-64.

4. R.E. Shafer, R.C. Webber, and T.H. Nicol, IEEE Transactions on Nuclear Science, NS-28, No. 3, (1981) 2290-2.

5. J.T. Rogers, Report No. UR-873, Department of Physics and Astronomy, University of Rochester, Rochester, N.Y. (1983) (unpublished).

6. A. Kreymer, R. Pordes, D. Ritchie, FNAL Application Note "Mulana," PM0041.2 (unpublished).

Chapter 5

Results

5.1 Introduction

The results reported here are divided into two groups, the first of which consists of measurements which characterize the detector properties while the second set consists of the actual beam induced data that was obtained. The electrical characteristics of the detector are included in section 5.2 along with measurements of the linearity of the upconversion process with different mechanical excitations. Section 5.3 presents data which characterize the mechanical structure of the detector and measurements of the mechanical Q_m for various resonances of the cavity system. Finally, section 5.4 presents the beam induced data and is divided into 3 subsections. The first subsection includes data taken with a single channel FFT (one mixer mode) without the inclusion of phase information from the beam intensity monitor. The next subsection presents data obtained with the two mixer mode in which the frequency of the beam is precisely tracked during the measurements. Finally, section 5.4.3 describes the data obtained with the Dual Channel HP3582A FFT and represents the best data taken to date.

5.2 Electrical Characteristics

All of the detection schemes rely upon the upconversion process as given in equation 3.3 restated here for convenience.

$$\Delta l = 27.3 \left(\frac{\Delta f_N}{\Delta f_{min}} \right) \left[\frac{P_2}{P_1} \frac{1}{Q_1 Q_2} \frac{(\beta_1+1)(\beta_2+1)}{\beta_1 \beta_2} \left\{ \frac{f_2}{f_1} \right\} (1+4Q_2^2 \Delta^2) \right]^{\frac{1}{2}} \qquad (5.1)$$

The electrical Q_e for each mode of the cavity system was measured by locking onto the desired resonance and observing the decay time of the radiated power as the microwaves were switched off with the high speed PIN switch. The Q values were then measured as a function of probe position as shown in figure 5.1. The unloaded Q values along with the coupling factors β_1 and β_2 could then be determined as a function of probe position

The unloaded Q was also measured as a function of temperature and is shown in figure 5.2. The solid curve in this figure represents the theoretical maximum derived from the BCS theory of superconductivity and the dashed curve represents the measured values. The data indicated by dots was obtained in Rochester in 1983 immediately after the cavity was annealed in an ultra-high vacuum furnace at Brookhaven National Laboratory. The data indicated by triangles was obtained during this investigation. This graph shows that the unloaded Q has degraded somewhat over the two year period. The large discrepancy between the predicted values and the real data at low temperatures can be attributed to resistive

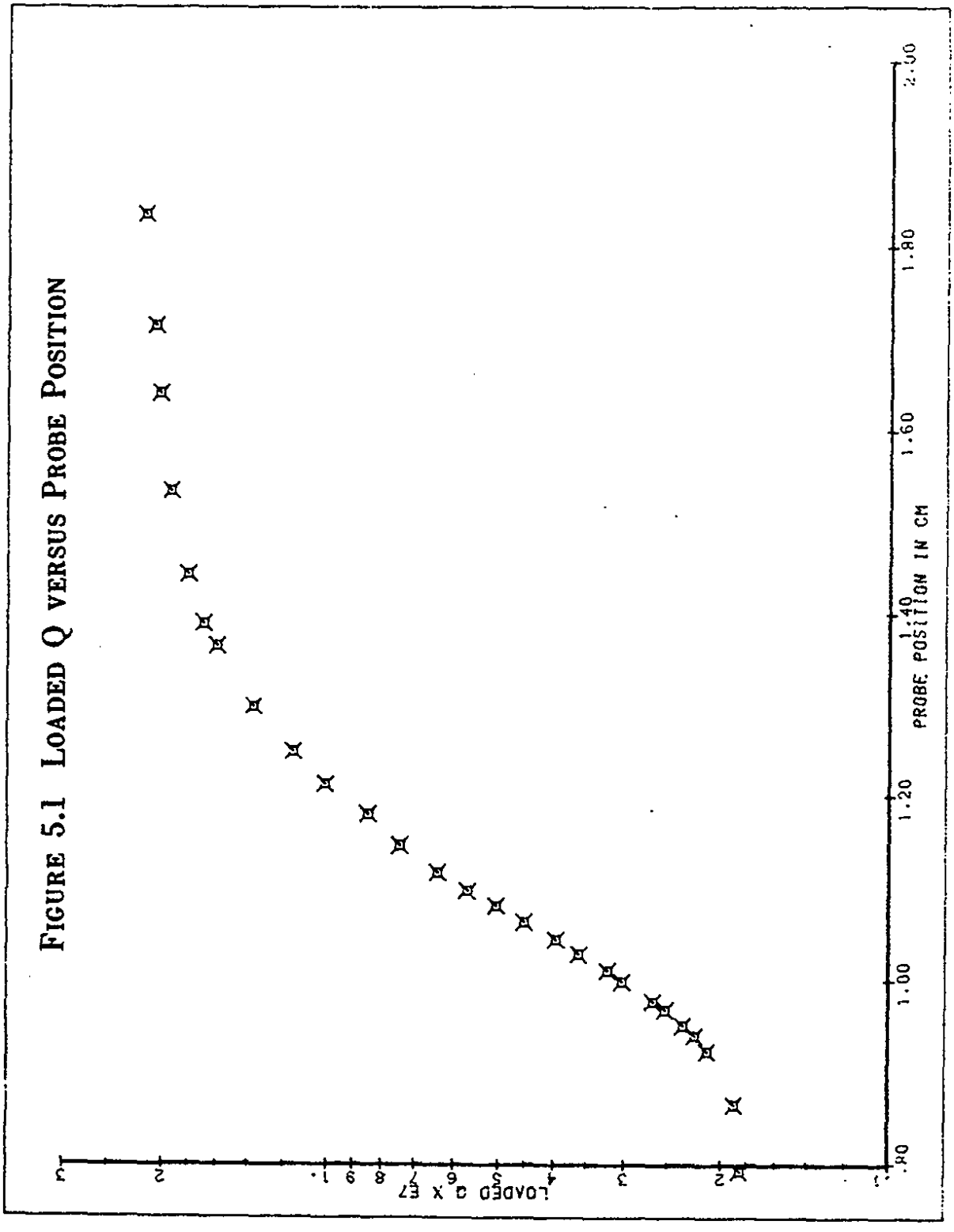

FIGURE 5.1 LOADED Q VERSUS PROBE POSITION

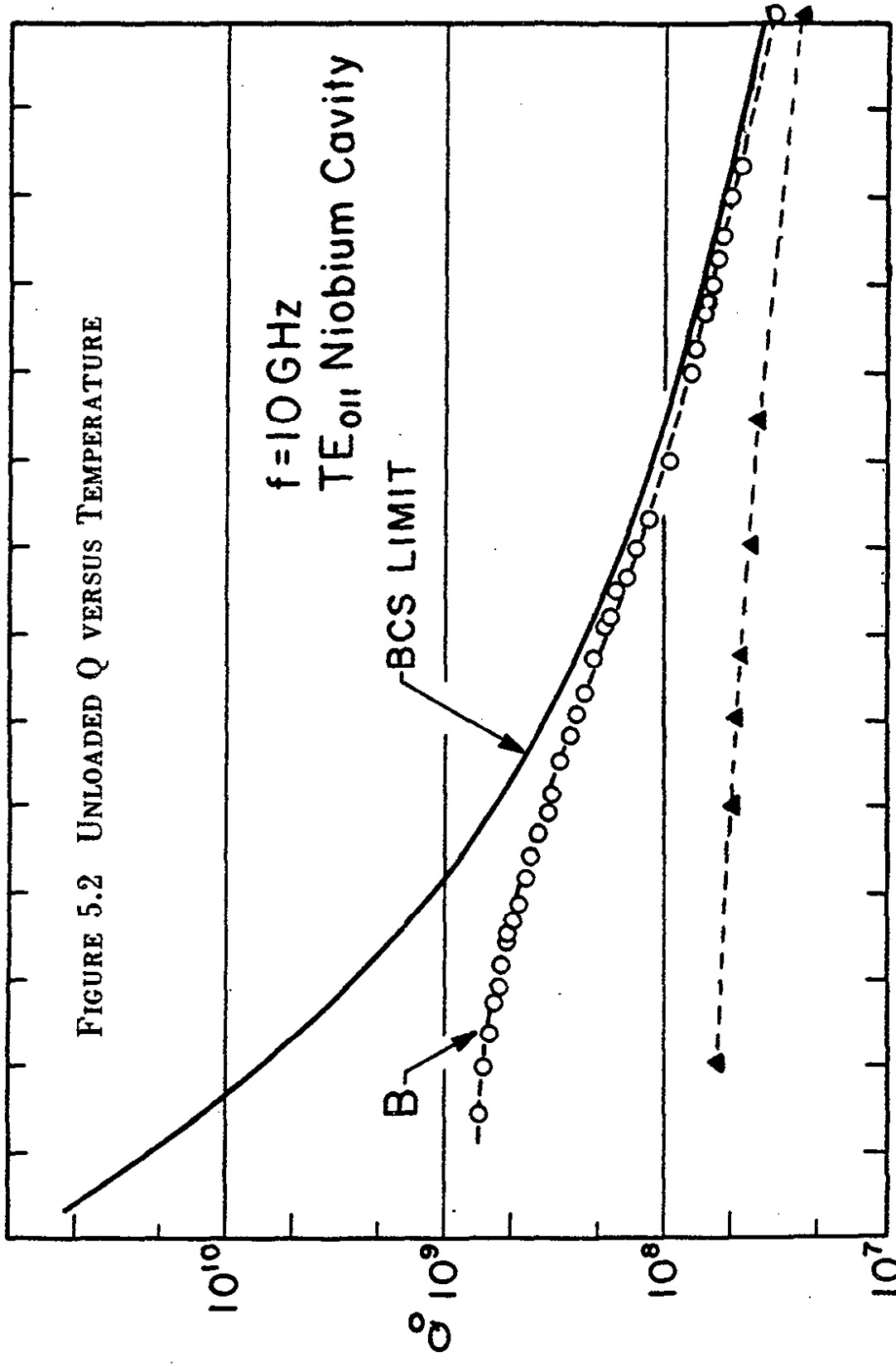

FIGURE 5.2 UNLOADED Q VERSUS TEMPERATURE

losses in the cavity due to surface contamination of the Niobium.

Critical coupling of the cavities occurs when the loaded Q is exactly half of the unloaded Q so that $\beta_1=\beta_2=1$. Since upconversion data was taken at two separate temperatures 4.2°K and 1.89°K, the probe positions were first set for critical coupling at 4.2° K and then were reset for 1.89° K operation by mechanically moving the probes while monitoring the decay time of the power stored in the cavities. Hence, for operation at 4.20°K $Q_1=(1.24\pm.02)\times10^7$ and $Q_2=(1.29\pm.02)\times10^7$ and at 1.89°K $Q_1=3.0\times10^7$ and $Q_2=3.1\times10^7$. For both temperatures $\beta_1=\beta_2=1.0$.

The difference frequency Δf of the cavities was measured by locking onto the input microwave frequency and observing the peak due to the phase noise of the oscillator which excites the second mode. Figure 5.3 shows a typical trace of the microwave power in the region of the second resonance obtained by measuring the output stage of the first IF mixer with the HP3561A FFT. The output of this mixer provides a precise measure of the difference frequency by comparing it to the frequency of the input power to the cavities. For all data sets, the difference frequency was set to the 26^{th} harmonic of the beam revolution frequency at 1.24054093 MHz ±.025 Hz. Adjustments to Δf were made by using the remotely controlled endwall tuning mechanism. The minimum difference frequency of the cavity system was also measured and found to be 1.18 MHz. Since the difference frequency was always maintained at the expected excitation frequency of the cavities, the last term in equation 5.1 was unity ($\Delta=0$).

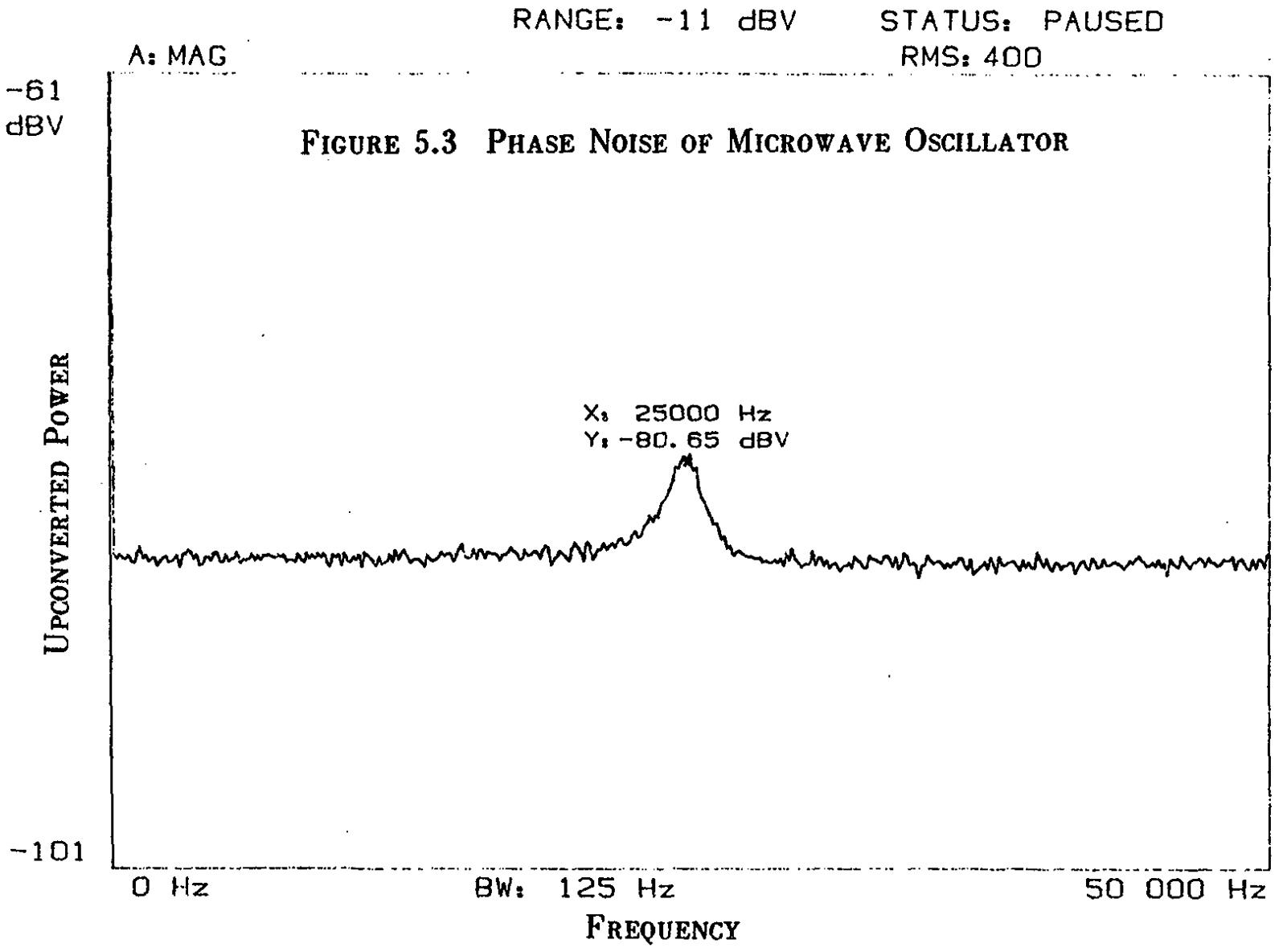

FIGURE 5.3 PHASE NOISE OF MICROWAVE OSCILLATOR

The input power to the cavities was measured at 5.58±.05 mW. The signal at the delta port of the hybrid tee at the input frequency to the cavities was maintained below -50 dBm by carefully adjusting the phase shifters on the microwave feed lines to maintain proper phase and amplitude balancing of the hybrid tee. The microwave system was locked onto the antisymmetric mode of the cavity system and adjustments were made to the DC tuning level of the phase lock loop circuitry as needed to maintain locking to the cavity mode.

A check of the linearity of the output power P_2 of the detector with the effective strain $(\Delta l)^2$ was made by applying known voltages at 1.240 MHz to each of the strain gauges and the PZT and monitoring the upconverted signal level. The apparatus used is shown in figure 5.4. This detection scheme is similar in operation to the one shown in figure 4.9 except that the second HP3325A synthesizer is used to excite the desired strain gauge or the PZT mounted on the resonant endwall of the cavity.

The results shown in figure 5.5 depict the linearity of the upconversion process for each of the transducers. From this graph we can readily see that the detector appears to be most sensitive to excitations produced by strain gauge 1 and least sensitive to strain gauge 2.

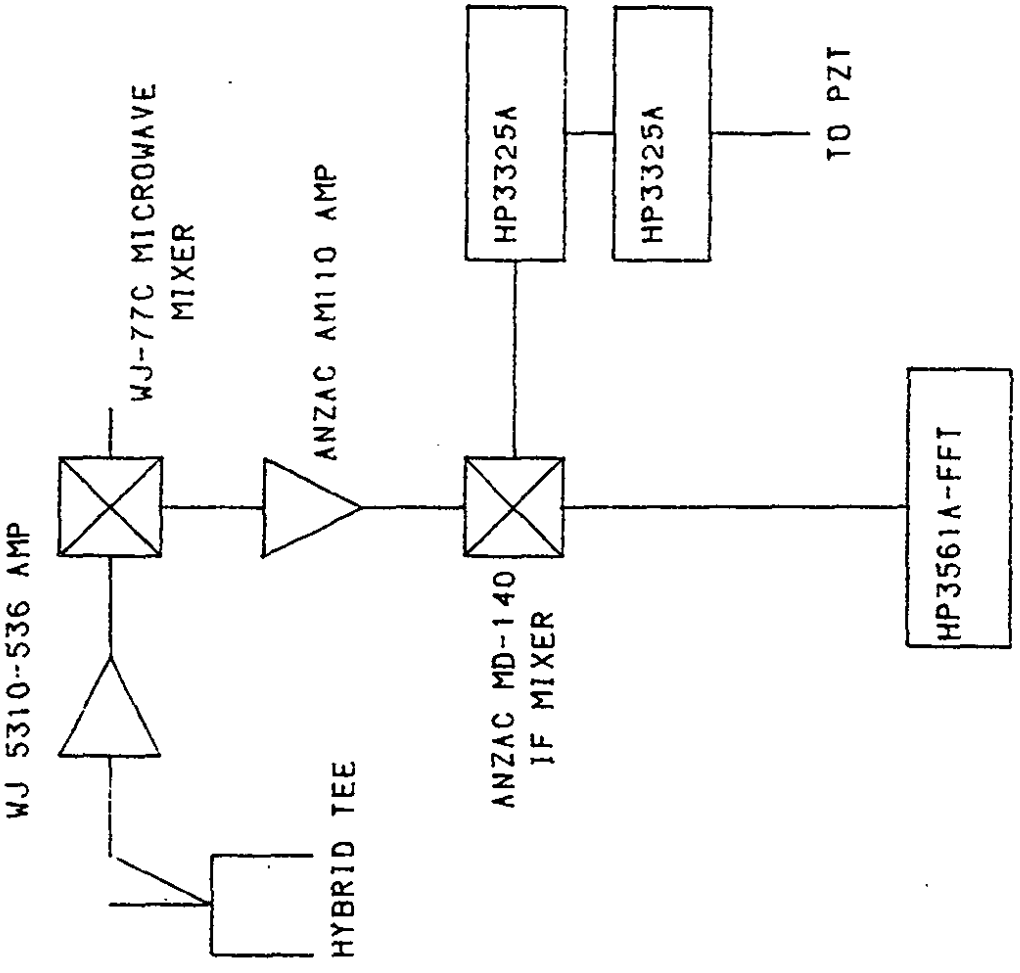

FIGURE 5.4 PZT CALIBRATION SYSTEM

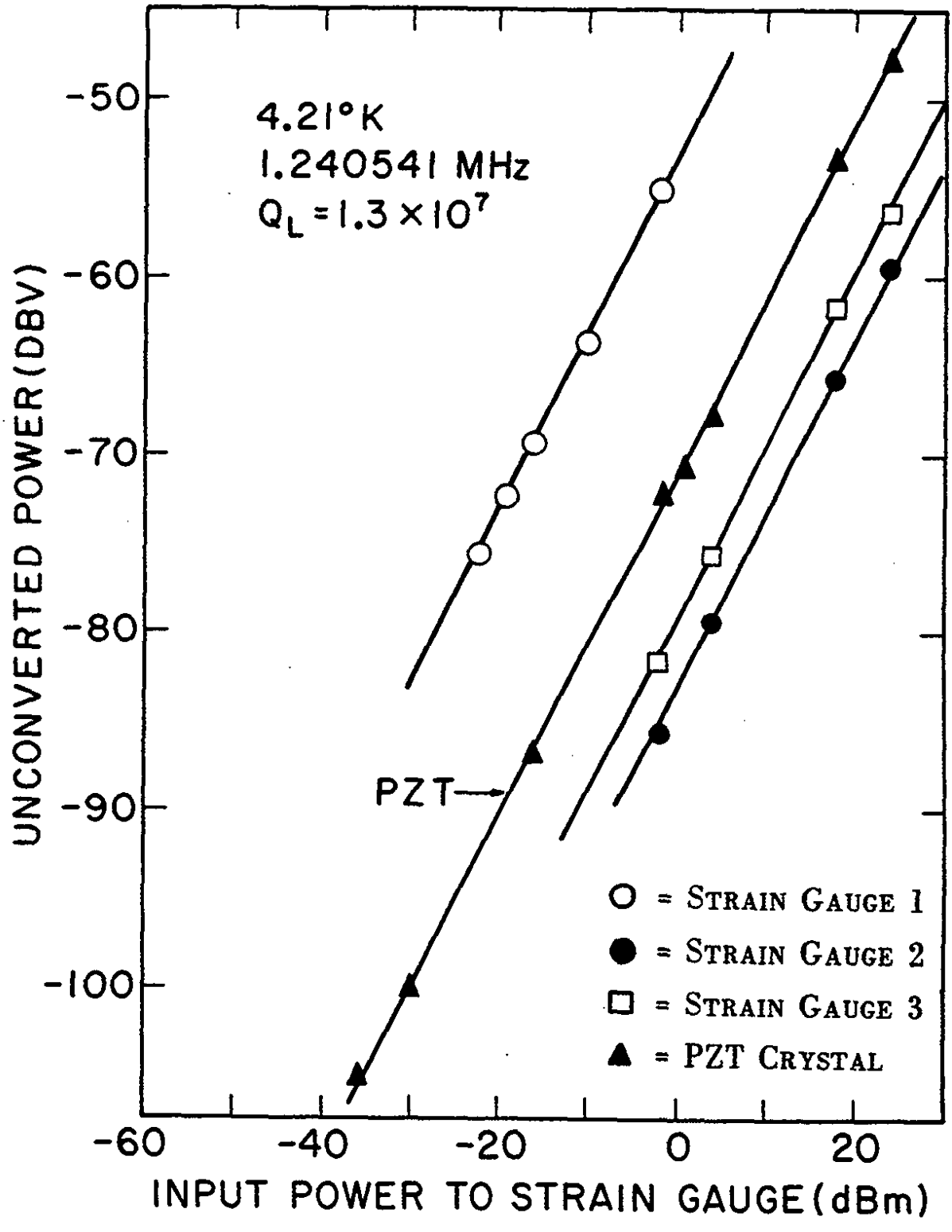

FIGURE 5.5 UPCONVERTED POWER VERSUS PZT EXCITATION

5.3 Mechanical Characteristics

The physical structure of the detector is complex involving several different shapes and sizes of a variety of materials such as Niobium, stainless steel and Aluminum. This gives rise to an extremely complex set of mechanical resonances which are difficult, if not impossible, to resolve in terms of specific modes of vibration. When the excited mechanical resonances fall within the bandwidth of the electrical difference frequency (Δf) of the detector, they excite the second cavity resonance and hence produce upconverted power at the symmetric mode. This effect can be measured with the apparatus shown in figure 5.4 where the frequency of the synthesizer driving the strain gauge is swept around the center frequency at 1.240 MHz. The result of the PZT excitation (at fixed voltage) is shown in figure 5.6 with upconverted power versus excitation frequency. This data was obtained with a PZT voltage of 10.0±.1 volts peak to peak. The envelope of this graph is determined by the electrical Q of the cavities so that the largest upconverted power of the detector occurs near the center of the electrical resonance.

Figure 5.7 shows a similar measurement with several different voltages applied to the PZT. The frequency sweep in this case is narrower than in figure 5.4. The bottom trace in this figure shows the exact location of the cavity difference frequency. This figure shows the reproducibility of the detailed mechanical structure of the detector. The measurement of this structure is possible because

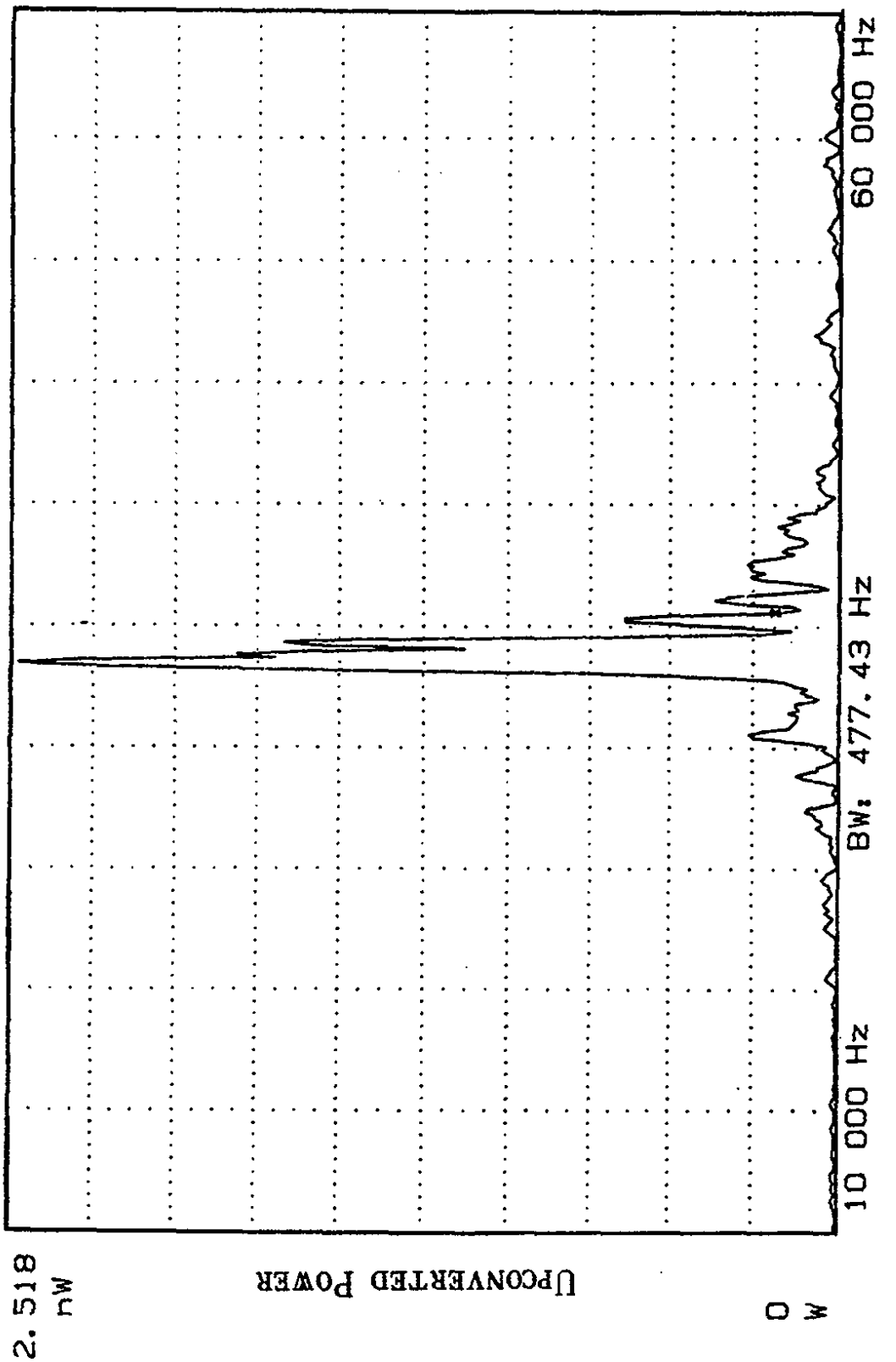

FIGURE 5.6 UPCONVERTED POWER VERSUS FREQUENCY

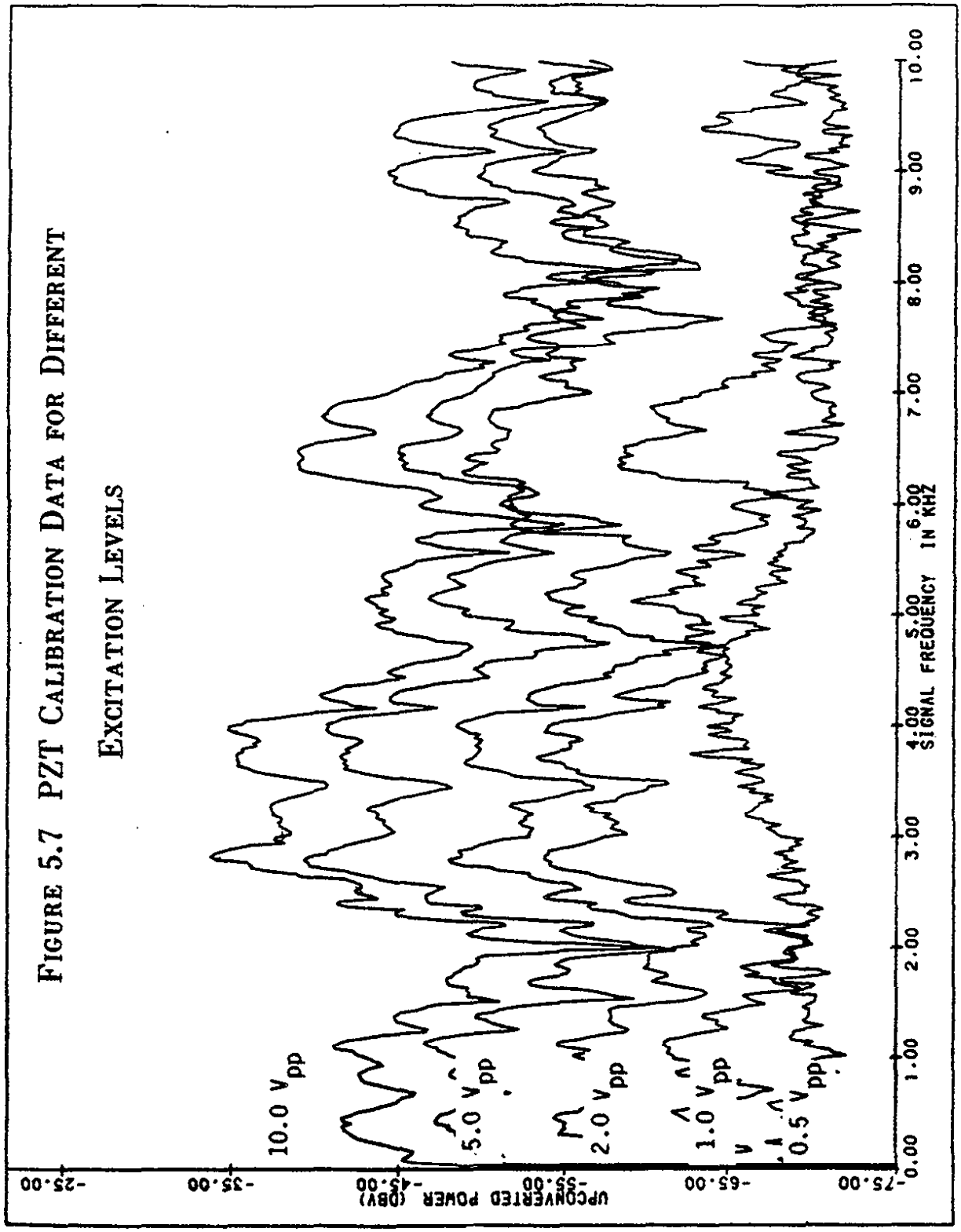

FIGURE 5.7 PZT CALIBRATION DATA FOR DIFFERENT EXCITATION LEVELS

the stability of the difference frequency of the microwave system is less than 1 Hz out of 1.24 MHz even though the cavity resonances are ~1 kHz wide.

The fact that the upconverted power decreases uniformly with decreasing excitation levels of the PZT (or of the strain gauges) for several different frequencies indicates the linearity of the upconversion process for several different modes of vibration.

The response of the detector to a mechanical excitation was derived in equation 3.6.

$$\frac{F_g(\omega)}{m} = \Delta l \left[(\omega_0^2 - \omega_p^2)^2 + \left\{ \frac{\omega_p \omega_0}{Q_m} \right\}^2 \right]^{\frac{1}{2}} \qquad (5.2)$$

In this expression we assume that the mechanical system is a bar oscillating in its longitudinal mode. Due to the complexity of the mechanical couplings in the detector it is not possible to verify this equation in detail. However, an estimate of the effective mechanical Q_m can be made for the resonance of interest at 1.240541 MHz. We define the mechanical Q as usual as the width of the resonant energy peak at half the absorbed power level divided by the resonant frequency.

$$Q_m = \frac{\Delta\omega}{\omega_0} \qquad (5.3)$$

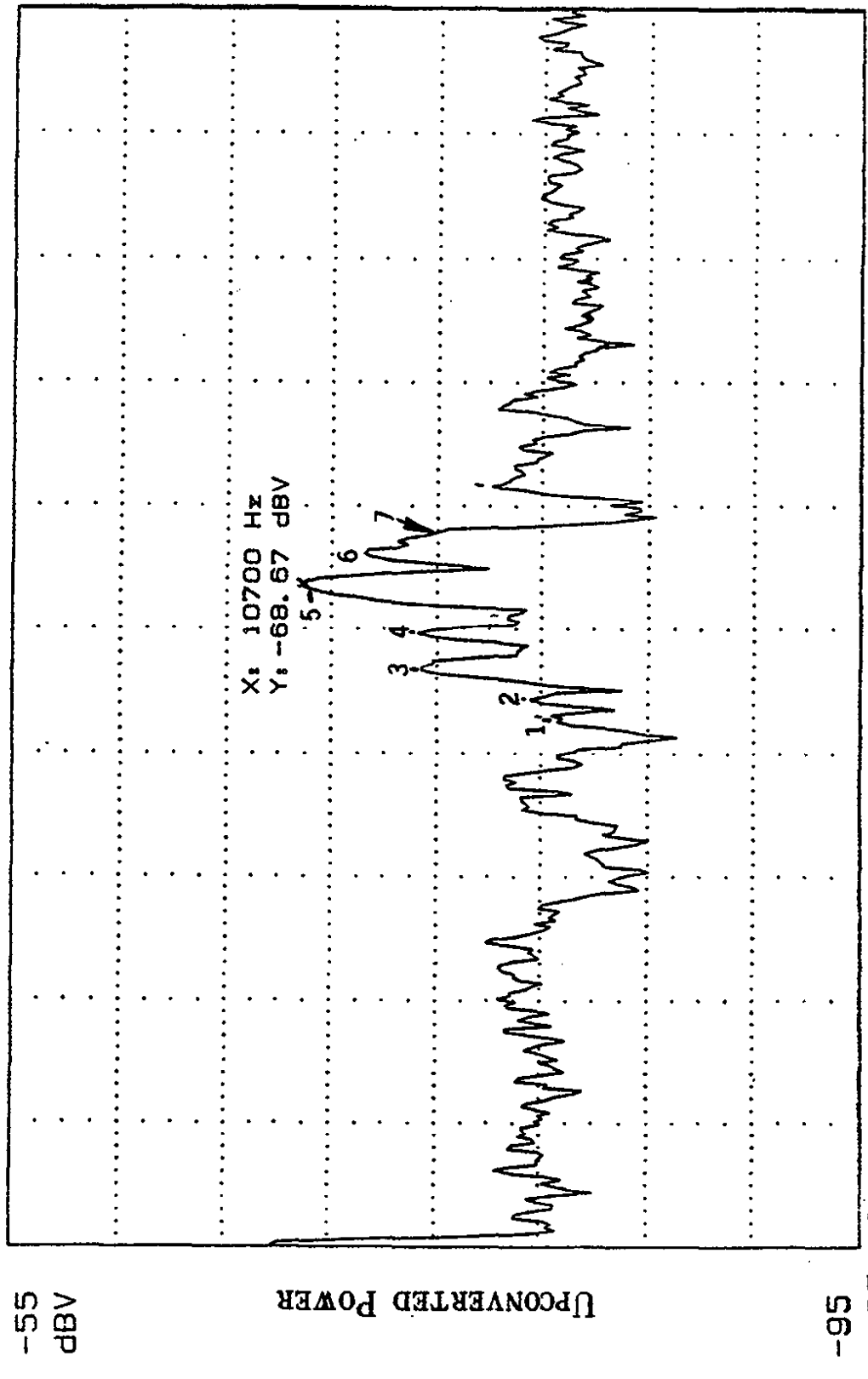

FIGURE 5.8 MECHANICAL RESPONSE OF DETECTOR TO PZT EXCITATIONS

Table 5.1

Mechanical Q Measurements

Peak No.	Bandwidth (Hz)	Frequency (MHz)	Q_m
1	300	1.238600	4130
2	250	1.238900	4960
3	380	1.239400	3260
4	250	1.239900	4960
5	300	1.240700	4140
6	300	1.241250	4140
7	420	1.241400	2960

NOTE: The frequency measurements and the bandwidth measurements are all ±100 Hz due to the fact that the bandwidth was 190 Hz for each measurement.

A few selected peaks are shown in figure 5.8 and the corresponding estimate of the mechanical Q_m is given in table 5.1. These estimates reflect the smallest allowed value for the mechanical Q and are limited by the 190 Hz bandwidth of the electronic system used to measure the peaks. It is important to note that the peaks measured may in fact be a superposition of several different resonances which add together to produce the observed excitation. However, measurement of these peaks resulted from the endwall being driven primarily in a longitudinal mode at the measured frequency. Hence we can say that if a gravitational impulse also drives the endwall in the same way as the PZT, then it will produce the same structure in the upconverted power as a function of frequency.

5.4 Upconversion Data

5.4.1 Single Mixer Mode

The data reported in this section was obtained using the single mixer mode detection scheme described in section 4.7. The reference frequencies of the mixer and the lock-in amplifier were selected so that the desired signal was maintained precisely at 7.000±.025 Hz during each measurement. The temperature was maintained at 4.20°K and two successive averages were taken for every beam cycle. The

HP3561A was set to take a single 16 second spectral average starting at the beginning of flattop and then a second 16 second average starting at the end of the flattop for each beam cycle. The resulting bandwidth of the detection system was 62.5 mHz.

In order to calibrate this system, one of the outputs of the beam intensity monitor was filtered and amplified to give a strong signal at the 26^{th} harmonic of the beam revolution frequency and applied to the PZT. Figure 5.9 shows the resulting calibration peak with -15.0±.5 dBm applied from the beam pick-ups at 1.24054093 MHz ±.025 Hz. This calibration peak shows that the desired signal has a width which is less than 62.5 mHz and therefore resides in a single FFT frequency bin at precisely 7.000±.025 Hz (see section 4.7). The dashed line shows the calibration when the beam intensity was zero and gives a measure of the noise background during this run.

The actual upconverted data for this system is shown in figure 5.10 on an expanded frequency scale centered about the bin of interest at 7.000±.025 Hz. This data represents the average of two seperate runs with 301 averages in the first set and 194 averages in the second set. It should also be noted that the first data set spanned the frequency range of 0.0 to 25 Hz and the second frequency span was adjusted so that the desired signal was in the center frequency bin. The 495 averages were obtained by shifting the two data sets so that the signal of interest was in the same frequency bin. The data was taken with 12 booster batches in the ring at an energy of 800 GeV per proton. The average intensity of the beam was $(6.62\pm.05)\times10^{12}$ protons (with a corresponding average 26^{th} harmonic

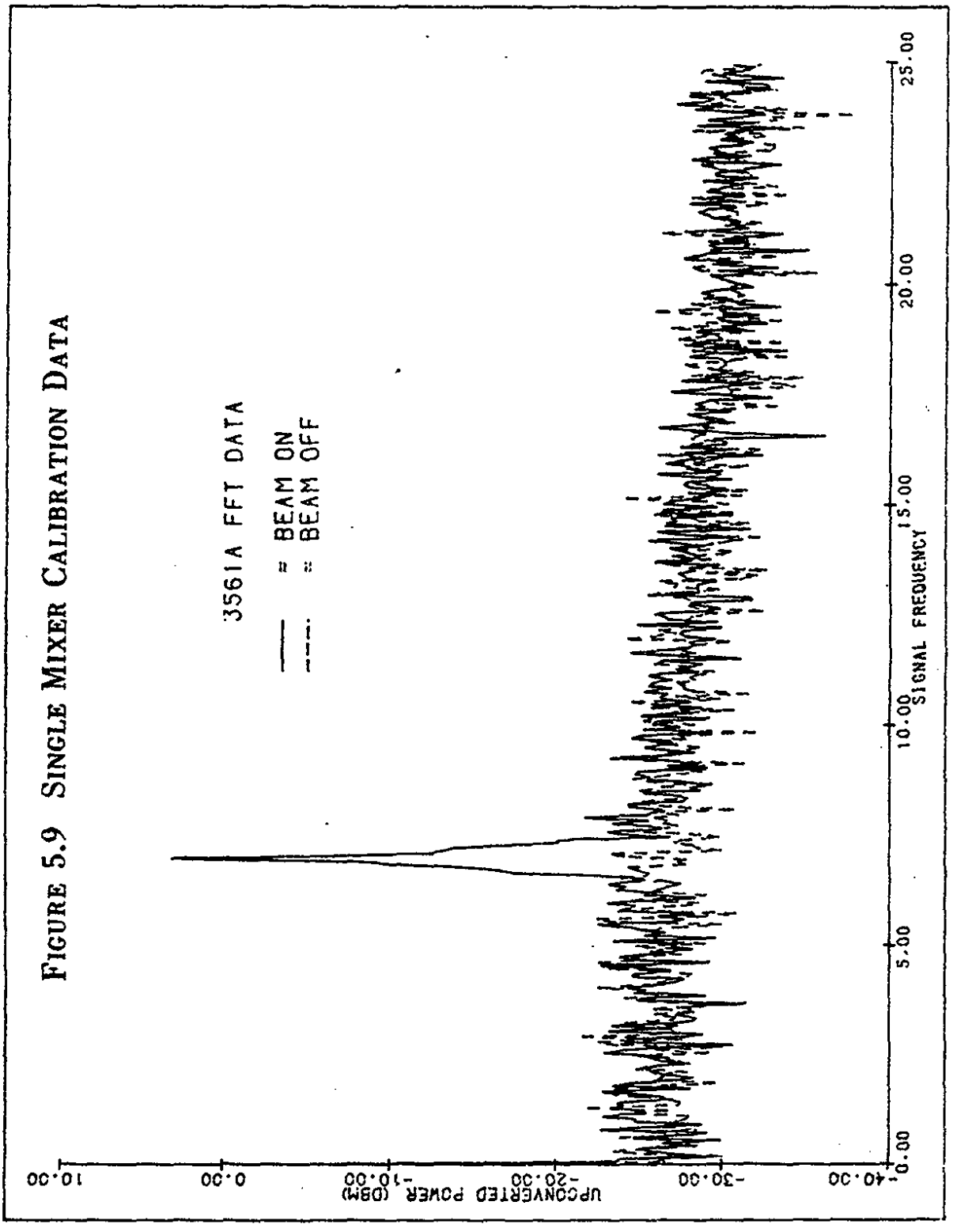

FIGURE 5.9 SINGLE MIXER CALIBRATION DATA

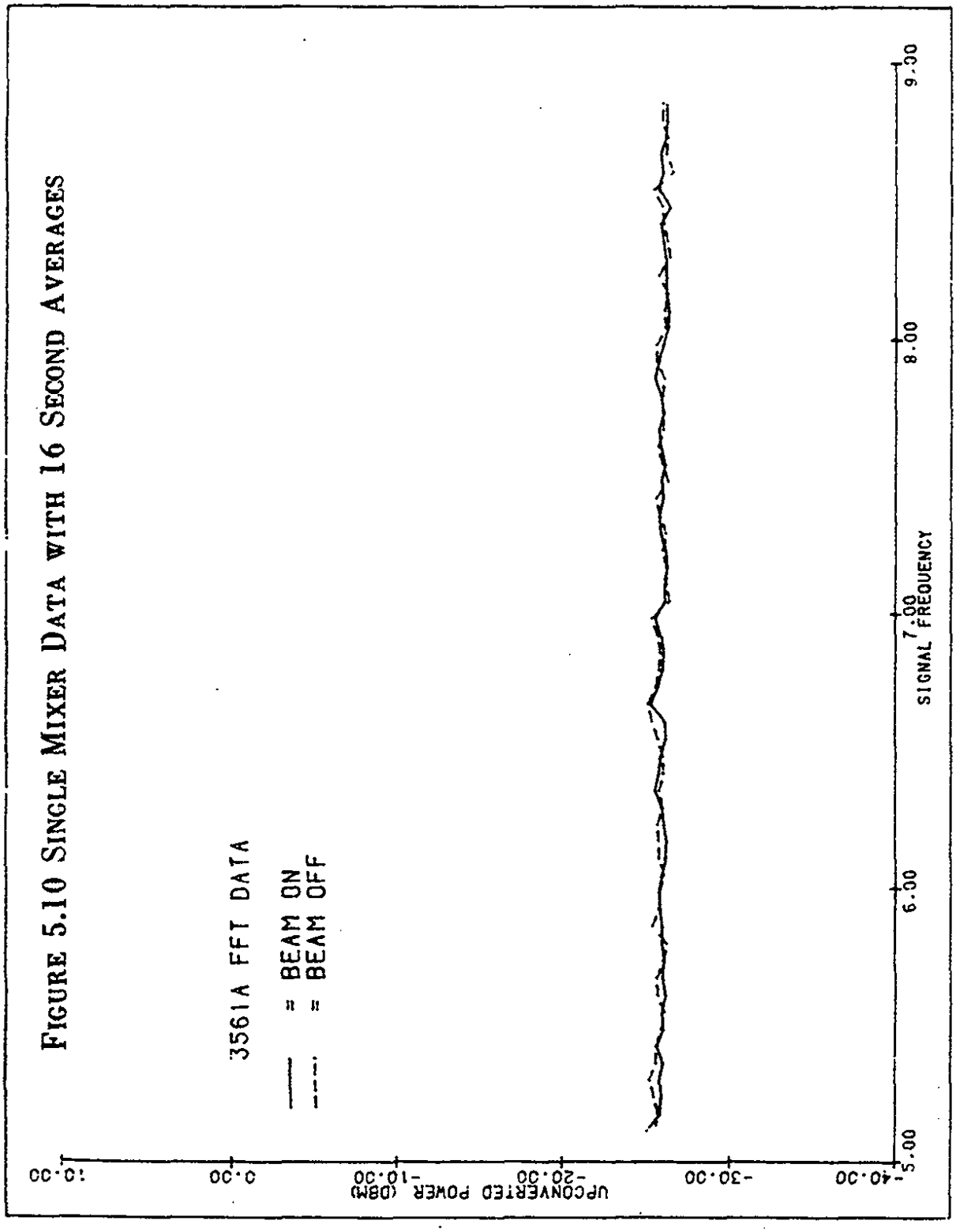

FIGURE 5.10 SINGLE MIXER DATA WITH 16 SECOND AVERAGES

measured at -50.46±.50 dBm). The dashed line in this figure shows the 495 averages of the ramp down signal when there is no beam left in the Tevatron after the spill. A direct comparison of these two figures shows that there was no obvious upconverted signal due to the passage of the beam by the detector.

The average detected signal (power) level at the frequency bin of interest for this data was -25.87 dBm per channel (in a single frequency bin). The total power gain of the system was 133.9±.5 dB so that the actual signal level at the cavities was -159.77 dBm or $(1.05\pm.06)\times10^{-19}$ Watts. The corresponding bandwidth of the detection system was 62.5 mHz.

The second data set was obtained with the averaging time set to 20 seconds for a corresponding bandwidth of 50 mHz. The calibration curve for this data is shown in figure 5.11 with -17.0±.5 dBm applied to the PZT from the beam pick-ups. The actual data is graphed in figure 5.12 with the signal of interest at 7.000±.025 Hz. The average beam intensity for this data was $(5.94\pm.02)\times10^{12}$ (with an average 26^{th} harmonic size of -49.14±.50 dBm). The average upconverted signal was -25.60 dBm corresponding to -159.50 dBm or $(1.12\pm.10)\times10^{-19}$ Watts in a 50 mHz bandwidth. The total number of averages for this data set was 168.

5.4.2 Two Mixer Mode

The data discussed here were taken with the two mixer detection

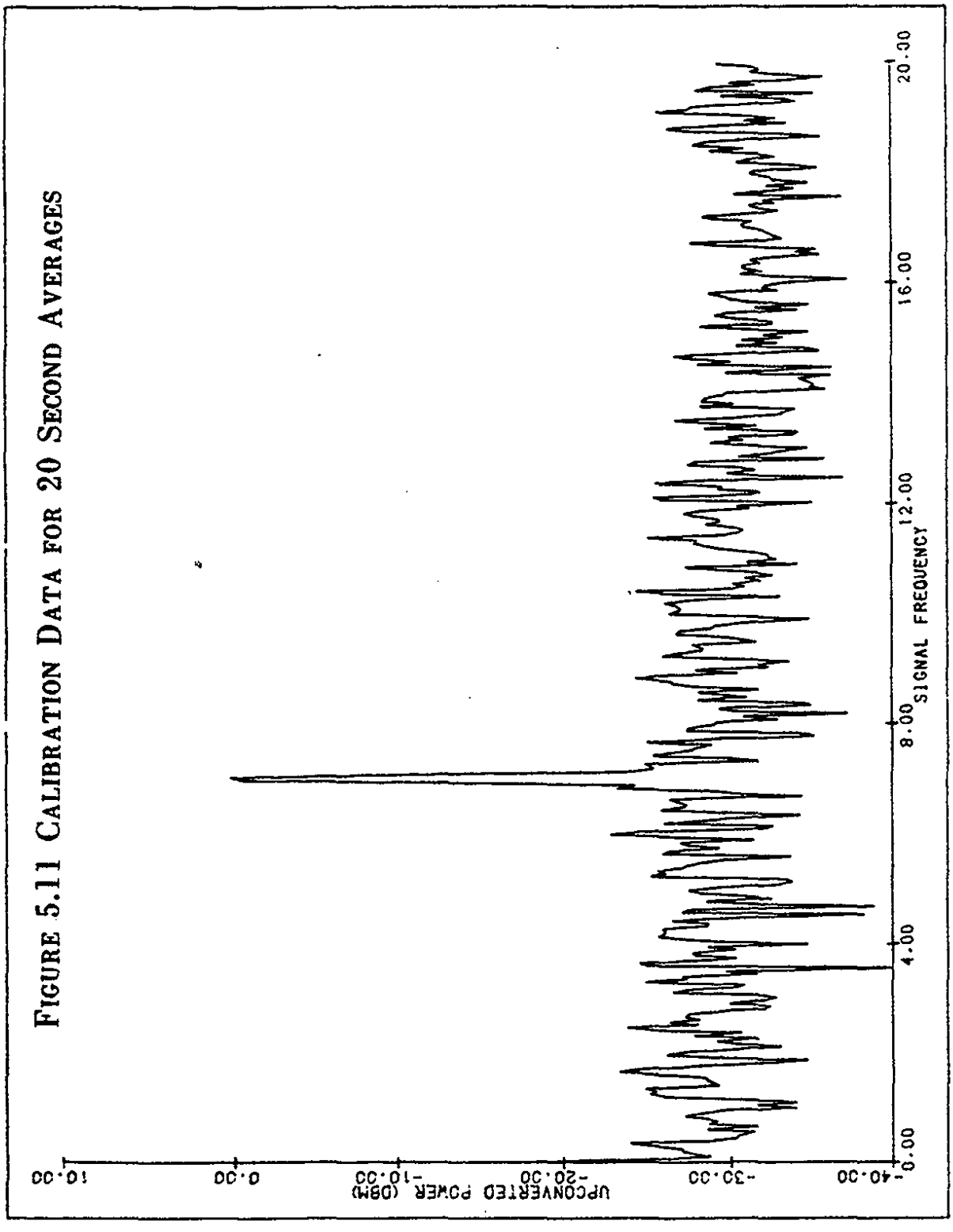

FIGURE 5.11 CALIBRATION DATA FOR 20 SECOND AVERAGES

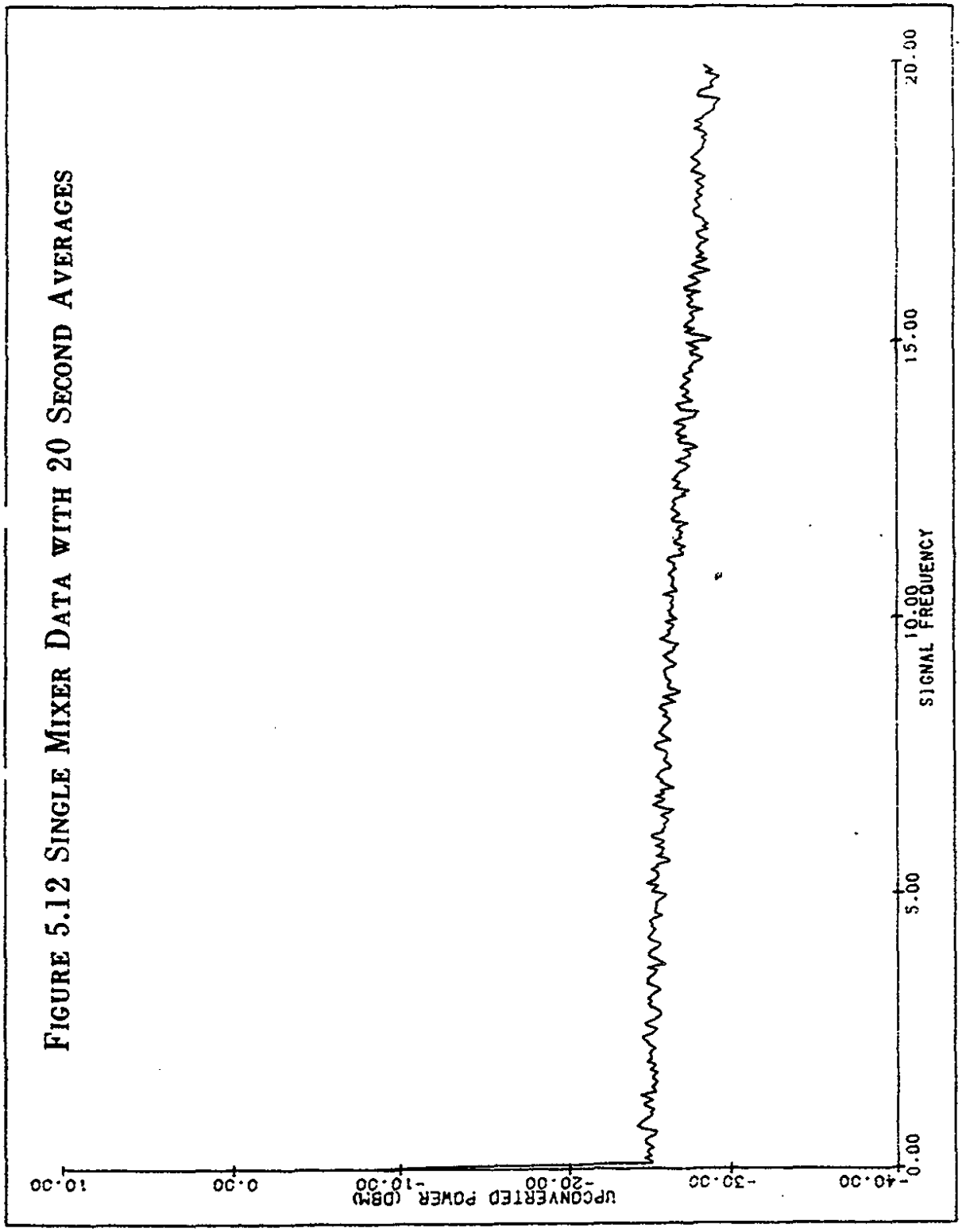

FIGURE 5.12 SINGLE MIXER DATA WITH 20 SECOND AVERAGES

scheme described in section 4.7. This detection system had the advantage that it accurately tracked the frequency of the beam throughout the entire ramp cycle so that the output signal at the FFT was always precisely at 7.000±.025 Hz. Thus longer integration times and hence narrower bandwidths could be achieved than with the single mixer scheme.

The first data set consists of 301 averages with an averaging time of 40 seconds each beginning at the start of the magnet ramp. The corresponding bandwidth was 25 mHz. The overall gain of the detection electronics was again 133.9±.5 dB with an input power to the cavities of 5.58±.05 mW.

The calibration for this run is shown in figure 5.13 and was obtained by applying -19.6 dBm from the beam synchronous signal at the 26^{th} harmonic into the PZT. The data is plotted in figure 5.14 and has an average signal at the bin of interest level of -34.30±.50 dBm. The resulting level at the cavities was $(1.51\pm.11)\times10^{-20}$ Watts. The average intensity was 3.20×10^{12} protons (with a measured average 26^{th} harmonic size of -56.8±.5 dBm).

For the second data set obtained with the two mixer scheme the integration time was 1250.0 seconds which spanned 15 consecutive beam cycles with an equivalent bandwidth of 800 μHz. The expected beam induced signal does not arrive with the same phase for every beam cycle and furthermore, the beam only appears for 50% of the total beam cycle. The result is that the signal to noise ratio does not improve by increasing the integration time beyond 40 seconds. This is demonstrated in figure 5.15 which shows the output from the

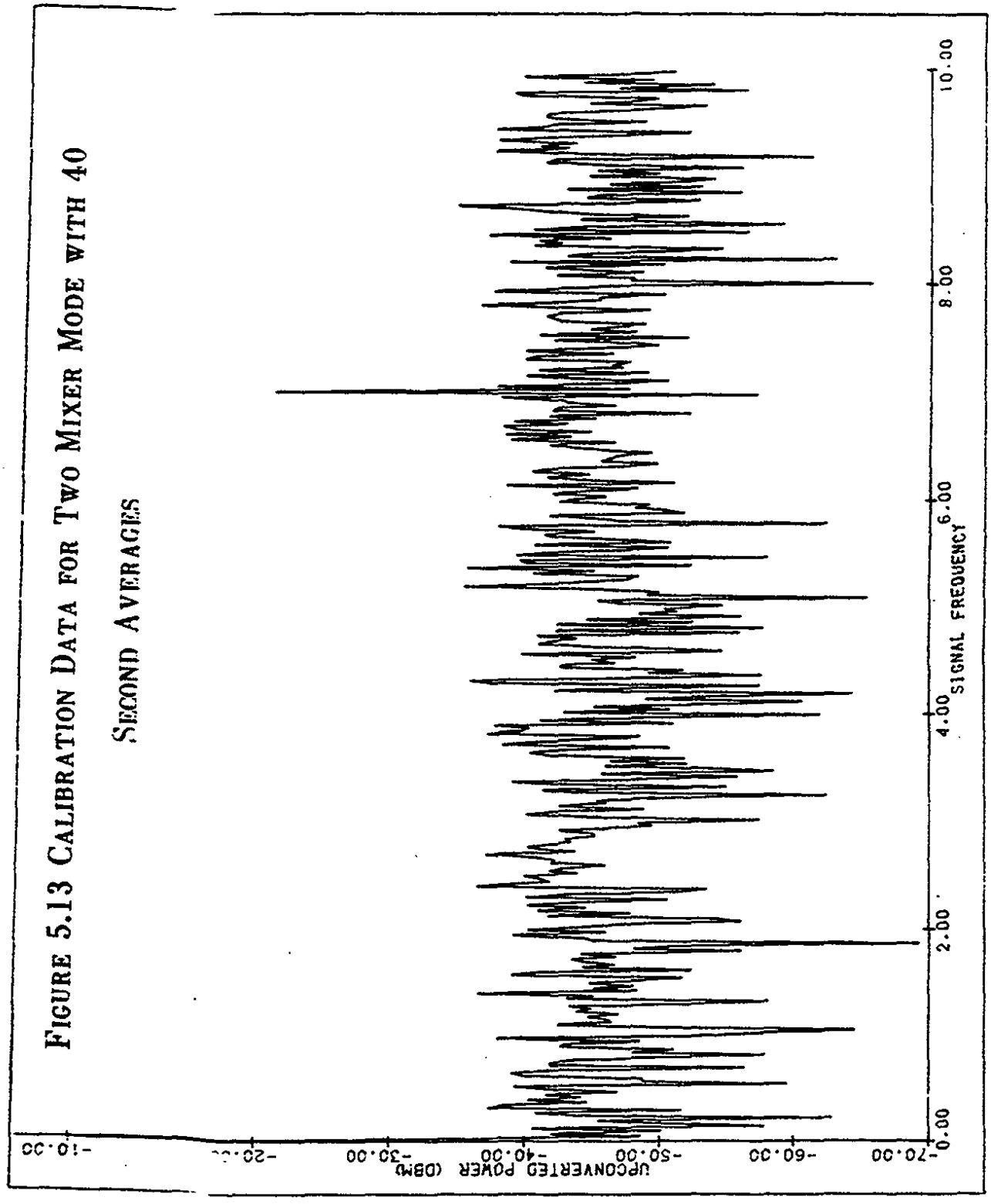

FIGURE 5.13 CALIBRATION DATA FOR TWO MIXER MODE WITH 40 SECOND AVERAGES

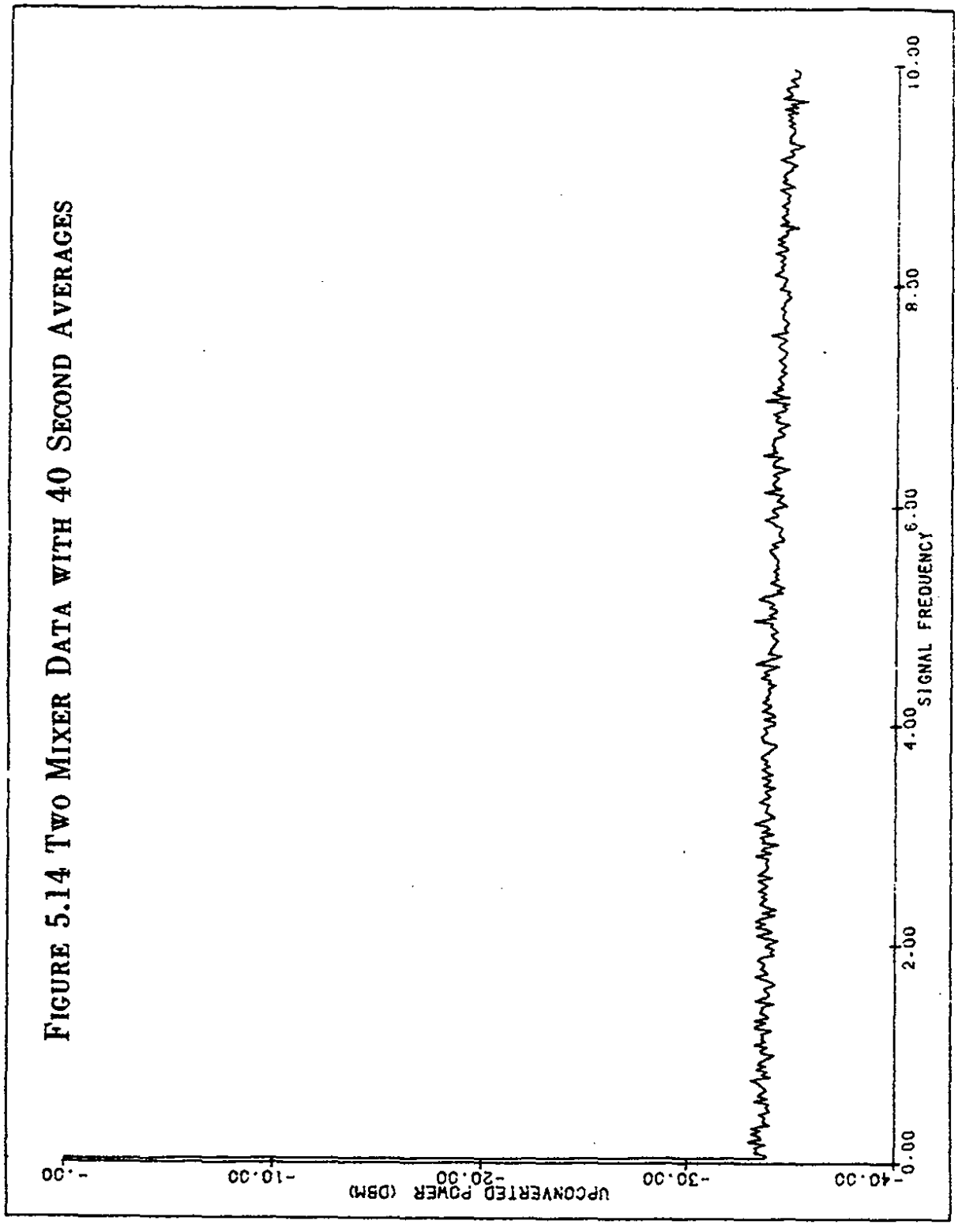

FIGURE 5.14 TWO MIXER DATA WITH 40 SECOND AVERAGES

beam pick-ups applied to the PZT with a bandwidth of 800μHz. The calibration signal now appears to be spread out over several frequency bins as expected. The bandwidth of the upconverted signal was estimated from this curve to be ~25 mHz. The 11 mHz structure which appears is due to the fact that the cycle time was 90 seconds and thus introduces a corresponding beat frequency at (1/90)≈11 mHz.

Figure 5.16 shows 10 averages with the signal of interest centered at 7.000±.025 Hz. The average intensity for this data was $(5.39\pm.02)\times10^{12}$ protons. The upconverted signal level in the bin at 7.000±.025 Hz was -44.67 dBm corresponding to $(1.39X\pm.4)10^{-21}$ Watts in a 800 μHz bandwidth. Thus the power over the 25 mHz width of the signal is approximately 3.5×10^{-20} Watts.

One final data set for this system was measured with an integration time of 7.8125×10^{3} seconds and is shown in figure 5.17. The corresponding bandwidth was 128 μHz. The average signal level at the frequency of interest was -61.2±3.0 dBm or $(3.08\pm3.0)\times10^{-23}$ Watts at the cavities and represents the smallest measured output power to date. The average intensity of the proton beam was $(4.0\pm.1)\times10^{12}$ with a corresponding 26^{th} harmonic of -56.0±.5 dBm. The total frequency span of this measurement is twice the bandwidth of the expected upconverted signal so that no general conclusions about limits on the size of such a signal can be drawn from this measurement.

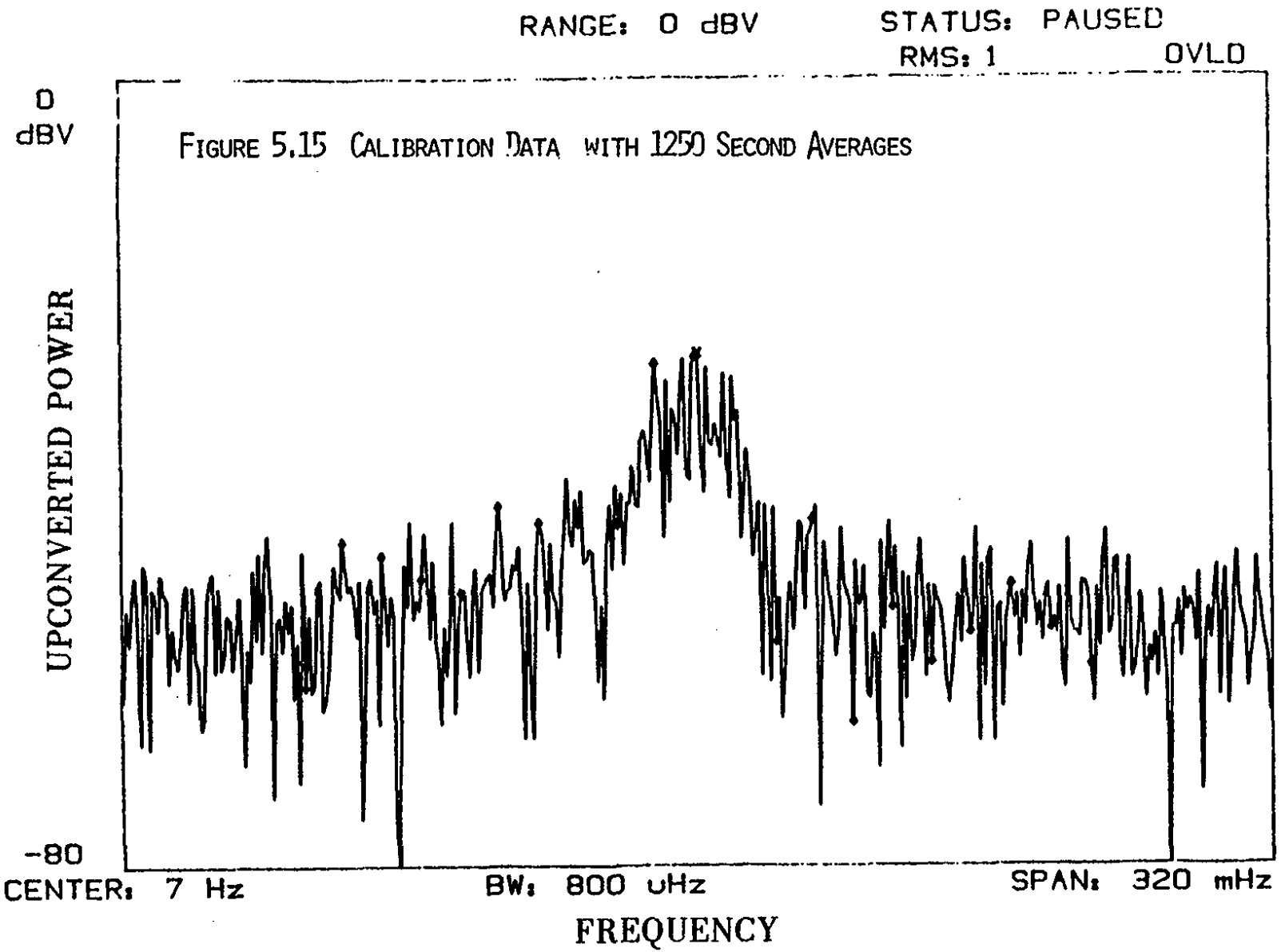
RANGE: 0 dBV
STATUS: PAUSED
RMS: 1
OVLD
0
dBV
FIGURE 5.15 CALIBRATION DATA WITH 1250 SECOND AVERAGES
UPCONVERTED POWER
-80
CENTER: 7 Hz
BW: 800 uHz
SPAN: 320 mHz
FREQUENCY

90T

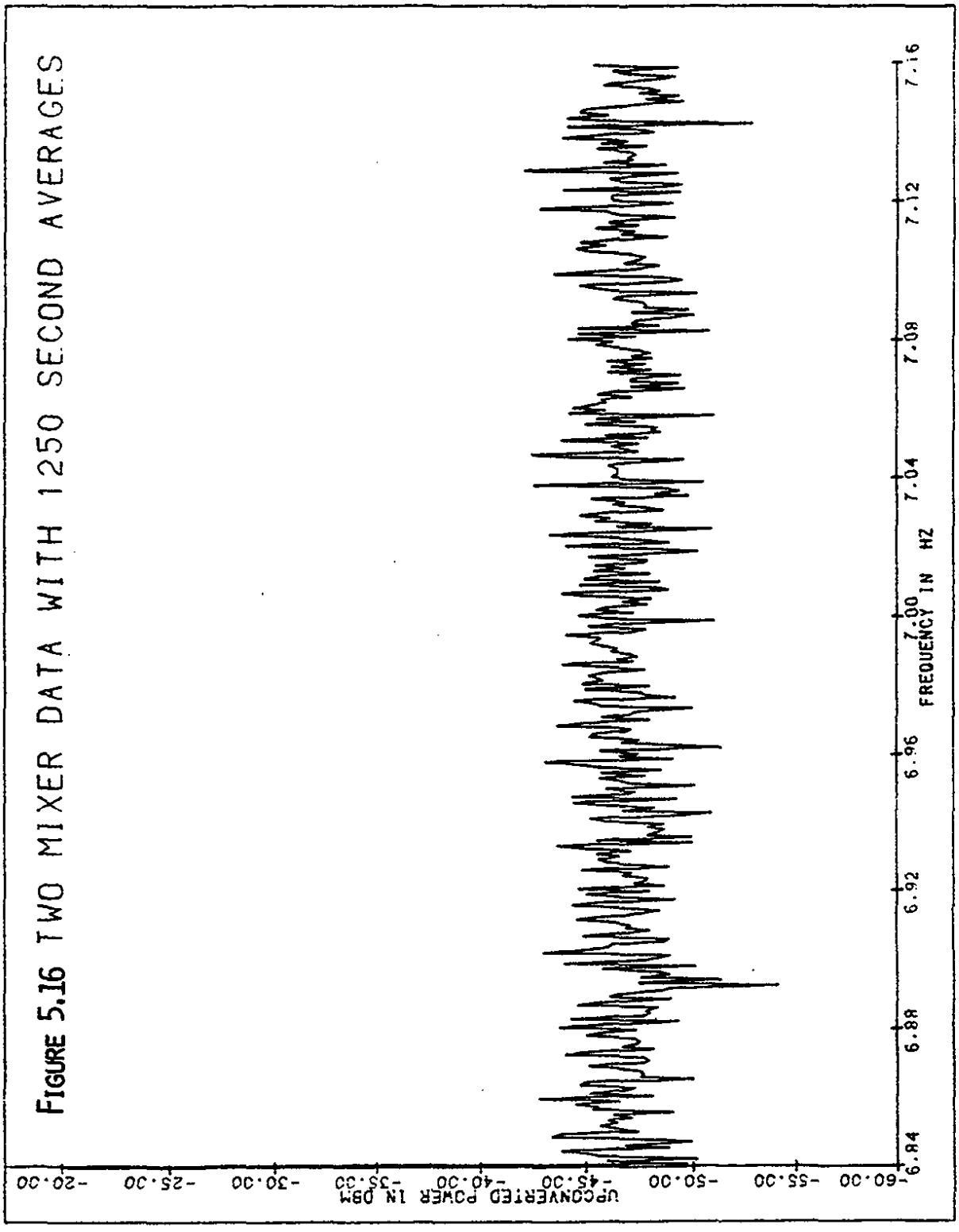

FIGURE 5.16 TWO MIXER DATA WITH 1250 SECOND AVERAGES

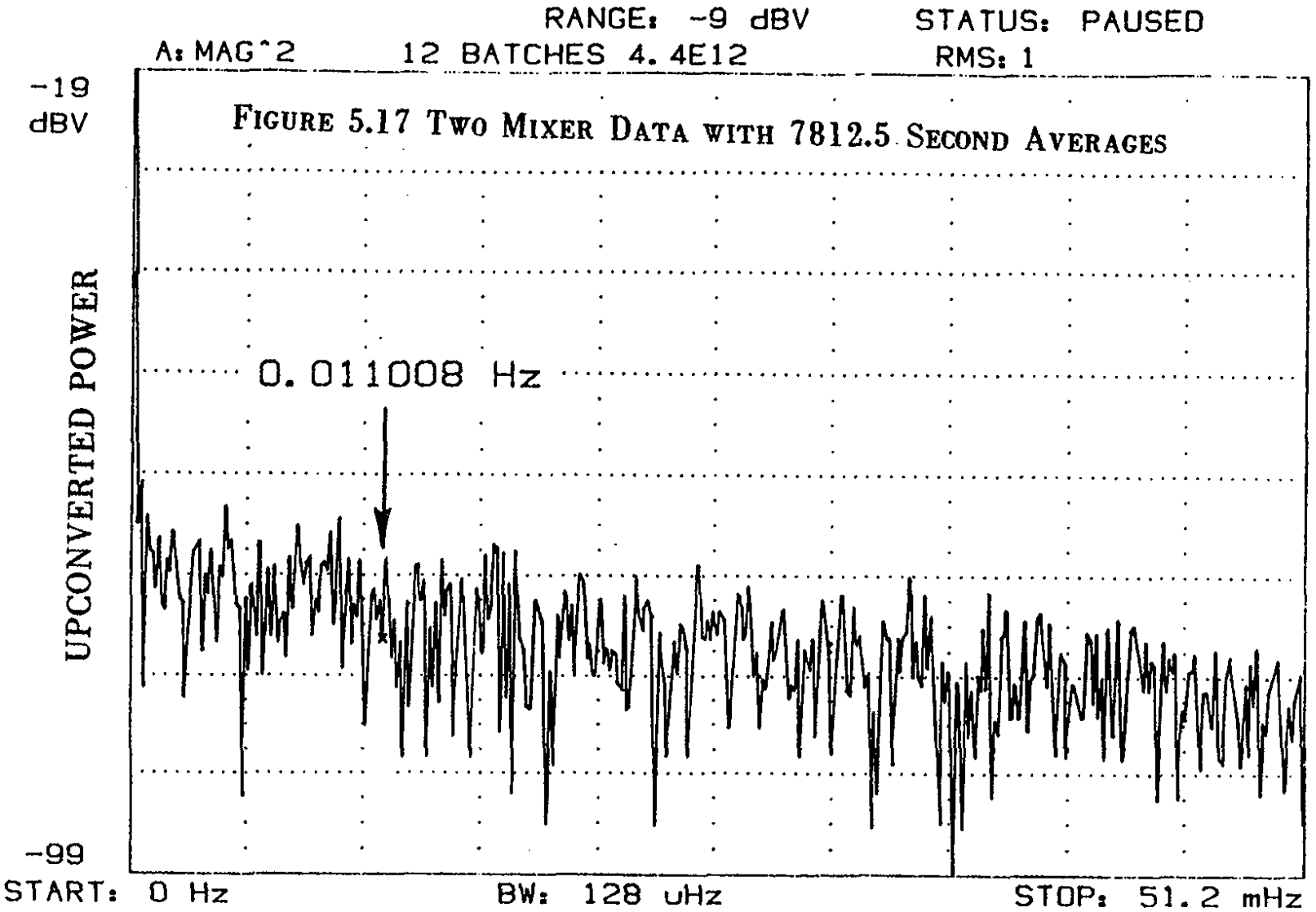

FIGURE 5.17 TWO MIXER DATA WITH 7812.5 SECOND AVERAGES

5.4.3 Dual Channel FFT Detection Scheme

The data presented here was measured with the dual channel spectrum analyzer scheme shown in figure 4.11. The advantage of this scheme is that the upconverted signal can be directly compared and correlated to the beam pick-up signal at the 26^{th} harmonic. This scheme takes full advantage of the knowledge of the constant phase relationship between the beam induced signal and the passage of the beam near the detector. Any spurious uncorrelated signal can thus be effectively eliminated by using the analysis techniques described in section 3.4.

The data logged using this system consisted of 25 second averages beginning 5 seconds before the start of flattop. The desired signal frequency was chosen to be 1019.00±.04 Hz and the HP3582A frequency span was adjusted so that a signal at 1019 Hz would appear in the central frequency bin (64). A calibration run for this scheme at 1.97°K was made by placing the output from the beam syncronous signal into strain gauge 1 and is shown in figure 5.18. The first data set consists of 410 averages taken at 4.20° K with a bandwidth of 40 mHz. The average intensity for this run was $(8.41\pm.02)\times10^{12}$ protons. Figure 5.19 shows the size of the upconverted signals measured by channel A of the HP3582A FFT. The top curve represents a straight power average of channel A and the jagged curve below is the corresponding voltage average. This average was performed by first shifting the phase of channel A by the corresponding phase of channel B bin by bin. This graph clearly

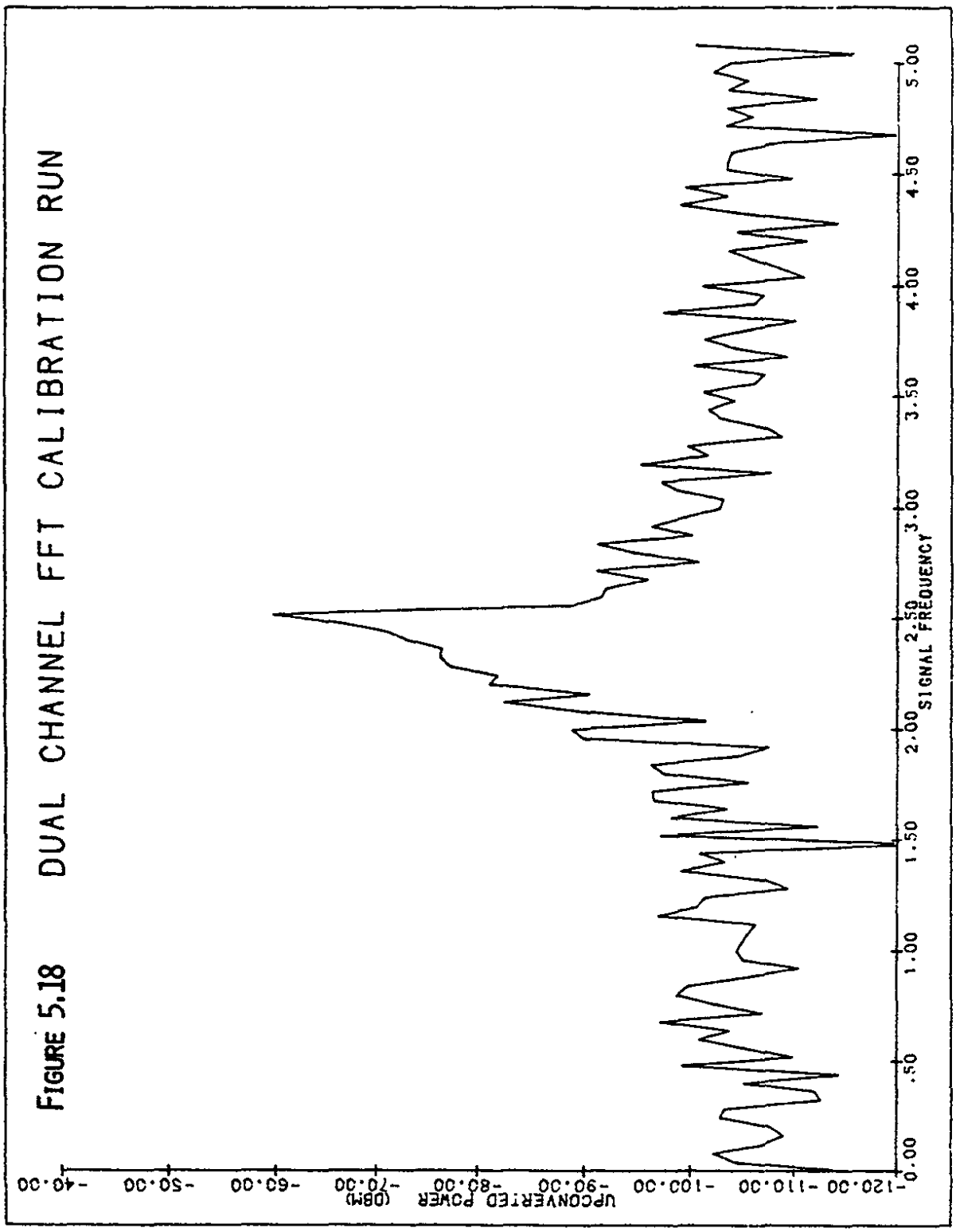
DUAL CHANNEL FFT CALIBRATION RUN
UPCONVERTED POWER (DBM)
-40.00
-50.00
-60.00
-70.00
-80.00
-90.00
-100.00
-110.00
-120.00
0.00
.50
1.00
1.50
2.00
2.50
3.00
3.50
4.00
4.50
5.00
SIGNAL FREQUENCY

FIGURE 5.18

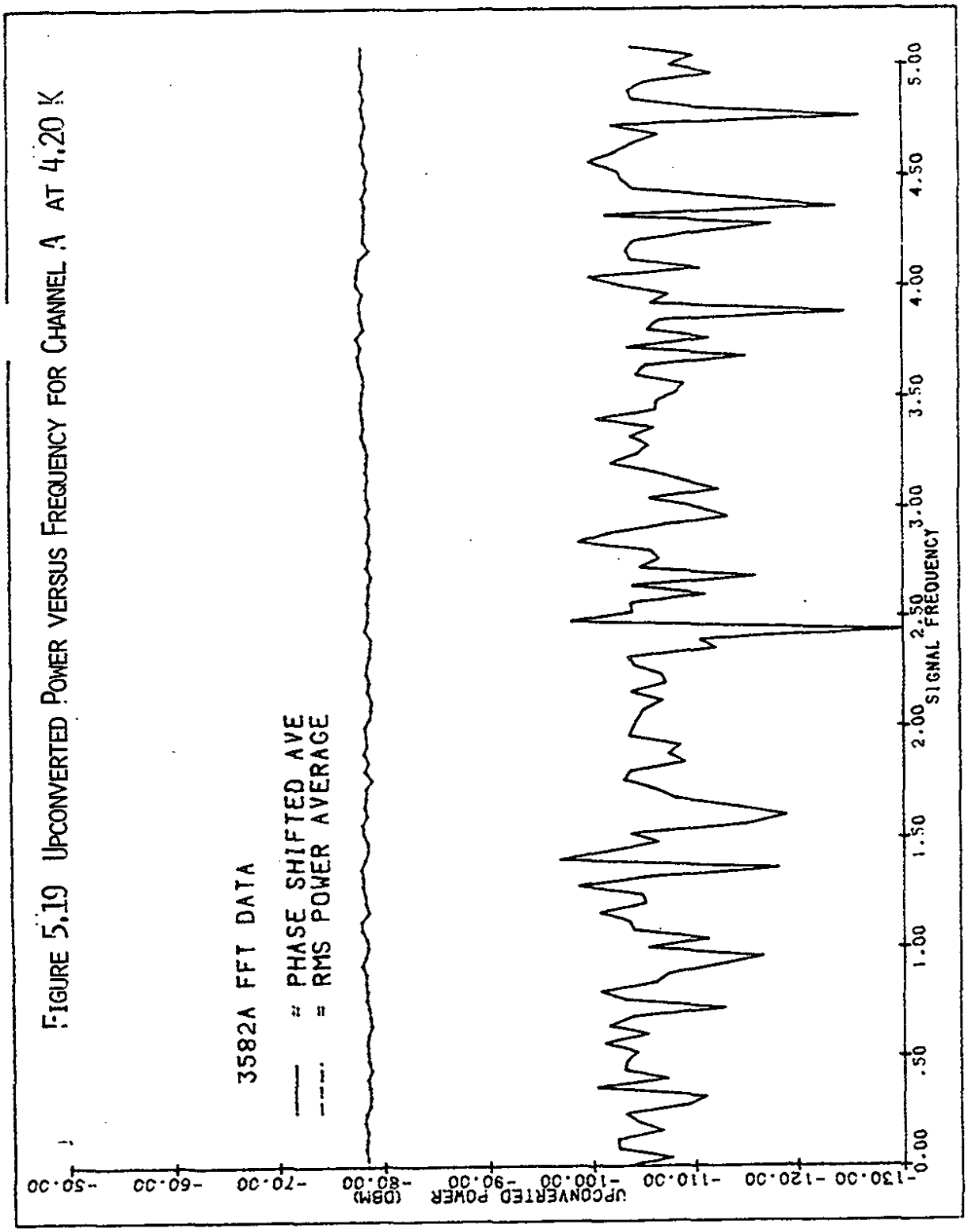

FIGURE 5.19 UPCONVERTED POWER VERSUS FREQUENCY FOR CHANNEL A AT 4.20 K

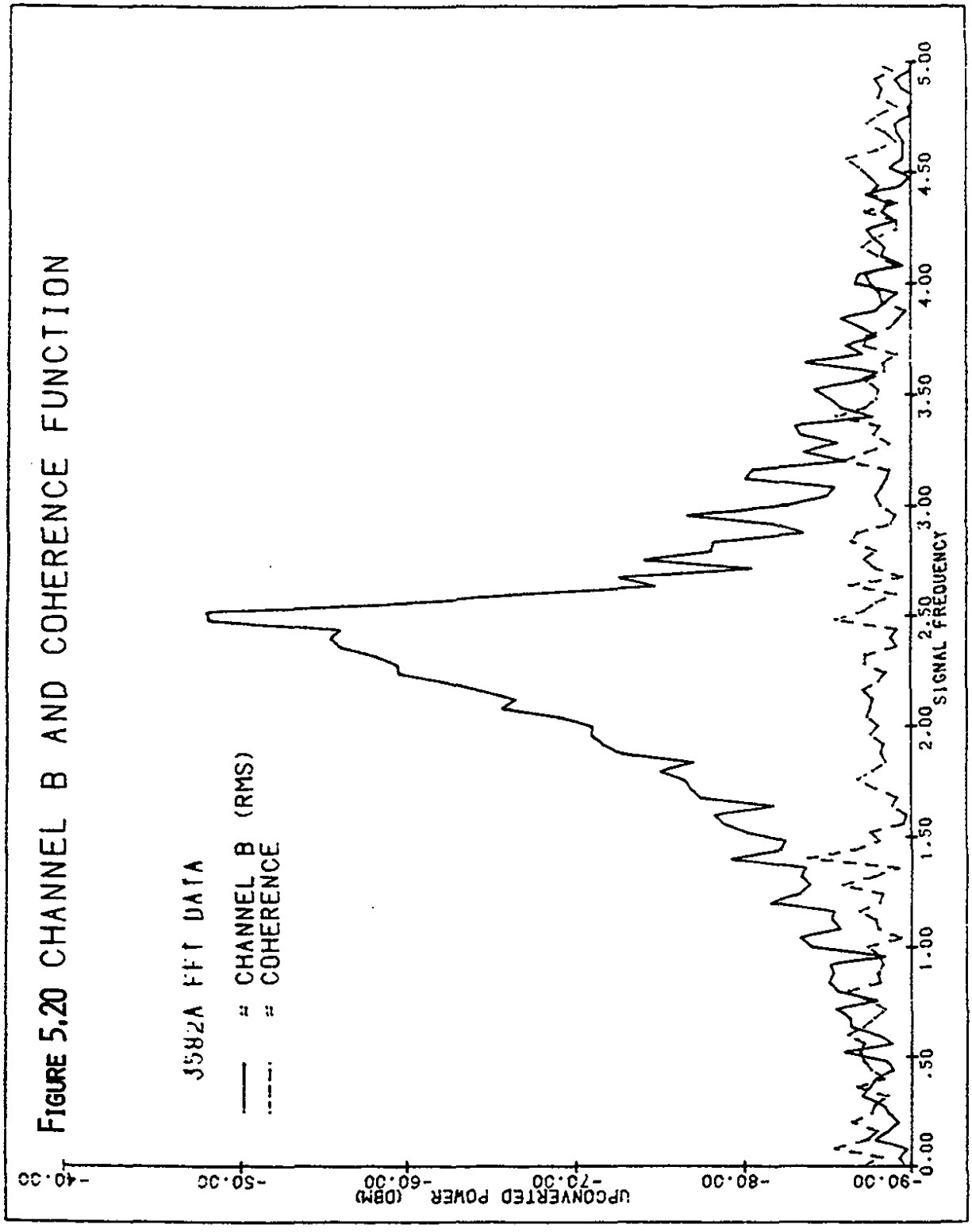
FIGURE 5.20 CHANNEL B AND COHERENCE FUNCTION
3582A FFT DATA
= CHANNEL B (RMS)
= COHERENCE
UPCONVERTED POWER (DBM)
-40.00
-50.00
-60.00
-70.00
-80.00
-90.00
0.00
.50
1.00
1.50
2.00
2.50
3.00
3.50
4.00
4.50
5.00
SIGNAL FREQUENCY

shows that the noise background has decreased for the phase shifted average (voltage average) and that the power average has a smaller relative variance in the background level. The size of the 26^{th} harmonic measured simultaneously by channel B is plotted in figure 5.20 as the solid curve and the dashed curve represents the measured coherence between the two channels. The shape of the 26^{th} harmonic results from averaging over 5 seconds of the ramp cycle before the start of flattop for which the frequency changes by approximately 5Hz. The largest value of channel B occurs in the 64^{th} frequency bin of the FFT precisely at 1019.00±.04 Hz as desired. The coherence function plotted in figure 5.20 by the dashed curve is a relative measure of the cross correlation between the two channels and is calculated as described in chapter 3. This figure shows that it is uncertain that a signal exists at the desired frequency which is coherent with the beam pick-up signal at 1.240540 MHz.

The gain of this system was 80.4±.5 dB so that the signal measured for the phase shifted average was -181.1±3.0 dBm or $(7.8\pm7.7)\times10^{-22}$ Watts in frequency bin 63 and -184.1±.5 dBm or $(3.9\pm3.6)\times10^{-22}$ Watts in frequency bin 64. The bandwidth of the detection system in this case was 40 mHz so that each frequency bin also spanned 40 mHz. The rms (root mean square) power average of channel A was -159.1±.2 dBm $(1.2\pm.1)\times10^{-19}$ W in bin 63 with a coherence of $\xi=.09\pm.01$ and $(1.2\pm.1)\times10^{-19}$ W in bin 64 with a coherence of $\xi=.06\pm.01$. We can use equations 3.25 and 3.26 to calculate the average noise background and the maximum size of the desired signal.

For bin 63,

$$N_{63}(\omega) = (1-\xi^2)\langle A^*A\rangle = (1.2\pm.1)\times10^{-19} \text{ Watts}$$

$$S_{63}(\omega) = \xi^2\langle A^*A\rangle = (9.7\pm.5)\times10^{-22} \text{ Watts}$$

and for bin 64,

$$N_{64} = (1.2\pm.1)\times10^{-19} \text{ Watts}$$

$$S_{64} = (4.3\pm.5)\times10^{-22} \text{ Watts}$$

Note that these measurements refer to power in a 40 mHz bandwidth.

These results are in agreement with the values obtained from the phase shifted voltage average for both frequency bins.

The run was repeated with the cavities at a temperature of 1.89°K and the overall power gain for the system was 74.4±.5 dB. The results are shown in figures 5.21 and 5.22. The average intensity for this data was $(7.87\pm.02)\times10^{12}$ and consisted of 12 booster batches in the ring with 4 RF buckets missing in the gaps between the batches. Data cuts were made for this and the preceding data run to exclude spectra for which there was little or no beam in the Tevatron. The results contain the average of the remaining 112 beam cycles. The average signal level was -91.7 dBm so that the corresponding power level upconverted at the cavities was -161.0±3.0

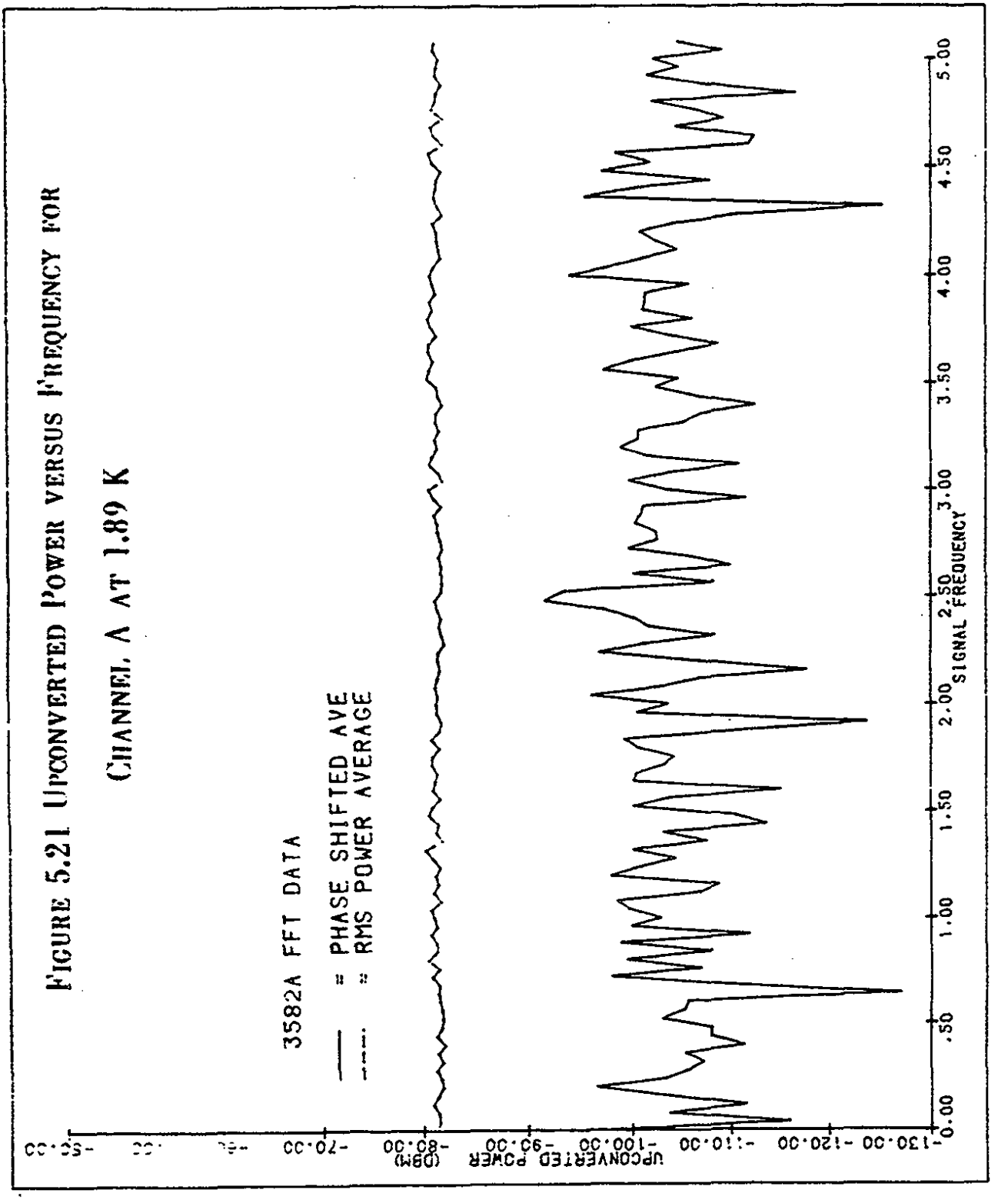

FIGURE 5.21 UPCONVERTED POWER VERSUS FREQUENCY FOR CHANNEL A AT 1.89 K

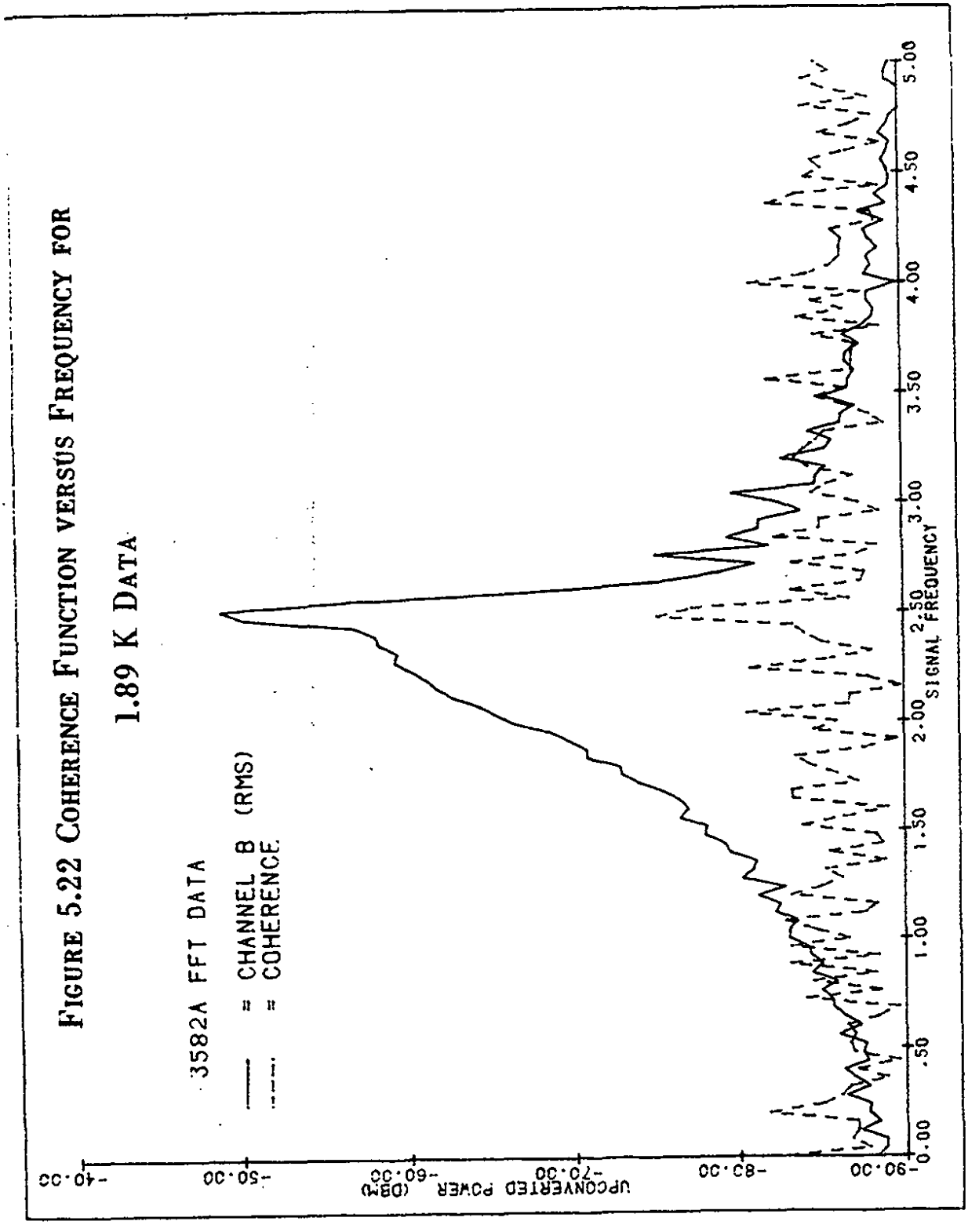

FIGURE 5.22 COHERENCE FUNCTION VERSUS FREQUENCY FOR 1.89 K DATA

dBm or $(2.5\pm2.4)\times10^{-20}$ Watts in bin 63 and -168.0±3.0 dBm or $(1.6\pm1.5)\times10^{-20}$ Watts in bin 64. The average 26^{th} harmonic in the same bin was -48.9±2.0 dBm. The rms (root mean square) power average of channel A was -156.1 dBm ($2.5\pm.1\times10^{-19}$ W) in bin 63 with a coherence of $\xi=.30\pm.05$ and ($2.1\pm.1\times10^{-19}$ W) in bin 64 with a coherence of $\xi=.25\pm.05$. We can again calculate the average noise power and the maximum size of any upconverted signal.

For bin 63,

$$N_{63}(\omega) = (1-\xi^2)\left\langle A^*A\right\rangle = (2.3\pm.1)\times10^{-19} \text{ Watts}$$

$$S_{63}(\omega) = \xi^2\left\langle A^*A\right\rangle = \quad (2.3\pm.1)\times10^{-20} \text{ Watts}$$

and for bin 64,

$$N_{64} = (2.0\pm.1)\times10^{-19} \text{ Watts}$$

$$S_{64} = (1.3\pm.1)\times10^{-20} \text{ Watts}$$

From figure 5.21 we see that a signal appears with the phase shifted voltage average at the desired frequency. The coherence function is plotted in figure 5.22 (dashed curve) and shows that a beam induced signal is present. A discussion of the origin of this signal is given in chapter 6.

The only detector parameters which changed for the data run at 1.89° K compared to the run at 4.20° K were the electrical Q of the cavities and the overall gain of the detection systems. We assume for this discussion that the mechanical structure has not changed significantly between the runs. Since the power in the 26^{th} harmonic was essentially the same, we expect that any beam induced signal detected by the transducer must also be the same.

Now let $X_1^2=\xi_1^2 S_1$ and $X_2^2=\xi_2^2 S_2$ be the expected signals for the 4.2° and the 1.9° run respectively where S_1 and S_2 are the upconverted power levels and ξ_1^2 and ξ_2^2 are the corresponding values for the coherence squared. If all other parameters are constant i.e. $X_1^2=X_2^2$, It must hold that

$$\frac{\xi_2^2}{\xi_1^2} = \frac{S_1}{S_2} \tag{5.3}$$

In accordance with equation 5.1,

$$\left(\frac{\xi_2}{\xi_1}\right)^2 = \left(\frac{Q_2}{Q_1}\right) \tag{5.4}$$

where Q_1 and Q_2 are the electrical Q values for the 4.2° and 1.89° data runs respectively. Thus for bin 63,

$$\left(\frac{\xi_2}{\xi_1}\right)^2 = \left(\frac{.30}{.09}\right)^2 \approx 11$$

whereas,

$$\left(\frac{Q_2}{Q_1}\right)^2 = \left(\frac{3.0}{1.24}\right)^2 \approx 6$$

For bin 64 we obtain,

$$\left(\frac{\xi_2}{\xi_1}\right)^2 = \left(\frac{.25}{.06}\right)^2 \approx 17$$

whereas $(Q_2/Q_1)^2$ has the same value as before. While these signal levels show the correct tendency the estimated systematic errors are too large to establish quantitative agreement. We therefore treat the corresponding signal levels (given by $\xi^2 S_2$) as an upper limit on a possible upconverted signal.

The results of the data runs are summarized in table 5.2 and the corresponding limit on beam induced displacements Δl are given in table 5.3.

Table 5.2

Measured Upconverted Power

Data Set Description	Averages	Bandwidth (mHz)	Intensity	Power in 26th Harmonic
(1)[1] 16 second averages	495	62.5	6.62×10^{12}	-50.46
(2)[1] 20 second averages	168	50.0	5.94×10^{12}	-49.14
(3)[2] 40 second averages	301	25.0	3.20×10^{12}	-56.80
(4)[2] 1250 second averages	10	.800	5.39×10^{12}	-56.0
(5)[2] 7812.5 second averages	1	.128	4.00×10^{12}	-56.0
(6)[3] 25 second averages	410	40.0	8.41×10^{12}	-48.04
(7)[3] 25 second averages	112	40.0	7.87×10^{12}	-48.90

[1] fixed frequency reference power average
[2] beam frequency reference power average
[3] fixed frequency, phase sensitive voltage average

Data Set	Power at FFT	Gain dB	P_2 (dBm)	P_2 (Watts)	P_2/P_1 *
1	-38.87	133.9	-159.77	1.05×10^{-19}	1.89×10^{-17}
2	-38.60	133.9	-159.50	1.12×10^{-19}	2.01×10^{-17}
3	-47.30	133.9	-168.20	1.51×10^{-20}	2.71×10^{-18}
4	-57.67	133.9	-178.57	2.20×10^{-20}	3.94×10^{-18} **
5	-74.22	133.9	-195.12	3.08×10^{-23} ***	----------
6 (bin 63)	-113.7	80.4	-181.1	7.76×10^{-22}	1.39×10^{-19}
6 (bin 64)	-116.7	80.4	-184.1	3.89×10^{-22}	6.97×10^{-20}
7 (bin 63)	-104.7	74.4	-166.1	2.45×10^{-20}	4.40×10^{-18}
7 (bin 64)	-106.6	74.4	-168.0	1.58×10^{-20}	2.84×10^{-18}

* P_1=5.58 mW

** The average power for this data set is calculated by multiplying the observed power by the ratio of the signal width (25 mHz) to the detection bandwidth (.800 mHz).

*** This data set was taken with a .128 mHz bandwidth and can not be used to estimate the effective strain applied to the cavities.

Table 5.3

Measured Limits on Effective Harmonic Displacements*

Data Set	Q_1	Q_2	Bandwidth (mHz)	Δl in cm	Error** ±cm
1	1.24×10^{7}	1.29×10^{7}	62.5	2.0×10^{-14}	$\pm6\times10^{-16}$
2	1.24×10^{7}	1.29×10^{7}	50.0	2.0×10^{-14}	$\pm9\times10^{-16}$
3	1.24×10^{7}	1.29×10^{7}	25.0	7.5×10^{-15}	$\pm6\times10^{-16}$
4	1.24×10^{7}	1.29×10^{7}	.800	9.0×10^{-15}	$\pm1.3\times10^{-15}$
5	1.24×10^{7}	1.29×10^{7}	.128	*********	*********
6 (bin 63)	1.24×10^{7}	1.29×10^{7}	40.0	1.7×10^{-15}	$\pm1.6\times10^{-15}$
6 (bin 64)	1.24×10^{7}	1.29×10^{7}	40.0	1.2×10^{-15}	$\pm1.2\times10^{-15}$
7 (bin 63)	3.0×10^{7}	3.1×10^{7}	40.0	4.0×10^{-15}	$\pm3.6\times10^{-15}$
7 (bin 64)	3.0×10^{7}	3.1×10^{7}	40.0	3.2×10^{-15}	$\pm3.1\times10^{-15}$

* All values for Δl are calculated from the following equation:

$$\Delta l = 57.4 \left[\frac{P_2}{P_1} \left(\frac{1}{Q_1 Q_2} \right) \right]^{\frac{1}{2}}$$

** *Errors are calculated from the variance σ associated with each measurement.*

$$\text{Error} = \frac{\sigma}{\langle \Delta l \rangle}$$

Chapter 6

Conclusions

6.1 Overview

The limits on the coherent signal observed in the detector were presented in the previous chapter. In order to place limits on the size of other possible long range forces, we must assume a particular form for the interaction. We choose a form identical to that of the gravitational interaction, namely a 1/r potential.

$$V_A = G_A \cdot \frac{m_1 m_2}{r} \tag{6.1}$$

where G_A is the "anomalous" coupling constant. The interaction is then proportional to the mass of the beam particles (protons) and the mass of the detector. Since the gravitational and inertial mass of the detector are presumed equal, the acceleration of the detector is

$$a = \frac{F}{M} = -G_A m_p N \cdot \vec{\nabla}\left(\frac{1}{r}\right) \tag{6.2}$$

where N is the number of protons in the beam. The expression above is valid in the limit of Newtonian velocities and has to be modified as discussed in chapter 1 (equation 1.3) for relativistic velocities. Let $\langle a_G \rangle$ be the average acceleration arising from the gravitational interaction, namely from the potential of equation 6.1 with G_A replaced by Newton's constant G_N. If the limit on the observed average acceleration is $\langle a \rangle_1$ then we can place the following limit on G_A.

$$\frac{G_A}{G_N} = \frac{\langle a_{observed} \rangle}{\langle a_G \rangle} < \frac{\langle a \rangle_1}{\langle a_G \rangle} \tag{6.3}$$

or

$$G_A < G_N \frac{\langle a \rangle_1}{\langle a_G \rangle} \tag{6.3'}$$

An alternate interpretation of the results is to consider the direct coupling of the long range force to the electromagnetic field in the detector. We know that such a coupling exists for the gravitational field as discussed in chapter 1. In that case, the average perturbation of the metric is given by equation 1.3.

If the long range interaction couples to the stored electromagnetic field the same way that gravity does,

$$\frac{G_A}{G_N} = \frac{\langle h_{observed} \rangle}{\langle h_{00} \rangle} < \frac{\langle h \rangle_1}{\langle h_{00} \rangle} \tag{6.5}$$

or

$$G_A < G_N \frac{\langle h \rangle_1}{\langle h_{00} \rangle} \tag{6.5'}$$

The limit obtained through equation 6.5' is weaker than that of 6.3'. This is because the mechanical resonant structure of the detector amplifies the effects of the imposed acceleration.

It is important to stress that the anomalous long range interaction must reduce to a level below that of gravitation in the static limit regardless of the form of the interaction or the model chosen. Otherwise there would be a contradiction with the experiments discussed in section 1.1. If the range of the force has macroscopic dimensions but is not infinite, then the Cavendish type experiments and other experiments testing for deviations in the gravitational force law would be able to detect such interactions.[1]

In order to compare the coupling strength of the assumed interaction with that of electromagnetism, it is convenient to think of the potential of equation 6.1 as arising from the exchange of a massless gauge particle "a" with coupling g between two massive particles. In that case,

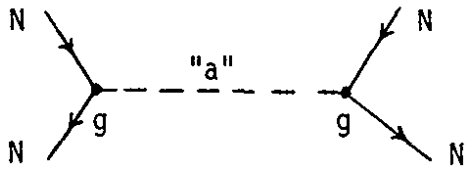

$$V = \frac{g^2}{4\pi r} \tag{6.6}$$

where the dimensionless quantity $g^2/\hbar c$ characterizes the strength of the coupling. Comparing equation 6.6 to equation 6.1 we find that

$$\frac{G_A m_p^2}{\hbar c} = \frac{g^2}{4\pi\hbar c} \tag{6.7}$$

assuming the interaction is between baryons. For electromagnetic interactions

$$\frac{g^2}{4\pi\hbar c} = \frac{e^2}{\hbar c} = \alpha = \frac{1}{137} \sim 10^{-2} \tag{6.8}$$

For the gravitational interaction

$$\frac{G_N m_p^2}{\hbar c} = 0.6\times10^{-38} \sim 10^{-38} \tag{6.9}$$

Equations 6.8 and 6.9 clearly show the extreme difference in the strength of the two known long range interactions.

In concluding this section we mention briefly other possible

long range forces that have been considered in the literature. The fact that the QCD color force is mediated by massless gluons implies that the force must be of long range. Such a force is not observed because only colorless (color singlets) particles are presumed to exist in nature. However, we can consider the possibility that higher order effects such as the exchange of multiple gluons will give rise to Van der Waal's color forces.[2] Such forces would have a rapid r dependence

$$V_N(r) \simeq \frac{\lambda_N}{r}\left(\frac{r_0}{r}\right)^{N-1} \qquad (6.10)$$

where $r_0 \sim 1$ Fermi is of the order of the nuclear scale, and $1 \leq N \leq 7$. Values of $N \leq 3$ can be excluded by existing experiments but there is no information for N between 4 and 7. The energy dependence of these forces is expected to be linear so that it is difficult to see how they can give rise to an anomalous interaction with strength of the order reported here.

Another possibility is related to the existence of very light particles that have been postulated to account for the symmetries of the strong and electroweak interaction. These particles are then exchanged between quarks and thus give rise to forces between electrically neutral matter. A particularly detailed model has been given for "axions" as an example.[3] However, in the static limit the strength of these forces is below that of gravitation. Furthermore, since the axion is a pseudo-scalar particle, the energy dependence

is 1/E or in terms of our experimemt, the coupling strength decreases with increasing γ. Another interesting possibility is related to the existence of light majorons.[4] These could give rise to a coupling of strength comparable to that of the gravitational interaction without violating existing evidence.

A different class of long range forces are those dependent on spin effects. Since matter is generally not polarized, these effects are absent from the well known tests of the gravitational interaction. Thus they can have considerably stronger couplings. However, since neither the proton beam nor the detector are polarized, the present experiment can not set limits on their strength.

6.2 Limits on Tidal Accelerations

The results of the 7 data sets reported in table 5.3 will be analyzed under the assumption that the differential tidal acceleration acting on the cavity sets it into mechanical vibration. As previously discussed, this will in general be a complex motion. However we have demonstrated that only mechanical vibrations at the difference frequency of the cavities can give rise to parametric conversion. The frequency difference of the cavities was carefully tuned to the 26^{th} harmonic of the beam revolution frequency so that only perturbations near this frequency (f_0=1.24054093 MHz) will contribute to the observed signal.

The average acceleration imparted by the beam on the detector is

$$\langle a \rangle = \frac{-m_{eff} G_N}{\pi \gamma b R} (2\gamma^2 \beta^2 + 1) \qquad (6.11)$$

where R is the radius of the Tevatron ring (it appears in this expression because of the periodicity of the beam) and b is the distance from the beam to the detector. m_{eff} is the fraction of the total mass in the beam that contributes a sinusoidal signal at the frequency of interest. As discussed in Appendix B, the effective mass can be determined from the ratio of the harmonic content of the beam at the 26^{th} harmonic to that at the 1113^{th} harmonic as follows;

$$m_{eff} = m_{beam} \frac{C_{26}}{C_{1113}} = m_p N \frac{C_{26}}{C_{1113}} \qquad (6.12)$$

with N the total number of circulating protons. The 1113^{th} harmonic is of course the frequency at which the individual buckets pass by the detector and give rise to the acceleration as calculated in equation 1.3. From the Fourier analysis of the beam as well as from direct measurements, it was found that $m_{eff} \approx m_{beam}/18.6$ for all of the data sets.

The measured limit on the size of this acceleration depends on the mechanical response of the detector at the 26^{th} harmonic. Information on the mechanical response was obtained from the PZT excitation of the cavity as shown in figure 5.8. From that data we estimate that in the vicinity of the 26^{th} harmonic (1.24054093 MHz) the detector had a mechanical resonance located at 1.240700 MHz with

mechanical Q factor $Q_m \approx 4000$. Then for an observed maximum displacement Δl, the average acceleration is given by equation 3.6,

$$\langle a \rangle = \Delta l \left[(\omega_0^2 - \omega_p^2)^2 + \left\{ \frac{\omega_p \omega_0}{Q_m} \right\}^2 \right]^{\frac{1}{2}} \qquad (6.13)$$

It is important to note that this equation is derived assuming that the tidal accelerations produce longitudinal vibrations in the detector as discussed previously. For all of the data sets, the detector was at a distance of 23.3±.5 cm from the proton beam. The data was obtained at an energy of 800 GeV so that $\gamma=853$ ($\beta \approx 1$). The limits placed on G_A as obtained from the data of table 5.3 through equations 6.13, 6.11 and 6.3' are shown in table 6.1 for the seven data sets. For sets 6 and 7 we give the corresponding limit from two adjacent frequency bins.

The best limit is that obtained from data sets 6 and 7. Taking an average of these measurements we can state that

$$G_A < 2 \times 10^{19} \; G_N$$

at the 90% confidence limit. This result is indicated as a dimensionless coupling $G_A m_p^2/\hbar c$ on a logarithmic scale in figure 6.1.

6.3 Limits on Metric Strain

In this case we consider the direct effect of a perturbation in the locally flat metric of space-time on the electromagnetic field.

Table 6.1

Limits on G_A/G_N from Measured Accelerations at 800 GeV

Data Set	Bandwidth (mHz)	Intensity	Expected Accel. cm/s²	Observed Limit cm/s²	Limit on G_A/G_N
1	62.5	6.62×10^{12}	3.45×10^{-24}	4.3×10^{-4}	1.2×10^{20}
2	50.0	5.94×10^{12}	3.09×10^{-24}	4.3×10^{-4}	1.4×10^{20}
3	25.0	3.20×10^{12}	1.67×10^{-24}	1.6×10^{-4}	9.6×10^{19}
4	.800	5.39×10^{12}	2.81×10^{-24}	1.9×10^{-4}	6.8×10^{19}
5	.128	4.00×10^{12}	**********	********	********
6 (bin 63)	40.0	8.41×10^{12}	4.38×10^{-24}	3.6×10^{-5}	8.2×10^{18}
(bin 64)	40.0	8.41×10^{12}	4.38×10^{-24}	2.6×10^{-5}	5.9×10^{18}
7 (bin 63)	40.0	7.87×10^{12}	4.10×10^{-24}	8.4×10^{-5}	2.0×10^{19}
(bin 64)	40.0	7.87×10^{12}	4.10×10^{-24}	6.9×10^{-5}	1.7×10^{19}

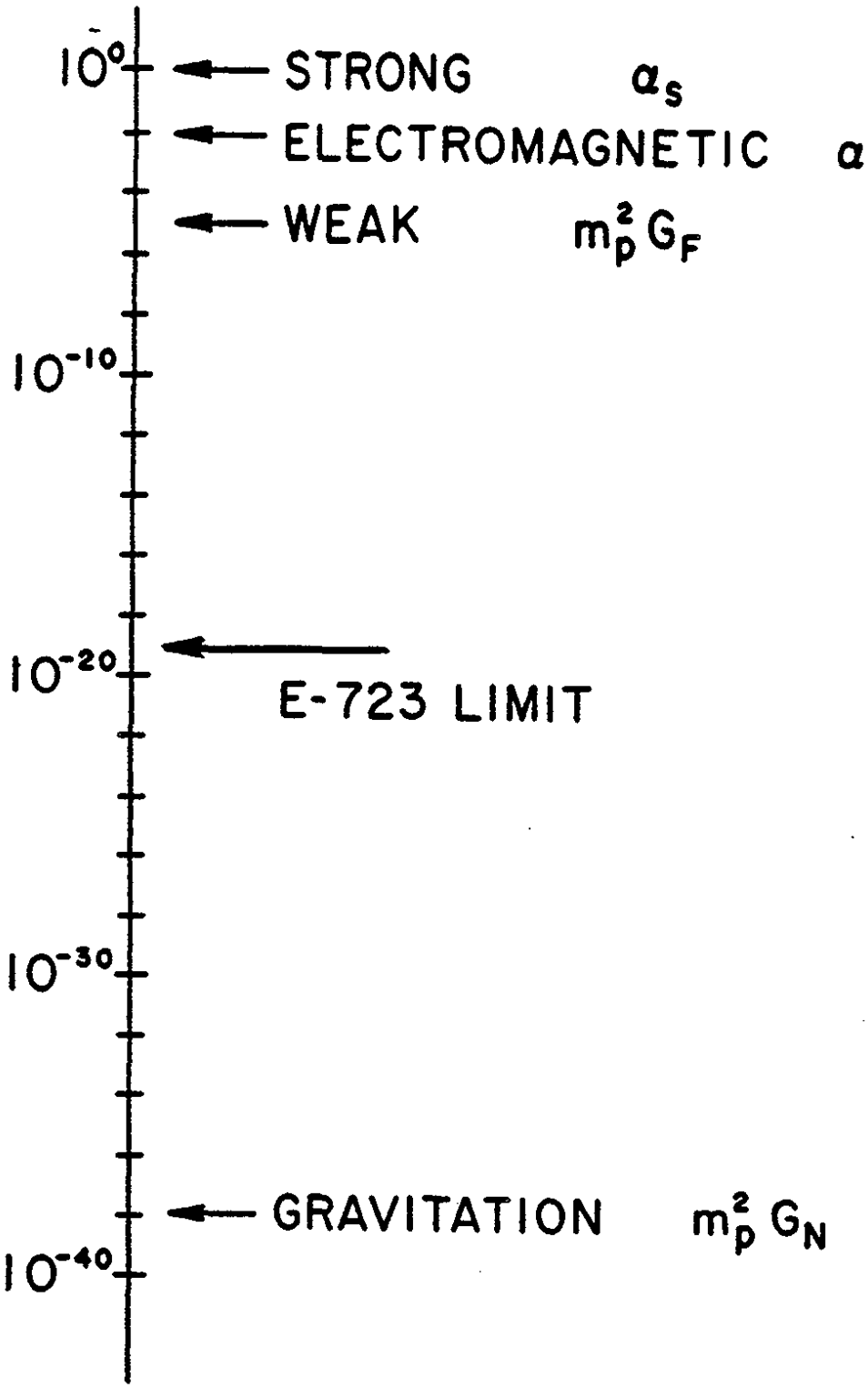

FIGURE 6.1 LIMIT ON STRENGTH OF ANOMALOUS INTERACTIONS

The limit obtained from this effect is generally weaker than that established in section 6.2. This is due to the fact that these perturbations are what give rise to coherent mechanical accelerations impatred to the cavities. The mechanical structure of the cavities then allows the longitudinal displacement to build up in accordance with equation 6.13 and this enhancement is absent in this analysis. We place a limit on the metric strain from the measured limits on the cavity endwall displacement with the use of

$$\langle h_{lim} \rangle \sim \frac{\Delta l_{limit}}{l} \tag{6.14}$$

where l represents the physical length of the cavity l=8 cm. From equation 6.5' we can then place a limit on G_A/G_N. This calculation has the advantage of unambiguous interpretation since it does not depend on the complex mechanical response of the detector.

The expected metric strain can be calculated using equation 2.6 which we note was derived from equation 1.3 by assuming the particle bunch to be Gaussian shaped and averaging over the beam revolution period.

Thus,

$$\langle h_{00} \rangle = \frac{4G\gamma m_{eff}}{\pi Rc^2} \cdot \log\left(\frac{2\pi R\gamma}{b}\right) \tag{6.15}$$

where R is the radius of the beam orbit and b is the distance from the beam to the detector. Again, we must use equation 6.12 to

determine the effective mass of the beam which contributes to the 26^{th} harmonic. The results are summarized in table 6.2.

An interesting interpretation of these data is that the metric in the vicinity of the proton beam remains locally flat to one part in 10^{16}!

We see that these limits are weaker than those of table 6.1. The ratio of $G_A m_p^2/\hbar c$ to α_e (α_e is the fine structure constant) is typically of the order 10^{-11} for the direct measurement and 10^{-17} for the results in table 6.1. This is a measure of the shielding of the cavity fields from the electric fields of the circulating protons. A qualitative analysis of this effect is given in Appendix D.

6.4 Sensitivity Limits

From figure 6.1 we see that the observed strength of the interactions are 19 orders of magnitude above the expected gravitational signal strength and 17 orders of magnitude below the electromagnetic interaction strength. For the first six data sets, the sensitivity of the detector is limited by the background microwave noise level. The last two data sets contain a signal of unknown origin that represents a new limitation on the detection sensitivity. Of course, other factors such as higher electrical Q_e, higher mechanical Q_m and better beam harmonic content would all contribute to an improved limit.

Table 6.2

Limits on G_A/G_N from Measurements on Metric Strain at 800 GeV

Data Set	Bandwidth (mHz)	Expected Strain	Observed Limit	Limit on G_A/G_N
1	62.5	8.2×10^{-42}	2.5×10^{-15}	3.0×10^{26}
2	50.0	7.3×10^{-42}	2.5×10^{-15}	3.4×10^{26}
3	25.0	3.9×10^{-42}	9.3×10^{-16}	1.3×10^{26}
4	.800	6.6×10^{-42}	1.1×10^{-15}	1.7×10^{26}
5	.128	*********	*********	********
6 (bin 63)	40.0	1.0×10^{-41}	2.1×10^{-16}	2.1×10^{25}
6 (bin 64)	40.0	1.0×10^{-41}	1.5×10^{-16}	1.5×10^{25}
7 (bin 63)	40.0	9.7×10^{-42}	4.9×10^{-16}	5.1×10^{25}
7 (bin 64)	40.0	9.7×10^{-42}	4.0×10^{-16}	4.1×10^{25}

The microwave noise arises from the phase noise of the stabilized oscillator at the pump frequency populating the upconversion mode and thus propagating through the detection system with the proper frequency. This noise is random in phase and hence the noise power level depends on the detection bandwidth. The exact level of this noise fluctuated due to the wideband standing wave structure of the long coupling lines and the changes which occurred in the phase balancing of the hybrid tee from one data set to another. However this background level was carefully measured for each detection scheme and is enumerated below in Table 6.3.

If we form a logarithmic average we can determine the effective detector temperature T_N from

$$\langle P \rangle = 4kT_N B \tag{6.16}$$

where k is Boltzman's constant and B is the detector bandwidth.

$$\frac{\langle P \rangle}{B} = 147 \text{ dBm/Hz} = 2.22\times10^{-18} \text{ Watts/Hz}$$

$$\therefore \; T_N = 40{,}000°K$$

This can be compared to the overall noise temperature of the detection electronics which for each case was ~650° K (corresponding to a noise figure of 4.9 dB). Thus we see that the effective noise temperature is dominated by the phase noise of the oscillator. A

Table 6.3
Background Microwave Noise Spectral Density

Data Set	Bandwidth (mHz)	P_2 (dbm)	Spectral Density (dBm/Hz)
1	62.5	-159.77	-148
2	50.0	-159.50	-147
3	25.0	-168.20	-152
4	.800	-178.57	-148
5	.128	-195.12	-156
6	40.0	-159.10	-145
7	40.0	-156.10	-142

NOTE: All spectral density measurements are ±3 dB.

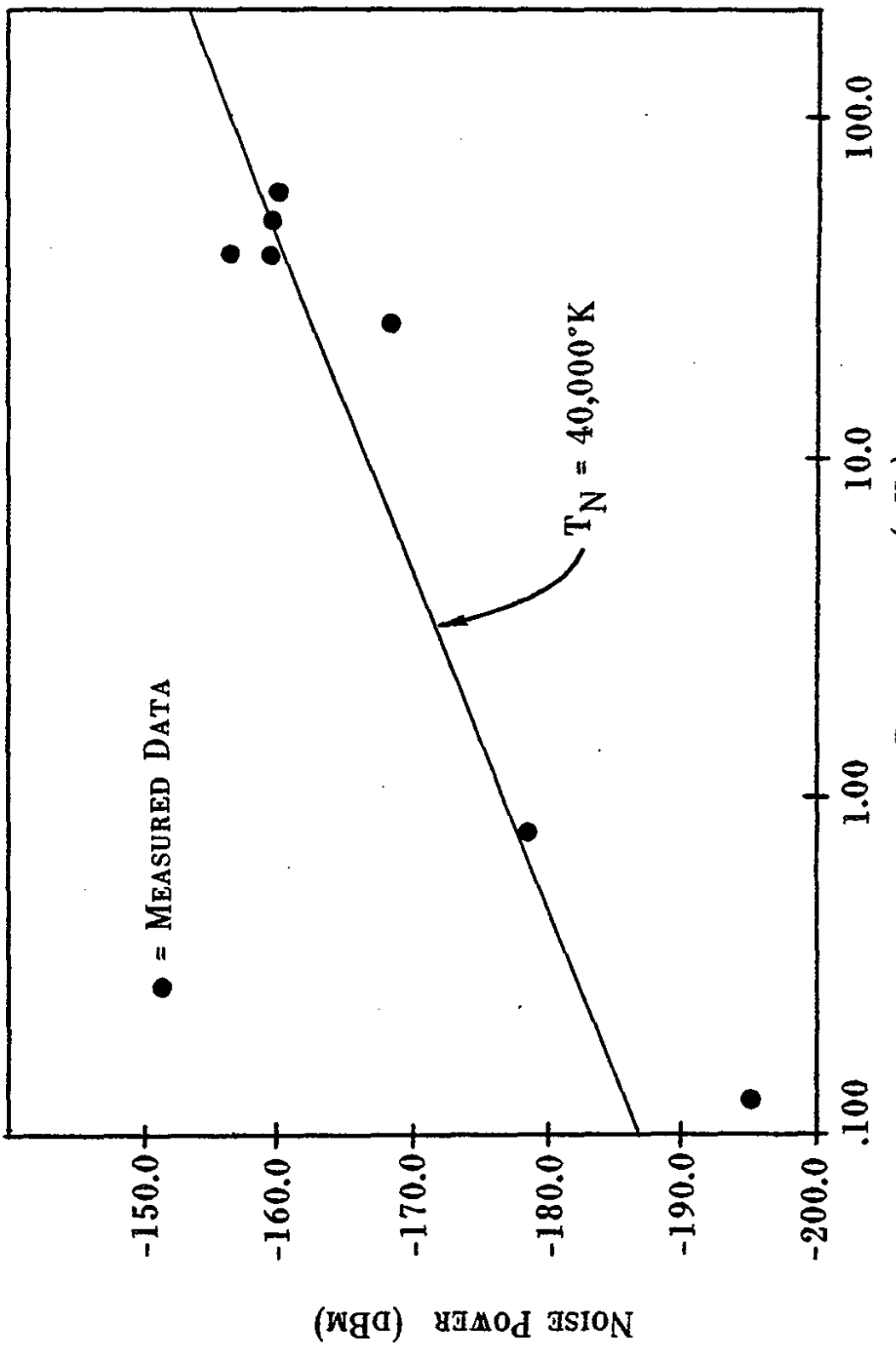

Figure 6.2 Noise Power versus Bandwidth

plot of equation 6.16 is shown in figure 6.2 for a noise temperature of 40,000° K along with the measured values for the data sets. We see that the noise generally decreases with decreasing bandwidth. The departures from the theoretical values are a result of the standing wave structures of the transmission lines and the subsequent difficulty in phase balancing the hybrid tee.

Another limitation on the sensitivity of the detector is the Brownian noise associated with thermal mechanical vibrations of the detector. This noise manifests itself as endwall displacements induced by the thermal bath energy at the detector.

The Brownian noise associated with a measurement of Δl is given by equation 3.31.

$$\Delta l(\omega) = \frac{2Q}{m\omega_0^2}\sqrt{\frac{kTm\omega_0}{Q}} = \sqrt{\frac{Q}{\omega_0}}\sqrt{\frac{4kT}{m\omega_0^2}} \qquad (6.17)$$

For a 1 Hz bandwidth measurement with Q_m=4140, f_0=1.240700 MHz, temperature T=4.2° and assuming that the mass which resonates is that of the resonant endwall, m≈60 g , we get,

$$\Delta l_{Brownian} = 2.89\times10^{-16}\ cm/\sqrt{Hz} \qquad (6.18)$$

For the best measurement at 4.2° the bandwidth was 40 mHz so that,

$$\Delta l_{Brownian} = 5.78\times10^{-17}\ cm \qquad (6.19a)$$

and for 1.89 K,

$$\Delta l_{Brownian} = 3.88\times10^{-17} \text{ cm} \qquad (6.19b)$$

These effects are a factor of 10^2 smaller than the observed displacements given in table 5.3. This shows that lowering the phase noise power will improve the sensitivity of the detector but eventually it will be limited by the Brownian motion of the endwall for a given bandwidth. The detection sensitivity can be improved by increasing the integration time of the detector or equivalently decreasing the bandwidth of the measurement scheme. A different approach to improving the sensitivity of the detector to acceleration measurements is to decrease the mechanical frequency of interest and/or increase the mechanical Q of the detector. This is evident from equation 6.13.

Operation of the detector in the high radiation environment presented other possible sources of noise to the detector. The first to be considered is the electromagnetic coupling of the beam to the cavity fields. This effect arises from two possible sources. One is the propagation of a time dependent electric (or magnetic) field from the beam into the detector. One could consider the direct excitation of the second mode by the electromagnetic fields of the beam. However, f_2=9.945 GHz and the closest harmonic of the beam RF is 187X53.1x10^6=9.930 GHz. This is a highly suppressed harmonic and differs from mode 2 of the cavities by 15 MHz. A more

likely possibility is the induced Coulomb force exerted on the endwall due to the time dependent electromagnetic fields of the beam. Such a case is treated qualitatively in Appendix D. This effect will arise due to the 26^{th} harmonic of the electromagnetic field of the beam but will be attenuated by the stainless steel beam pipe as well as the metal in the dewar.

From the analysis given in Appendix D we find that the maximum electric field at the cavities is

$$E = 2.7\times10^{-2} \text{ V/m}$$

and the corresponding force which causes the cavity to vibrate at the 26^{th} harmonic is

$$F \sim 8\times10^{-16} \text{ N}$$

resulting in a displacement of the endwall of the order

$$\Delta l \sim 10^{-22} \text{ cm}$$

Thus we see that this effect is too small to be detected by the present cavity.

Yet another possibility is the effective displacement produced by the excitation of the PZT due to the induced electric fields across its electrodes. We show in the appendix that such an effect would produce maximum displacements of the order 10^{-15} to 10^{-17} cm and would be dependent on the strength of the 26^{th} harmonic.

Further tests on the origin of the signal in the last data set are needed to establish its source. The most important test is to measure the energy dependence of this signal during the energy ramp of the beam cycle. For an electromagnetic signal there should be no energy dependence whereas for the anomalous effects described in

chapter 1 one expects dependence of the form γ^n where $n \geq 2$.

In conclusion we state that the origin of the signal in the final data set is unknown but most likely due to the electromagnetic pick-up by the PZT or one of the strain gauges. Further improvements in the sensitivity of the detector in the accelerator environment are needed to explore the origin of this signal. In addition, it appears that no new longe range forces appear for highly relativistic massive particles at the level

$$\frac{G_A}{G_N} \sim 10^{19} \tag{6.20}$$

References

1. H.J. Paik, Phys. Rev. D, 19D, 2320, (1978).

2. G. Feinberg, J. Sucher, Phys. Rev. D, 20D, 1717 (1979).

3. J.E. Moody and F. Wilczek, Phys. Rev. D, 30D, 130, (1984).

4. C.S. Anlakh and R.N. Mohapatra, Phys. Letts., 119B, (1982) 136.

Appendix A

A Test of Special Relativity

One of the fundamental postulates of the theory of special relativity is that the velocity v of a particle of rest mass m is always less than the velocity of light (c). The velocity is related to the momentum p and the energy E of the particle through

$$\gamma = \frac{E}{mc^2} = \frac{\sqrt{p^2c^2+m^2c^4}}{m^2c^2} \qquad (A.1)$$

and

$$\gamma = \frac{1}{\sqrt{1-\beta^2}} \qquad (A.2)$$

where

$$\vec{\beta} = \frac{\vec{v}}{c}$$

These relationships were first tested using relativistic electrons from nuclear beta decay where typically $\gamma \sim 2\text{-}3$. High energy particle accelerators shere $\gamma \sim 1000$ or higher can be used for more precise tests of equation A.2. The fact that accelerators operate as

designed is itself a confirmation of the theory.

The energy ramp of the proton beam from 150 GeV to 800 GeV per proton allows a unique test of special relativity. During this portion of the beam cycle, a series of RF cavities with electric fields oriented along the particle trajectory are used to accelerate the protons during each revolution around the ring. At the same time, the field strength of the dipole magnets which guide the beam along its nearly circular orbit must simultaneously be increased so that the radius of the beam orbit remains fixed. We can thus treat the dipole fields as a single uniform homogeneous magnetic field which generally increases as a function of time. We also will assume that the particle orbit is circular. The motion of the individual protons is then governed by the Lorentz force law given below.

$$\vec{F} = q\vec{v} \times \vec{B} \tag{A.3}$$

q is the charge on the proton and v is the velocity of the trajectory through the magnetic field $\vec{B}$. The condition for a stable circular orbit is met when this force is balanced by the centripetal force on the proton.

$$qvB = \frac{mv^2}{R} \quad \text{or} \quad p = qBR \tag{A.4}$$

where R is the radius of the circular orbit. The result of equation

A.4 remains valid for relativistic momenta p.

In order to make a precise test of equation A.2 we compare the change in the revolution frequency f of the particles with the change in magnetic field. We can establish the relation between the frequency and the magnetic field as follows;

$$f = \frac{\beta c}{2\pi R} = \frac{v}{2\pi R} \tag{A.5}$$

Solving A.2 for v and substituting into equation A.5 we get

$$f = \frac{c}{2\pi R}\left(1-\frac{1}{\gamma^2}\right)^{\frac{1}{2}} \tag{A.6}$$

Now from equation A.1 we note that

$$E = \sqrt{p^2c^2+m^2c^4} = \gamma mc^2$$

For the Tevatron, E is always greater than 150 GeV and m is the rest mass of the proton so that $E >> mc^2$ and $\gamma >> 1$. We then make the approximation that

$$E \approx pc \quad \text{or} \quad pc \approx \gamma mc^2 \tag{A.7}$$

Since $\gamma >> 1$ we can expand equation A.6 as follows:

$$f = \frac{c}{2\pi R}\left(1 - \frac{1}{2\gamma^2} + \cdots\right) \tag{A.8}$$

so that the change in frequency during the ramp cycle can be written

$$f_2 - f_1 = \frac{c}{4\pi R}\left(\frac{1}{\gamma_1^2} - \frac{1}{\gamma_2^2}\right) \tag{A.9}$$

Now since $E \approx pc = \gamma mc^2$, substitution into equation A.4 yields the relationship between γ and the magnetic field namely,

$$\gamma = \frac{RqB}{mc} \tag{A.10}$$

For the Tevatron, B is linearly related to I, the current in the dipole magnets. In the limit $\gamma >> 1$,

$$\gamma \propto \frac{RqI}{mc} \tag{A.11}$$

Finally, substituting the result in equation A.9 we get the desired relationship,

$$f_2 - f_1 = \alpha\left(\frac{1}{I_1^2} - \frac{1}{I_2^2}\right) \tag{A.12}$$

where α is a constant which can be determined experimentally.

The actual magnet current during one particular ramp cycle was measured and is plotted in figure A.1 as a function of time. This figure also shows the derivative of the magnet current and thus shows that the energy of the proton beam is slightly non-linear with time. We can independently measure the time dependence of the revolution frequency of the beam with the beam position monitors described in section 4.7. Thus we can compare the expected frequency shift of the beam given by equation A.12 with the measured data and test our hypothesis.

A measurement of the revolution frequency at the 1113^{th} harmonic (53.1 MHz) was made and is shown in figure A.2. From the magnet current data obtained simultaneously, the frequency shift was calculated where the extreme points at 150 GeV and 800 GeV were used to determine the constant α in equation A.12. The calculated points are compared with the data (solid curve) in figure A.3.

From figure A.3 we see that the largest deviation between the calculated and observed values is of the order

$$\delta f \leq 10 \text{ Hz} \qquad \text{(A.13)}$$

We can use this information to set a limit on the deviation of equation A.2 from the exact form of special relativity. We assume that

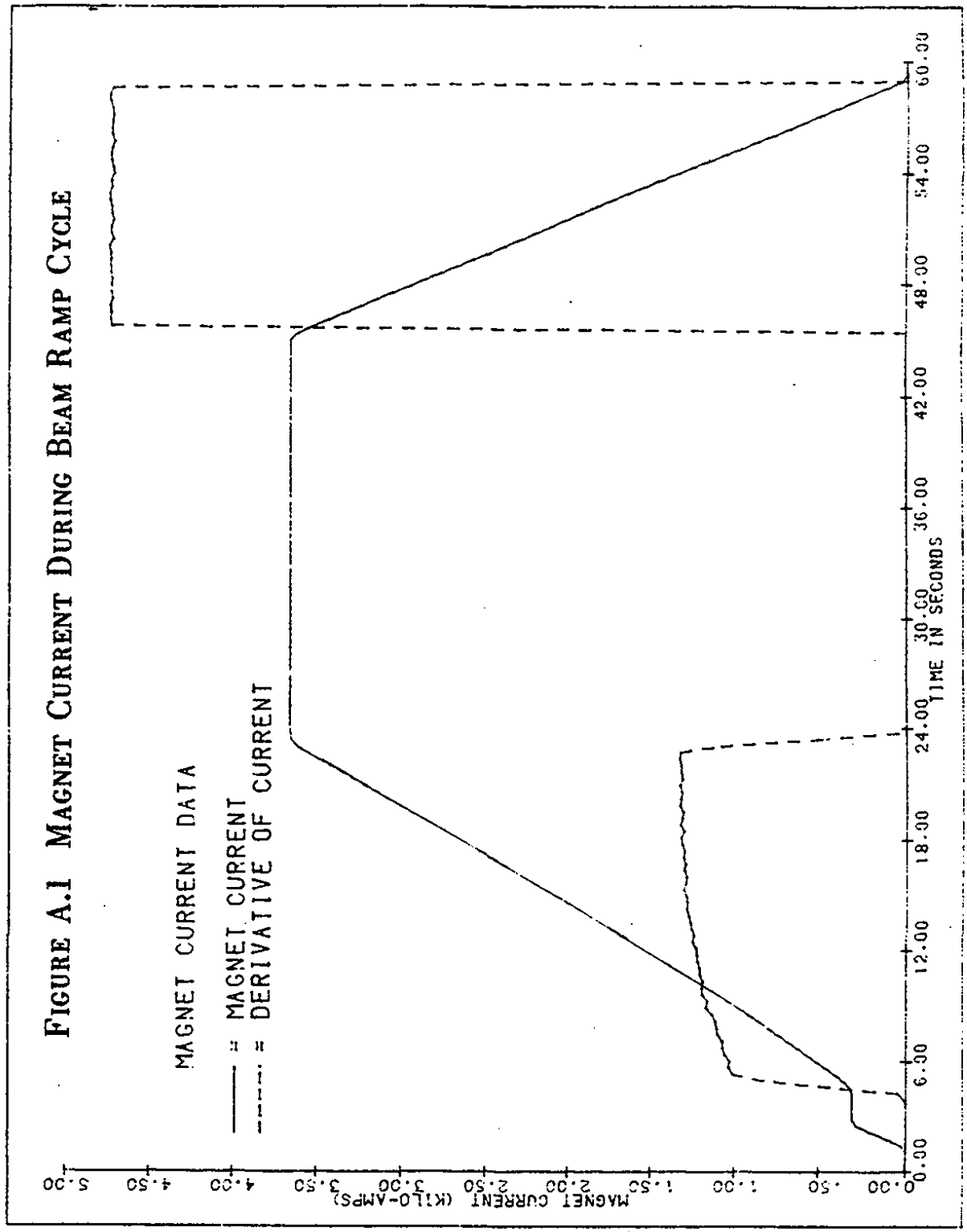

FIGURE A.1 MAGNET CURRENT DURING BEAM RAMP CYCLE

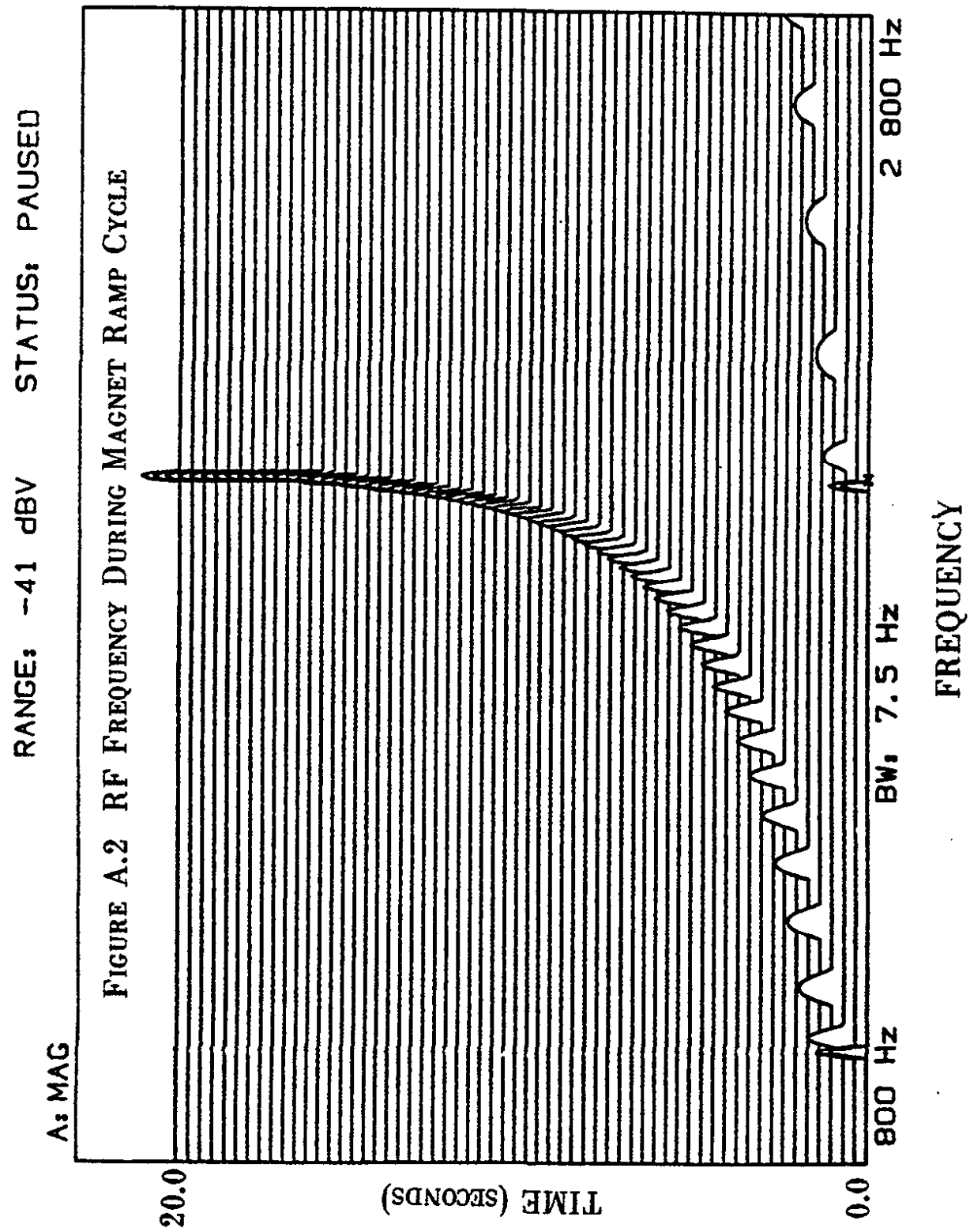

FIGURE A.2 RF FREQUENCY DURING MAGNET RAMP CYCLE

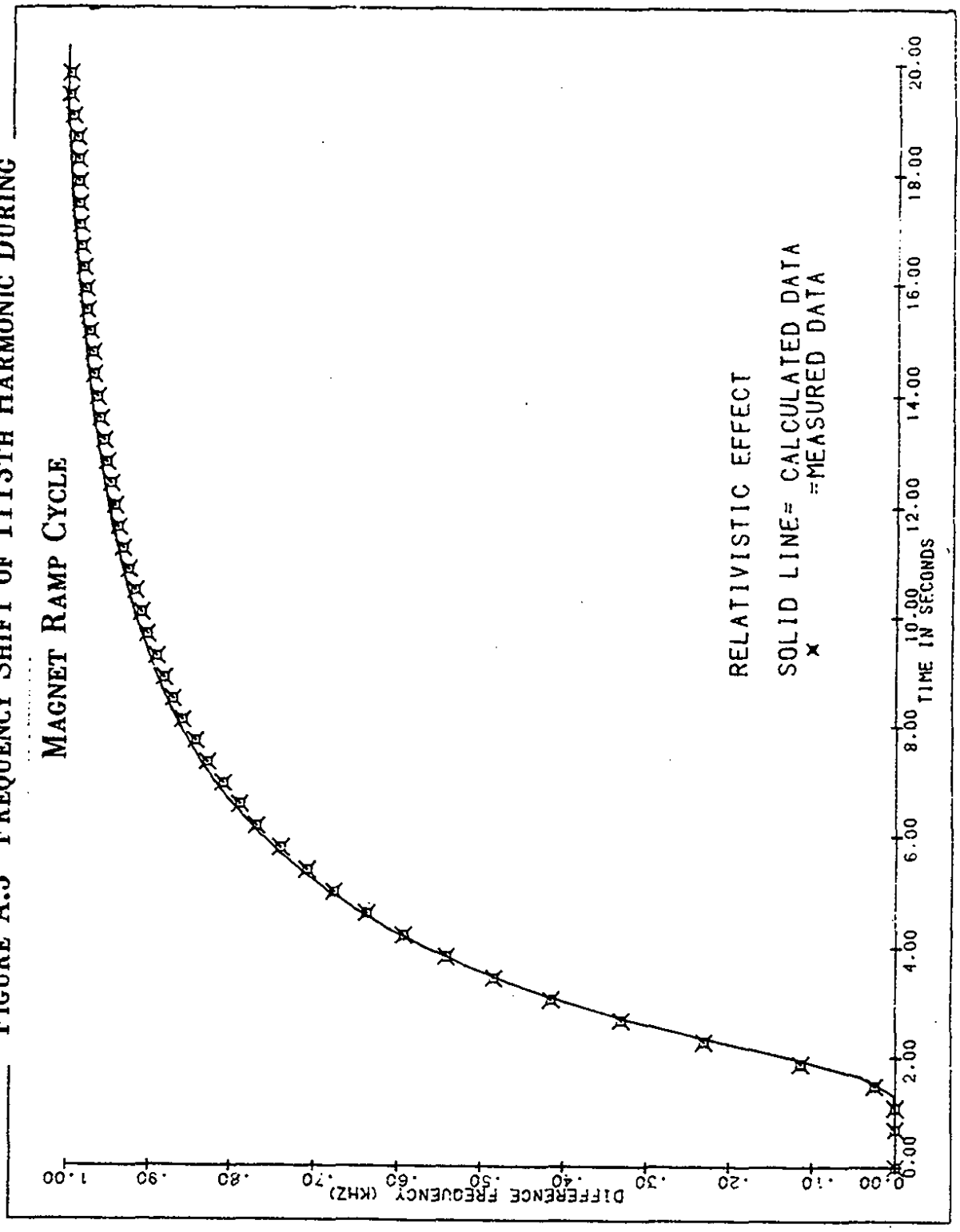

FIGURE A.3 FREQUENCY SHIFT OF 1113TH HARMONIC DURING MAGNET RAMP CYCLE

$$\beta^2 \approx \left[1 - \frac{1}{\gamma^{(2+\varepsilon)}}\right] \tag{A.14}$$

Then we can write

$$f = f\infty \left(1 - \frac{1}{\gamma^{(2+\varepsilon)}}\right)^{\frac{1}{2}}$$

and

$$f = f\infty \left[1 - \frac{1}{2\gamma^{(2+\varepsilon)}} - \mathcal{O}\left\{\frac{1}{\gamma^4}\right\}\right] \tag{A.15}$$

where

$$f\infty = n \cdot \frac{c}{2\pi R}$$

with n the harmonic number. Since $\varepsilon << 1$ we can write

$$f = f\infty \left[1 - \frac{1}{2\gamma^2} - \cdots\right] + f\infty \cdot \frac{1}{2\gamma^2} \cdot \varepsilon \ln(\gamma) \tag{A.16}$$

The first term on the right hand side of equation A.16 is the same as given by equation A.12 and used to calculate the points in figure A.3. The second term represents the anomalous correction due to the

form introduced in equation A.14. Thus

$$\delta f = f_\infty \cdot \frac{1}{2\gamma^2} \cdot \varepsilon \ln(\gamma) \leq 10 \text{ Hz}$$

We finally note that

$$f_\infty \cdot \frac{1}{2\gamma^2} = f_\infty - f$$

so that

$$\delta f = (f_\infty - f) \cdot \varepsilon \ln(\gamma) \leq 10 \text{ Hz}$$

Taking $(f_\infty - f)$=100 Hz which corresponds to E ≈ 400 GeV we obtain

$$\varepsilon \leq \frac{10}{100} \cdot \frac{1}{\ln(400)} = 0.017 \qquad \text{(A.17)}$$

which shows the accuracy of the functional relationship of equation A.2.

It should be remarked that a change in the equilibrium orbit by 0.1 mm corresponds to a fractional frequency shift of

$$\frac{\delta f}{f} = \frac{\delta R}{R} = \frac{10^{-4}}{10^3} = 10^{-7}$$

Since $f \approx 53$ MHz this would give $\delta f = 5.3$ Hz. Thus the observed deviation of the frequency from the calculated values may well be due to radial shifts of the equilibrium orbit. Displacements of 0.1 mm are not uncommon and are the limiting factor on the accuracy of the result presented in equation A.12.

Appendix B

Fourier Analysis of the Beam Structure

The Tevatron has 1113 RF buckets equally spaced around the ring. Each bucket travels around the ring with frequency

$$f = \frac{v}{2\pi R} = \frac{\beta c}{2\pi R}$$

We write the density per unit time of the m^{th} bucket as

$$f_m(t) = A_m f_0(t) \qquad (B.1)$$

where A_m is the number of protons in the bucket and does not change in time. Furthermore, all buckets are assumed to have the same distribution $f_0(t)$. Then the total beam density is

$$F_{total}(t) = \sum_{m=0}^{1112} A_m f_0(t-t_m) \qquad (B.2)$$

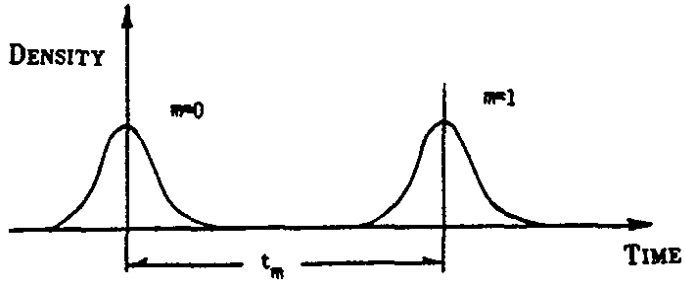

$$t_m = \left(\frac{2\pi mR}{1113\beta c} \right) \tag{B.2a}$$

where t_m is the time delay between the first and the m^{th} bucket.

The Fourier amplitudes for a single bucket are given by

$$f_{0n} = \frac{1}{2T} \int_{-T}^{+T} f_0(t) e^{-in\pi t/2T} dt \tag{B.3}$$

Here $2T=2\pi R/\beta c$ is the beam revolution period and we used the fact that $f_0(t)$ is periodic in the interval -T to +T. The amplitude f_{0n} corresponds to the frequency $\omega_n=n\omega_0$ where $\omega_0=\beta c/R$. In terms of the Fourier components the contribution of a single bucket to the beam density is

$$f_m(t) = A_m \sum_{n=-\infty}^{\infty} e^{in\pi(t-t_m)/T} f_0 \tag{B.4}$$

and summing over all buckets

$$F_{tot}(t) = \sum_{m=0}^{1112} A_m \sum_{n=-\infty}^{\infty} e^{in\pi(t-t_m)/T} f_0$$

$$= \sum_{n=-\infty}^{\infty} C_n e^{in\pi t/T} \tag{B.5}$$

where the coefficients C_n are defined as

$$C_n = \sum_{m=0}^{1112} e^{-in\pi t_m/T} A_m f_0 \tag{B.6}$$

Now suppose the buckets are Gaussian shaped in the longitudinal direction so that for a fixed observer

$$f_0(t) = \frac{1}{\sqrt{2\pi}\sigma} e^{\frac{1}{2}(t/\sigma)^2} \tag{B.7}$$

Here, σ represents the rms width of the pulse. Then, the Fourier amplitudes of $f_0(t)$ are

$$f_0 = \frac{1}{2T} \int_{-T}^{+T} \frac{e^{-(\frac{1}{2}\sigma^2 t^2 + in\pi t/T)}}{\sqrt{2\pi}\sigma} dt \tag{B.8}$$

Since the rms length of the pulse is typically 2 nsec and is much shorter than the revolution period, we can extend the limits of integration to infinity to evaluate the integral in closed form. We then obtain

$$f_0 = \frac{\omega_0}{2\pi} \cdot e^{-\frac{1}{2}(n\omega_0\sigma)^2} \tag{B.9}$$

and since

$$t_m = \frac{2mT}{1113}$$

$$C_n = \sum_{m=0}^{1112} e^{-2inm\pi/1113} A_m f_o \qquad (B.6')$$

For any given pattern of the A_m we can obtain the complex coefficients C_n from equation B.6'. In terms of real functions, we write

$$F^n(\omega) = G_n \cos(n\omega_o t + \phi) \qquad (B.10)$$

where ϕ = Arc Tan (B/A)

and

$$G_n = 2\sqrt{A_n^2 + B_n^2}$$

where

$$A_n = \sum_{m=1}^{1113} A_m f_{o\,n}(\omega) \cos\left(\frac{2\pi\omega m}{1113}\right)$$

$$B_n = \sum_{m=1}^{1113} A_m f_{o\,n}(\omega) \sin\left(\frac{2\pi\omega m}{1113}\right) \qquad (B.11)$$

A particularly suitable normalization for this prescription is provided by dividing F^n by the size of the n^{th} harmonic assuming all of the protons are in a single bucket so that m=0.

$$F_{norm}(\omega) = \frac{F_{total}(\omega)}{F_0(\omega)} \qquad (B.12)$$

where $F_0^n(\omega)=2A_0 f_{0\,n}(\omega)$ and is obtained by setting m=0 in equations B.10 and B.11. In this way, all of the beam induced effects can be derived for the case of a single gaussian bucket and then normalized for the N^{th} harmonic by multiplying by this ratio. Equivalently, we can measure the 1113^{th} harmonic and the N^{th} harmonic and experimentally determine equation B.12 as follows

$$\left(F_{norm}(\omega)\right)^2 = \frac{\alpha_N}{\alpha_{1113}} \qquad (B.13)$$

where α_n and α_{1113} are the measured power at the N^{th} and 1113^{th} harmonic respectively. We have assumed that the beam distribution is roughly uniform so that the 1113^{th} harmonic is equivalent to having all of the protons in a single bucket.

A computer program was written based on equations B.10, B.11 and B.12 and was used to determine the Fourier structure of the beam reported in chapter 2 for different beam distributions. As described in chapter 2 the program adequately predicts the expected size of the 26^{th} harmonic as well as the 1113^{th} harmonic and their

ratio. From the analysis as well as from direct measurements this ratio was found to be

$$\frac{\alpha_N}{\alpha_{1113}} = \frac{1}{18.6} \tag{B.14}$$

Appendix C

Simulation of the Signal Processing

The complexity of the off-line analysis, and of the detection and data acquisition system warranted a test of the procedures used. This appendix describes a test using simulated data logged with the data acquisition system described in section 4.8. The techniques described in chapter 3 were used analyze the data to test the software of the off-line analysis and establish the advantage of the phase shifted voltage average over the rms power average.

The PDP-11/34 computer logged data from the HP3582A FFT in a 16-bit format such that the first four 16 bit words represented the real and imaginary voltage respectively of the first frequency bin of channel A of the FFT. The following 4 bytes represented the real and imaginary voltage of channel B and so forth. The words were repacked into the real and imaginary parts by the software of the program.

The signal output of the HP3582A FFT was proportional to the voltage measured. The normalization below gives the relationship between the linear magnitude A logged on data tape and the power in units of dBV

$$(\text{Power})_{\text{dBV}} = 20 \cdot \log_{10}(A) - 86.43 + G \qquad (C.1)$$

Here G is the full scale of the gain setting selected for the

measurement. For instance, if the full scale setting for channel A was -30 dBV and the output of the FFT was A=100,

$$(P)_{dBV} = 20 \cdot \log_{10}(100) - 86.43 - 30 = -76.43 \text{ dBV}.$$

For a system with an impedance of 50Ω the relatioship between power units of dBV and dBm is

$$P_{dBm} = P_{dBV} + 13.01 \qquad (C.2)$$

Note that 1.0 mW is defined as 0.0 dBm.

The data was then analyzed using the two averaging techniques we describe here. The rms power average was formed by averaging the sum of the squares of the real and imaginary parts of each channel bin by bin.

$$\langle P_{rms} \rangle = \langle V^2_{real} + V^2_{imag} \rangle \qquad (C.3)$$

The phase shifted voltage average was formed by calculating the phase of channel B for each bin using the formula given below and then shifting the phase of the signals in the corresponding bins of channel A by that amount.

$$\phi_B = \text{Arc Tan} \left(\frac{B_{imag}}{B_{real}} \right)$$

and

$$\phi_A = \text{Arc Tan}\left(\frac{A_{imag}}{A_{real}}\right)$$

so that

$$A = A_r e^{i(\phi_A - \phi_B)} \qquad (C.4)$$

The resulting real and imaginary voltages of channel A were averaged over all of the beam cycles logged. Finally the power of the phase shifted average was calculated as the sum of the squares of its real and imaginary parts.

$$\langle P_{shifted} \rangle = \langle V_{imag} \rangle^2 + \langle V_{real} \rangle^2 \qquad (C.5)$$

The coherence function of the data was calculated using the formalism given in chapter 3.

The test data was obtained by using a HP3325A Synthesizer to generate a signal at a frequency of 12.6 kHz and at a power level of -40.0 dBV. This signal was added to the output of the random noise generator of the HP3582A FFT at an average level of -35.6 dBV and applied to channel A of the FFT as shown in figure C.1. The synchronous output of the HP3325A provided the (reference) input to channel B of the FFT at 5.4 dBV. The computer was used to write 186 spectra to data tape for off-line analysis.

Figure C.2 shows the rms power average of the test data. In this case, no phase adjustment was made with respect to channel B and at the frequency of interest (12.6 kHz) no clear signal appears. The signal level at 12.6 kHz was -34.9 dBV or -21.9 dBm. The bottom curve shows the same data averaged using the phase shifted voltage averaging technique. In this case it is clear that a signal is present and that the phase shifting technique has improved the signal to noise ratio of the detection system. The signal power in the center frequency bin (at 12.6 kHz) was -38.77 dBV. We thus see the value of calculating the phase shifted voltage average since it allows the detection of a signal in the noise even though as in this case the expected signal is smaller than the average rms noise level. The corresponding coherence was plotted as a function of frequency and is shown in figure C.3. It is obvious from this plot that a signal is present in channel A which is correlated in phase with the reference in channel B. We will now show that the coherence function can be used to obtain the same results as the phase shifted analysis using equations 3.25 and 3.26.

$$S = \xi^2 A$$

$$N = (1-\xi^2)A$$

$$\frac{S}{N} = \frac{\xi^2}{(1-\xi^2)}$$

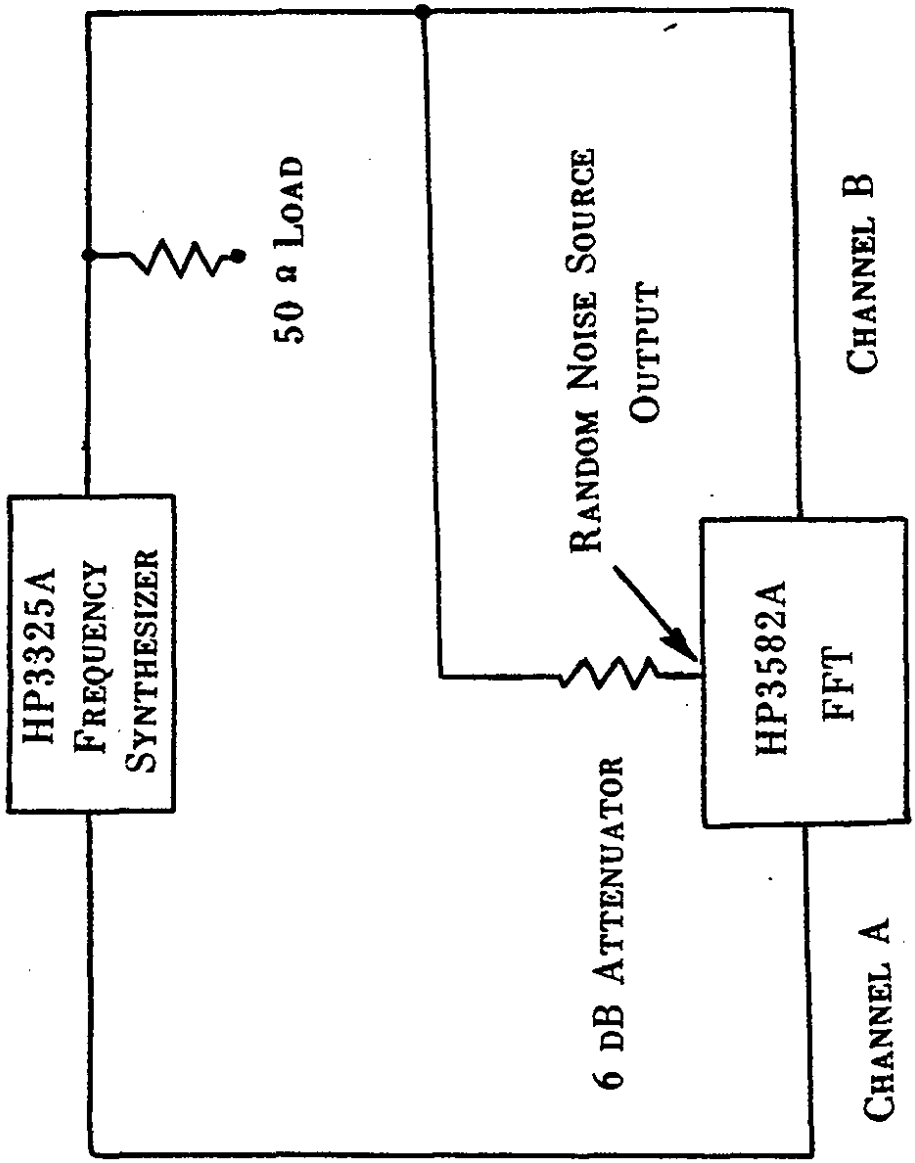

Figure C.1 Apparatus for Simulating Test Data

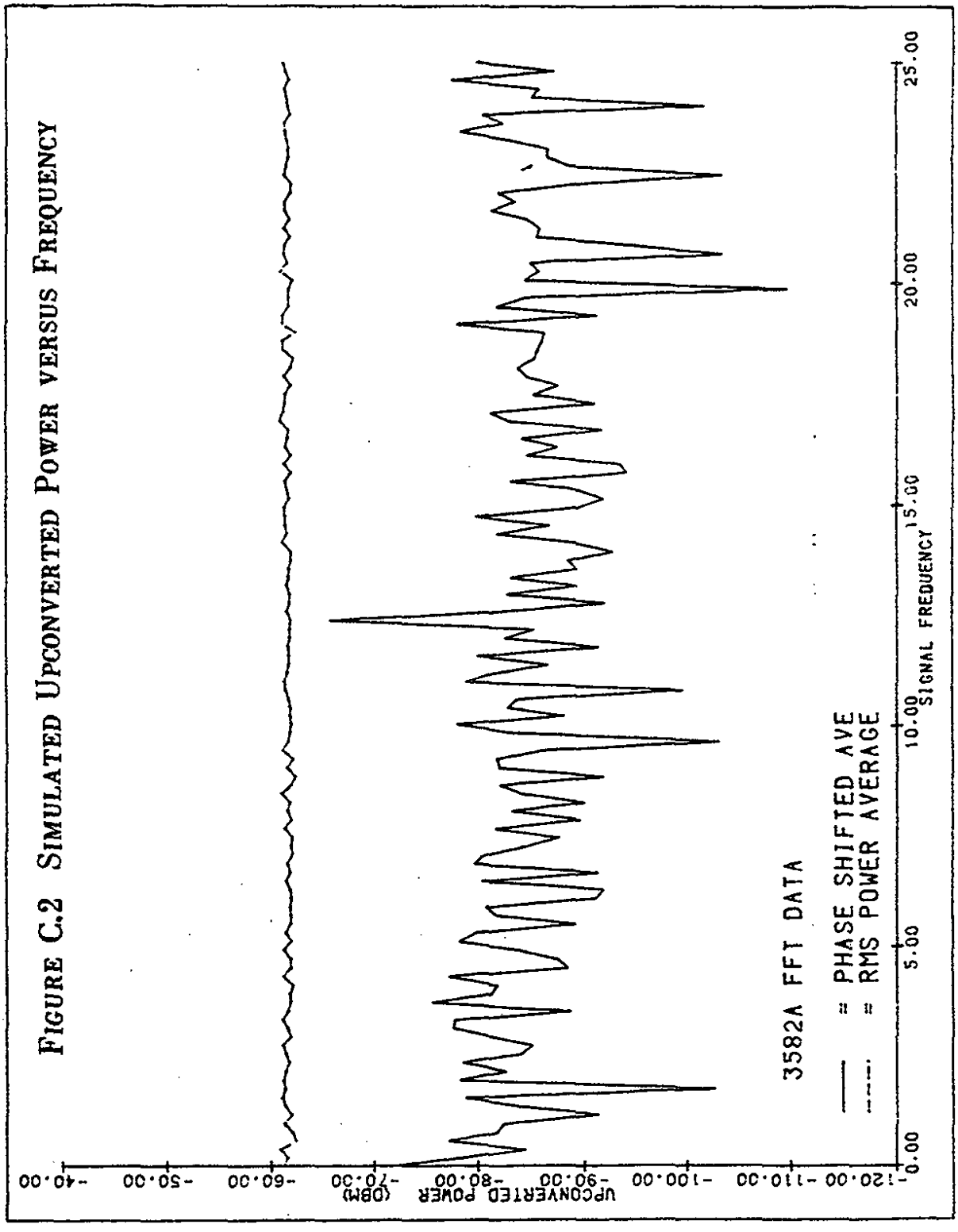

FIGURE C.2 SIMULATED UPCONVERTED POWER VERSUS FREQUENCY

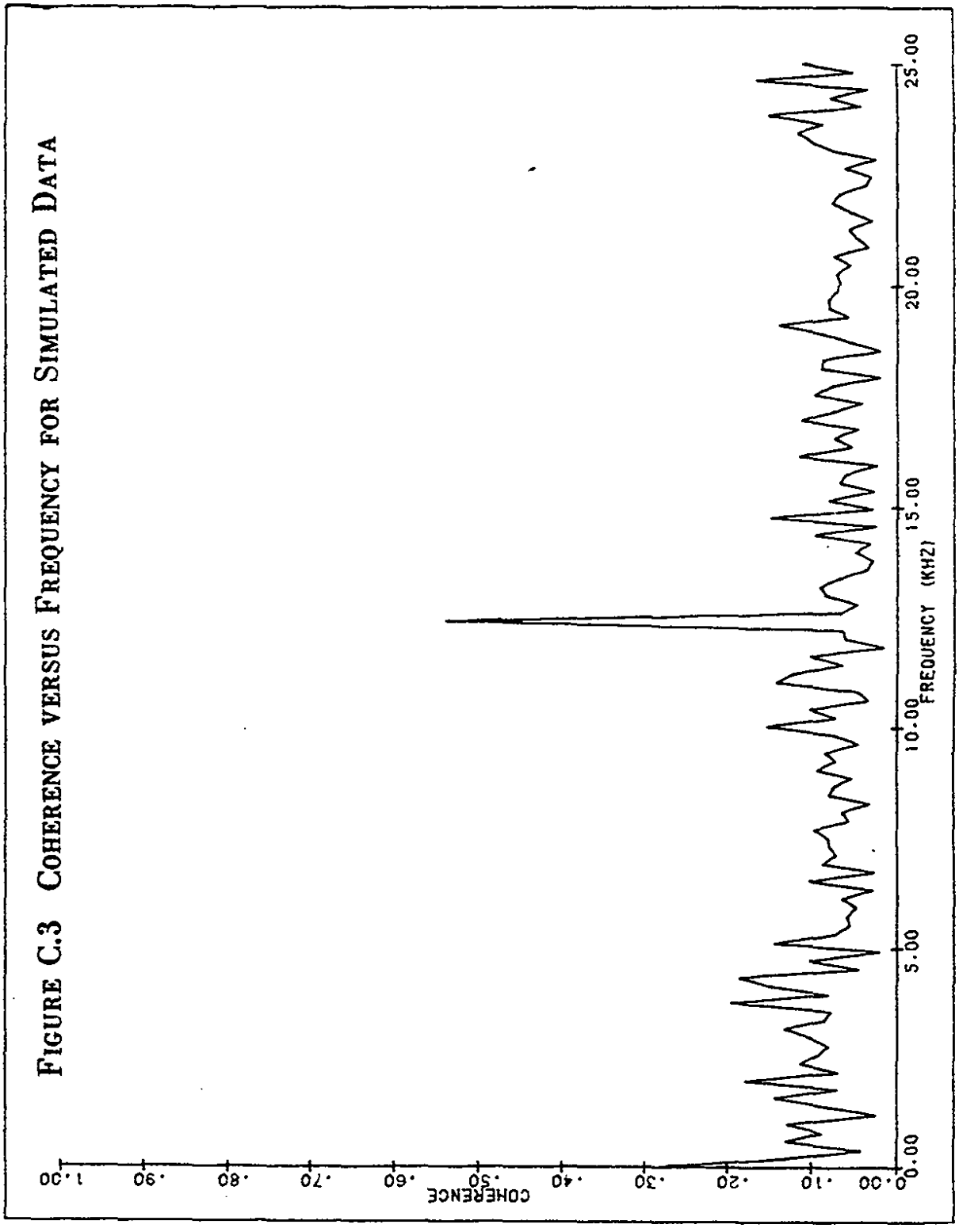

FIGURE C.3 COHERENCE VERSUS FREQUENCY FOR SIMULATED DATA

The input values for the table below show the measured noise and signal powers and the values calculated with the coherence function. We see that the phase shifted averages are in close agreement with the calculated values from the coherence function.

Using the same apparatus shown in figure C.1, the FFT was allowed to take 256 averages and calculate the coherence function and the rms power averages of both channels. The resulting sinal levels for channel A and channel B were -33.8 dBV and 5.4 dBV respectively. The measured coherence function was .54 at 12.6 kHz. These values are in excellent agreement with the calculated values.

Table C.1

Comparison of Input and Measured Signal and Noise Powers

	Input Signal (dBV)		Measured (dBV)	
	Signal	Noise	Signal	Noise
Channel A	-40.0	-35.6	-39.2	-35.3
Channel B	+5.4	*****	+5.4	*****

Appendix D

Electromagnetic Background

The electromagnetic background places limitations on the ultimate sensitivity of the detector. We present an analysis of several different possible sources of noise and the size of the limits they impose. Consider an observer at a distance b from a highly relativistic particle of charge q traveling in the x direction as shown.

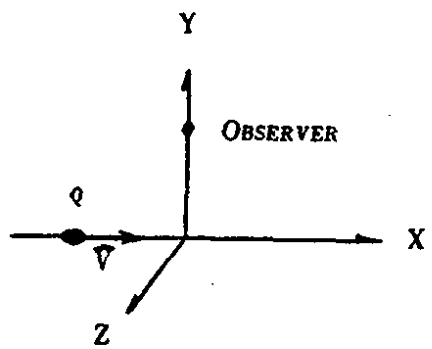

The electric field in the y direction is

$$E_y(t) = \frac{b}{4\pi\epsilon_0}\left(\frac{\gamma^2 q^2}{(b^2+\gamma^2 v^2 t^2)^3}\right)^{\frac{1}{2}} \qquad (D.1)$$

We can calculate the average electric field at the position of the observer by integrating over the revolution period of the beam since the pulse is shorter in time than the effects we wish to observe at 1.24 MHz and 53.1 MHz. Thus

$$\langle E \rangle = \frac{1}{T}\int E_y(t)dt \approx \frac{q}{4\pi\epsilon_0 bvT} \qquad (D.2)$$

where T is the period for the frequency of interest T=1/f. From the studies on the harmonic content of the beam presented in chapter 2 we know that the largest signals appear at the RF frequency of 53.1 MHz and the 26^{th} harmonic of the beam revolution frequency at 1.240 MHz. The size of the electric fields for 53.1 MHz can be found by assuming the 10^{13} protons are evenly distributed in the 1113 buckets. Then

$$\langle E_{1113} \rangle = \frac{fq_e}{4\pi\varepsilon_0 bc} \cdot \left(\frac{N}{1113} \right) \qquad (D.3)$$

where N is the total number of protons. For the Tevatron, N ~ 10^{13}, f=53.1 MHz and b=20 cm so that $\langle E \rangle$ = 11 V/m at a distance of 20 cm from the beam. We note that $\langle E \rangle$ = 63 V/m at a distance of 3.5 cm from the beam. This is in good agreement with measured voltages across the beam pick-ups which were typically 2.5±.3 Volts for 10^{13} protons. The corresponding electric field at the electrodes of the pick-ups was 71±8 V/m.*

The proton beam is surrounded by a stainless steel pipe ~3 mm thick and the cavities are housed inside a dewar jacket made of stainless steel. We estimate that the total thickness of the stainless steel which shields the electric fields is about 5 mm. The transmission coefficient of a conductive sheet with thickness D>>δ where δ is the skin depth is

*This is estimated as V/2d with d the spacing between the electrodes at 7 cm.

$$T = 2\sqrt{2}\frac{D}{\delta}e^{-D/\delta} \tag{D.4}$$

where

$$\delta = 2c\sqrt{\frac{\varepsilon_0}{\omega\sigma}}$$

and σ is the conductivity of the sheet. In this case $\sigma = 1.4\times10^{6}$ $(\Omega m)^{-1}$. The thickness of the stainless steel is $D \approx 5\times10^{-3}$ m. For the 26^{th} harmonic, the skin depth is

$$\delta_{26} = .54 \text{ mm} \tag{D.5}$$

with a corresponding transmission coefficient of

$$T_{26} = 2.5\times10^{-3} \tag{D.6}$$

Thus the electric field at the cavity is

$$E_{26} = T_{26}E = 2.7\times10^{-2} \text{ V/m} \tag{D.7}$$

For the 1113^{th} harmonic, the skin depth is

$$\delta_{1113} = 8\times10^{-5} \text{ m} \tag{D.8}$$

and

$$T \sim 9\times10^{-25} \tag{D.9}$$

so that

$$E_{1113} \approx 10^{-23} \text{ V/m} \tag{D.10}$$

Thus we would not expect an appreciable effect fron the 1113^{th} harmonic due to the large attenuation by the stainless steel.

The presence of the small electric field at the frequency f can contribute to two different backgrounds. First, the electric field will induce a surface charge on the endwall given by

$$\Sigma = \frac{4\pi\epsilon_0 E \ell}{l} \tag{D.11}$$

where l is the length of the cavity. Then the cavity will be subject to a force F_e which is periodic with frequency 2f. If 2f=1.24 MHz this force will produce an upconverted signal. The force is given by

$$F_e \approx \Sigma A E \approx 4\pi\epsilon_0 E^2 A \tag{D.12}$$

where A is the area of the endwall.

For cavity dimensions of the order 10^{-1} m and E = 2.7×10^{-2} V/m,

$$F_E \sim 8\times10^{-16} \text{ N} \tag{D.13}$$

Then for a mechanical Q_m=4140 the harmonic displacement of the endwall of the cavity at the 26^{th} harmonic is approximately

$$\Delta l = \frac{F_E Q}{m\omega^2} = \frac{4\pi\epsilon_0 E^2 A^2 Q}{m\omega^2} \qquad (D.14)$$

We chose m to be the mass of the endwall ~60 g so that

$$\Delta l \approx 10^{-22} \text{ cm} \qquad (D.15)$$

Such a displacement is too small to be detected by our present apparatus.

A second possibility is the strain produced by motion of the PZT due to the induced electric fields across its electrodes. The electric field at the cavities is shown to be attenuated by a factor of ~2.5×10^{-3}. The expected attenuation in the power is thus ~50 dB. The 26^{th} harmonic during the data runs was approximately -50 dBm so that we might expect that the power applied to the PZT was of the order -100 dBm. Then from the plot of upconverted power versus PZT excitation shown in figure 5.5 we can estimate the size of this effect. Remembering that the gain of the detection system for figure 5.5 was 62 dB we find the following relation between upconverted power P and the power P_A applied to the PZT.

$$P = P_A - 102 \text{ dB} \qquad (D.16)$$

where P and P_A are in units of dBm.

Thus

$$P \simeq -202 \text{ dBm} \qquad (D.17)$$

If on the other hand we calculate the effect for strain gauge 1 we find that P≃-180 dBm and we are in close agreement with the results of the experiment.

Another possible source of noise is the particle background in the vicinity of the detector. As the buckets of protons are accelerated, some may come in contact with the walls of the beampipe. This leads to a large shower of charged particles at relativistic energies. To observe the size of such effects, three particle scintillators or "paddles" were positioned near the detector as shown in figure D.2. Each paddle was approximately 60 cm long and 40 cm wide for a total area of 2400 cm^2. They were arranged so that the outer two scintillators were 30 inches apart and were placed perpendicular to the beam axis.

The output of the photomultiplier tubes connected to each of the paddles was applied to a LeCroy Model 621DL Quad Discriminator followed by a LeCroy Model 465 Coincidence Unit. The coincidence unit was used to detect particles which traveled through all three sets of paddles within a 20 nanosecond timespan. The total number of coincident particles was counted by a Jorway Model 1880 Dual Channel BCD Scalar.

During HEP running periods, we found that the particle spray consists of general background spray which occurs continuously throughout the beam cycle and several bursts of radiation. These bursts occur during the injection from the booster into the main ring, the injection from the main ring into the Tevatron and at the start of "flat-top" for the Tevatron. The background particle spray occurs at a level of about 5×10^5 particles per second and the bursts were generally larger than 10^6 particles per burst. The bursts were short in duration (.1 sec) and probably saturated the detection electronics so that an accurate count was not obtainable. We assume for the course of this discussion that the particle spray was of the order 10^7 particles/sec. We can estimate the total number of particles crossing the detector from the ratio of the area of the scintillator to that of the cavities. The cavity cross section was about 25 cm^2 so that

$$\frac{\text{Area of Cavities}}{\text{Area of Paddles}} \times 10^7 \text{ particles/sec} \sim 10^5 \text{ particles/sec}$$

Each particle will deposit (on average) an energy of 2 MeV per gram of Niobium it crosses. The total energy imparted to one gram of Niobium is of the order of 10^{-8} Watts. This will not significantly change the temperature of the cavities and hence will not appreciably degrade the electrical Q.

The particle bursts can contribute to the background electromagnetic noise level at harmonics of the beam revolution

frequency since they occur for each pass of the buckets around the ring near our detector. A test for this source of noise was made by mixing the outputs of the photomultiplier tubes in the Anzac MD-140 Mixer and measuring the output with the HP3561A Spectrum Analyzer. Figure D.3 shows the result during the injection into the main ring and during the main ring ramp cycle. Figure D.4 shows a similar result for the injection into the Tevatron. The peaks occur at a frequency which is less than the 1.240541 MHz frequency we are interested in and furthermore, we do not take data during these portions of the ramp cycle. Figure D.5 shows one final measurement made at the start of the Tevatron spill. The signal level for this measurement is ~-24 dBm at 1.2405409 MHz (±.5 Hz). Data is taken which encompasses this burst but it tends to be very short in duration and we expect its phase relationship to any expected signal to be random depending on focusing of the beam and the individual particle trajectories. Thus we do not expect this effect to significantly effect the background noise spectrum.

To differentiate between background and a real signal the energy dependence of the upconverted power must be studied. Electromagnetic effects should be independent of energy. It is also important to measure the dependence of the observed signal on beam intensity. This is in principle difficult since the intensity is already near its maximum value and the size of the 26^{th} harmonic also depends on the beam distribution. One further test would be to introduce additional shielding to attenuate the electric and

magnetic fields impinging on the strain gauges. Such shielding would not in principle affect the size of gravitational strains or any other extremely weak interaction.

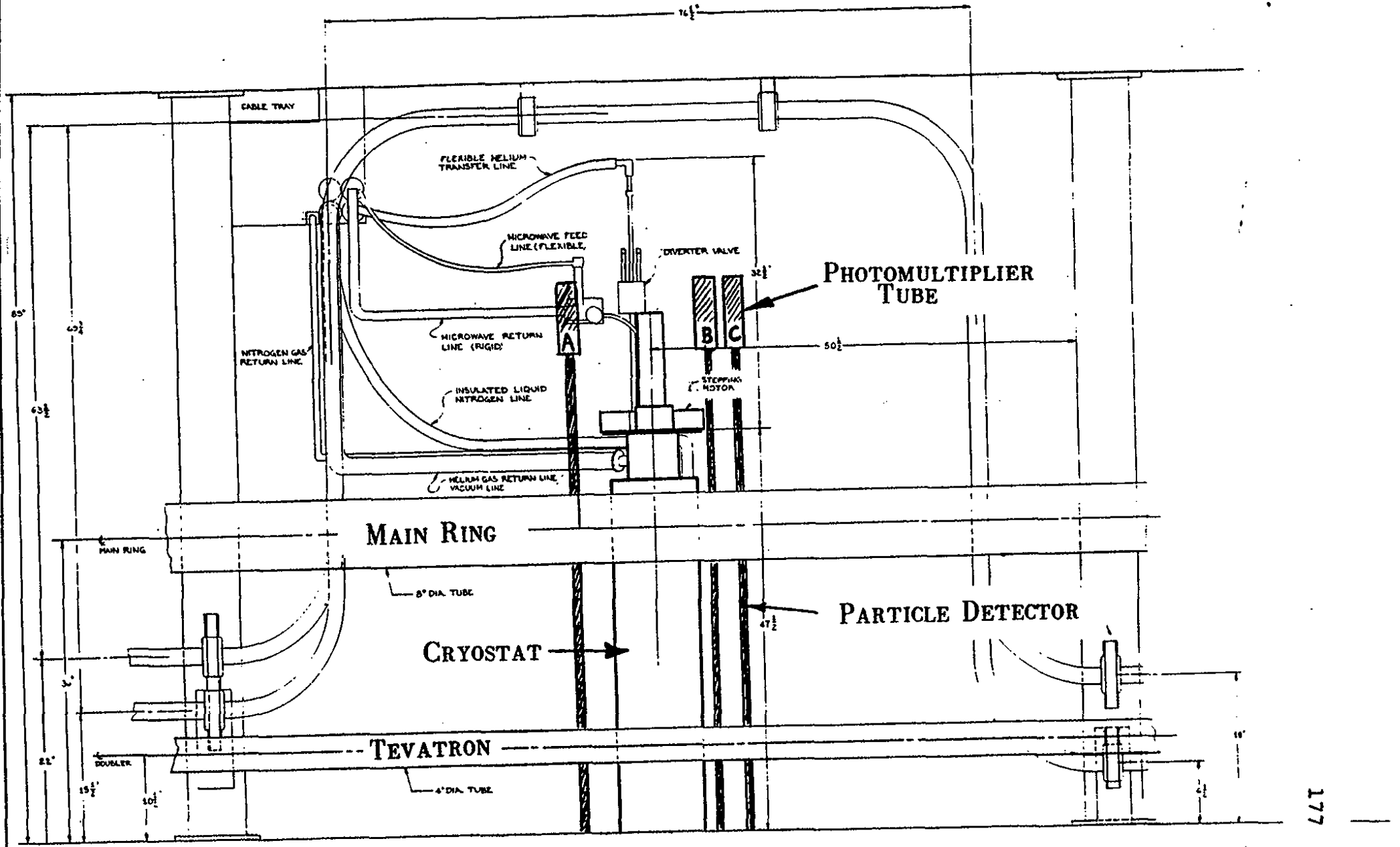

FIGURE D.2 LOCATION OF PARTICLE COUNTERS AT C0

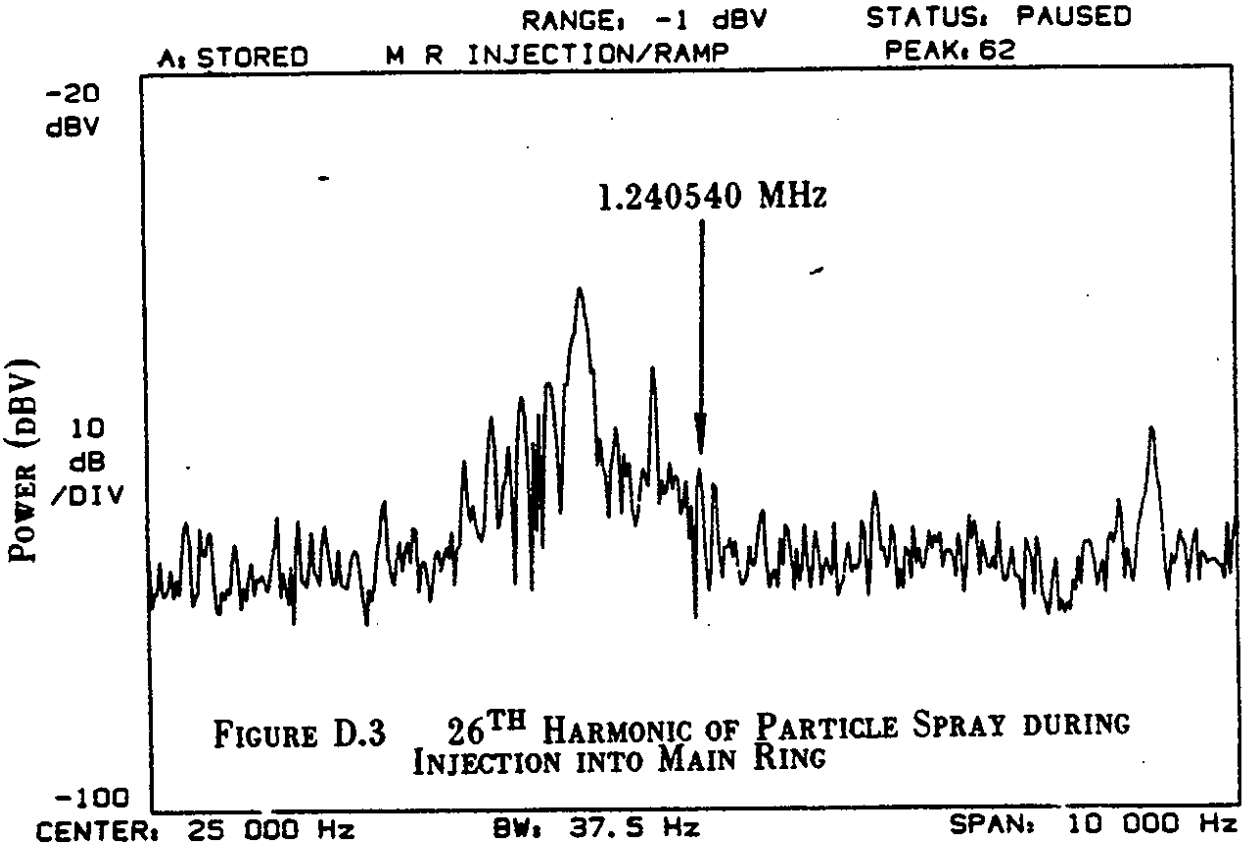

FIGURE D.3 26^{TH} HARMONIC OF PARTICLE SPRAY DURING INJECTION INTO MAIN RING

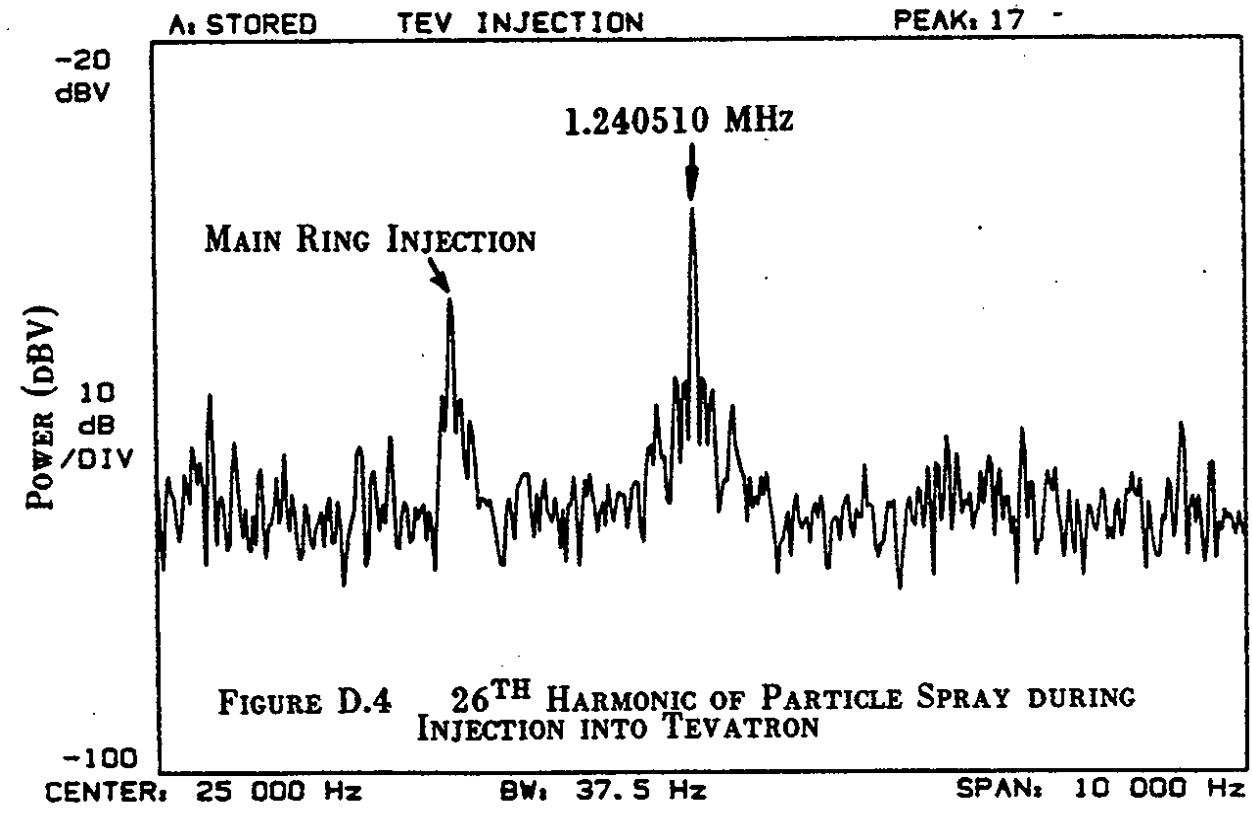

FIGURE D.4 26^{TH} HARMONIC OF PARTICLE SPRAY DURING INJECTION INTO TEVATRON

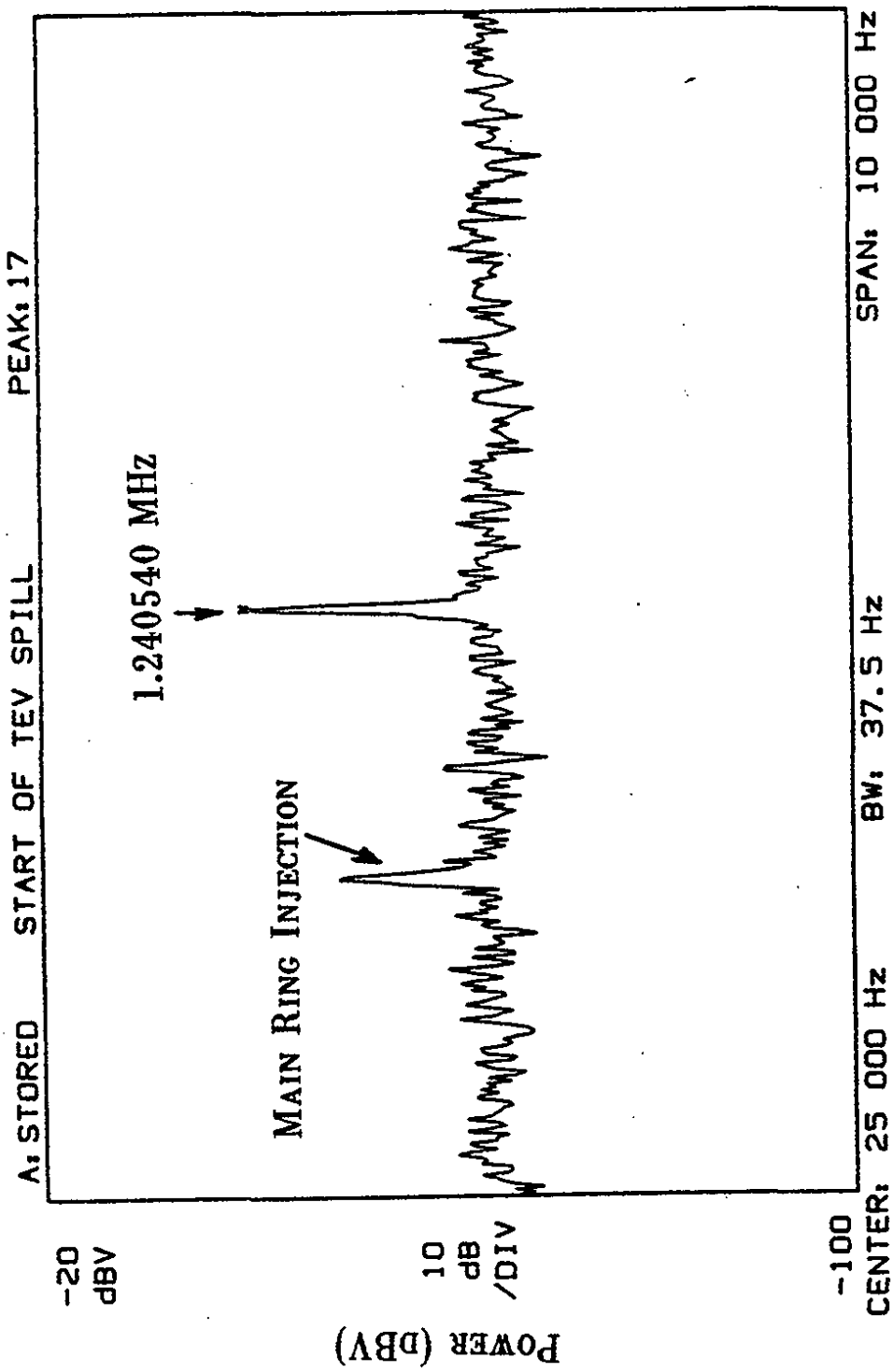

FIGURE D.5 26^{TH} HARMONIC OF PARTICLE SPRAY DURING SPILL